Micro spectrometer for the measurement of the composition of new gas

Sebastiaan Voorderhake
1222015

Daily supervisor:
Dr. G. de Graaf
Supervisor:
Dr. R.F. Wolffenbuttel

September 11, 2011

Micro spectrometer for the measurement of the composition of new gas

---

Thesis

submitted in partial fulfillment of the requirements for the degree of

Master of Science

in

Electrical Engineering

in the department of Microelectronics, EEMCS

by

Sebastiaan Fabian Voorderhake

Committee members:

Prof. K.A.A. Makinwa	(TU Delft: Electronic Instrumentation Laboratory)
Dr. R.F. Wolffenbuttel	(TU Delft: Electronic Instrumentation Laboratory)
Dr. W. Haije	(TU Delft: DelftChemTech - ECN: Biomass, Coal & Environmental Research)
Dr. G. de Graaf	(TU Delft: Electronic Instrumentation Laboratory)
Dr. A. Emadi	(TU Delft: Electronic Instrumentation Laboratory)
ing. F. Bakker	(ECN: Engineering & Services)

Electronic Instrumentation Laboratory

Faculty of Electrical Engineering, Mathematics and Computer Science

Delft University of Technology

Abstract

As the world is in need of more sustainable energy sources, the use of new gases like hydrogen or bio-gases seems to be a very attractive one. By mixing these new gases with the traditional natural gas, it becomes possible to have a smooth and economically durable transition. The amount of new gases added may be dependent on the availability, progress of technology and safety and regulatory issues. This is very much like what is already been done with electrical energy sources like wind or solar power. However, unlike electricity, gas comes in a wide variety.

Unfortunately appliances and machines currently running on gas are designed to operate only within a very strict window of gas compositions. To be able to widen this band, it is required to have machines that can adapt, depending on the available gas composition. It is therefore required to be able to measure this composition.

This thesis describes the first steps in the design and development of an infrared absorption multi-gas micro-spectrometer for the measurement of the concentrations of Carbon Monooxide (CO), Carbon Dioxide (CO_2) and Hydro Carbons (C_xH_{2x+2}) in a composite gas. This includes mathematical modeling, design and fabrication.

From the model it is found that it should be possible to design a system which is capable of detecting all these gases with sufficient accuracy and over their total dynamic range. Test structures have been designed and partly fabricated, giving great insight in the limitations, restrictions and tolerances of the fabrication process.

Acknowledgments

This work would not have been possible without the help of many people to whom I am indebted. It is my pleasure to heartily thank all those who helped me during this year. In particular, I would like to express my deepest gratitude to:

Dr. Reinoud Wolffenbuttel, my supervisor, for his support and guidance during this project. He was always open for discussion on any topic and always managed to motivate me when times were a bit difficult.

Dr. Ger de Graaf, my daily supervisor, to whom I am very thankful for all the time and effort he put in discussing the details of the project.

Arvin Emadi, Huaiwen Wu and Fabio Santagata, Phd students. They were of absolute importance to get to this thesis by sharing their knowledge and research. These researches are in many aspects the ground work for this thesis. I am therefore most grateful that they were always available for questions and advice about both theory and practical work.

Willem van der Vlist and Hugo Schellevis, DIMES technicians. Although we encountered many difficulties during the processing, you have always tried to create a work around.

Other DIMES staff, especially Lina Sarro, for discussions on fabrication techniques and materials.

To all people from the DUT Racing Formula Student team for giving me an amazing time here in Delft and giving me the opportunity to make mistakes, develop myself and become the person who I am today. Together we experienced great sorrows but also the greatest heights, both of which I will never forget.

To all my house mates: Mascha, Kah Kih, Rick, Benny, Femke, Frank, Jeroen, Wijnand, Anton, Anne and Stèphan. You always made me feel truly at home and over the years became much more than just house mates. Our friendships will never be lost.

All my other friends, especially Bart Brandhoff, for all those beers which made sure that just enough brain cells died to keep me sane.

Finally, but of course absolutely not the least important, my parents (Jan and Ingrid), sister (Sabine) and brother in law (Ronald), for their continuous support in all aspects. I have always been free to follow my own path and could count on your love no matter what.

Contents

Chapter 1

Introduction

1.1 Motivation

Governments and energy suppliers are facing a huge challenge. The primary energy supplies are slowly being consumed and a big debate is going on regarding the environmental effects associated with the energy production and its use. The key players in this market (e.g. governments, suppliers and consumers) are therefore currently involved in a discussion regarding the transition of the society to a more sustainable energy system. The biggest difficulty in this debate stems from the fact that the energy sector exhibits great inertia which is associated with the enormous infrastructure in the form of, for example, power grid lines, oil and gas pipelines or refuelling stations. Refitting the complete infrastructure seems practically impossible because of cost and time issues. Therefore the primary focus is to use the existing networks and adapt them wherever required. Moreover the consumer market must also be gradually transformed, since at present it is tuned to specific properties of the existing fuels.

Natural gas as a source of energy

If we look at the share of natural gas in the world's total primary energy supply (TPES), we can see that it is the third largest after oil and coal. In the year 2000 it was already as big as 21.1% and it is expected to reach 25.8% in 2030. [1]. Taking into account the fact that the TPES is estimated to increase from 9963 to 16300 million tons of oil equivalents (Mtoe) over the same period of time, the volume of the gas market will be doubled. Since natural gas is considered the cleanest form of all fossil fuels, it might be the right source of energy for mitigation of environmental problems and therefore may serve as a bridge between the present and the future, in which molecular hydrogen and bio-gases will play a role, along with natural gas. Unfortunately also natural gas is a limited source and is currently being estimated to run out somewhere around 2068. [2]

The introduction of new gases

However, this limit to natural gas, does not mean that gas as an energy source is not to be pursuit any further. For further sustainability of the gas network, an increased amount of research is being conducted into so called new gases (e.g. Hydrogen or bio-gases), which may be produced by for example farmers or greenhouses. Another alternative is the electrolysis of water into hydrogen and oxygen with electricity from sustainable sources such as wind, water or solar energy.

One issue with these new gases is that it is not yet clear what the effects might be on the infrastructure. But assuming that the transmission network or its distribution counterpart will be able to cope with the change, a very attractive scenario for the introduction of the new gases into the energy infrastructure seems to be to mix them into natural gas. This scenario is comparable to that currently in place for wind and solar energy sources, where any excess generated energy can simply be delivered onto the network. The big issue obviously is that gas, unlike electricity, comes in a big variety of flavours. Mixing the new gases with the traditional ones has the advantage of being incremental in nature. Depending on the market situation (availability of new gases, safety and regulatory issues, progress of technology, etc.), the content of new gases in the mixture could be gradually increased, leading to a smooth and economically durable transition of the whole energy system, albeit the variety of flavours.

Figure 1.1: A bio-fermentation installation (building to the right) and storage of used fermentation material from which remnant gas is still released (building to the left) at a farm in Northwest Friesland, the Netherlands. [3]

Gas in the Netherlands

Ever since the discovery of a natural gas source at Slochteren, the Netherlands in 1959, natural gas played a prominent role in the energy supply and economy of the Netherlands. Over the years the Netherlands has established an excellent infrastructure, with 12,000 km of pipelines taking care of both high pressure and regional gas distribution. It ensured the position of the Netherlands as a major natural gas exporter and user. In the year 2009, natural gas accounted for 36.1% of the TPES of the Netherlands. 53.3% of the produced and imported gas was exported putting the Netherlands at position 7 on the list of biggest gas exporters in the world. Also, natural gas dominates the fuel mix for electricity production with an exceptionally high contribution of 51.2% [4, 5].

Obviously, the Netherlands would like to keep its position as major gas junction independent on the type of gas. Already this summer (2011), a Liquefied Natural Gas (LNG) tank in the port of Rotterdam will be taken into service to receive gas from the middle east. This tank will be connected only to a special distribution network, which is used by 80 different companies including power plants and major industry. The problem is that industrial as well as domestic gas appliances are currently setup only to deal with natural gas from within the current distribution band, which is based on the composition found in the Slochteren field (i.e. Groningen gas or G-gas). The gas from the middle east is very different in composition, forcing these companies to adapt their burners, gas motors and turbines or risk damages that can cost them up to 450 million euro's a year [6]. Except for the special industrial network, the Dutch government is planning on introducing the middle eastern gas to the domestic network in about 10 years, leaving little time to get all adaptations done.

A public debate

As can be seen in newspaper articles like [3,6,7], a public discussion is currently starting on how to maximize the potential of new gases and its impact on society. In "Sensors for New Gases" [1] Nederlandse Gasunie, the company which manages the gas transport and infrastructure in the Netherlands (including gas composition), reports that "if new gases are to be introduced successfully, the end user must first be prepared to accept them." They continue by stating that this can be done by the introduction of sensors which measure the actual composition, since it is the composition that dictates the combustion process. By combining these sensors with adaptive gas burners, it will allow for true sustainable development of the gas market.

EDGaR & the "Microsystem multi-component gas sensor platform" project

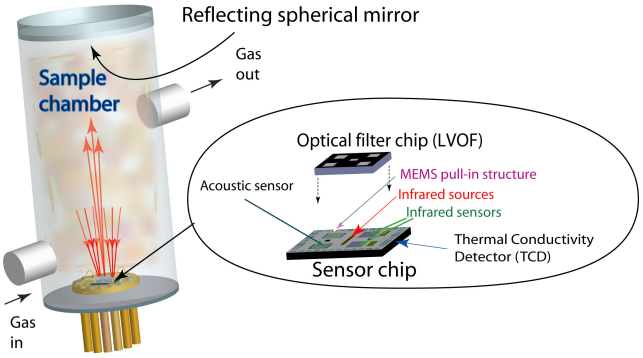

Figure 1.2: Illustration of the proposed gas sensor platform.

With the "Microsystem multi-component gas sensor platform" project, the Electronic Instrumentation (EI) Laboratory group at the TU Delft is developing a sensor platform as part of the Energy Delta Gas Research (EDGaR) program, to try and fulfil this need for the measurement of gas composition. Unfortunately, one single sensing principle is insufficient for identification of all the components in the gas mixture. It is therefore proposed to have several sensing principles on a single sensor chip, which are all based on physical interaction with the gas. Three principles have been identified as the best candidates for low-cost, reliable gas-sensing with the added constraint of possible integration on a single chip:

1. **Optical infrared absorption**: Certain gas molecules absorb infrared light. The wavelength at which absorption occurs and the amount of absorption, indicate which gas is present in what quantity.

2. **Thermal conductivity**: Gases may also be identified because they conduct heat differently.

3. **Photo-acoustic infrared absorption**: When gas molecules are excited by infrared light, their movement causes pressure changes in the gas that can be detected with a (MEMS) microphone.

1.2 Goals / Objectives

This thesis will further research the optical infrared absorption principle. The aim of this thesis is the design and development of a demonstrator infrared absorption multi-gas micro-spectrometer for the measurement of the concentrations of Carbon Monooxide (CO), Carbon Dioxide (CO_2) and Hydro Carbons (C_xH_{2x+2}) in a composite gas, and a mathematical model thereof. This model and demonstrator will then be used to answer several research questions (in order of priority):

- 1: What is the range of concentrations of the different components in the gas?
- 2: What are the limitations, restrictions and tolerances in the production process?
- 2: What is the required spectral resolution for proper concentration resolvability?
- 2: What is the required detectivity and sensitivity of the detectors?
- 3: Is there any system that could theoretically satisfy these requirements?
- 4: How much do all unknown parameters (e.g. material properties, production tolerances, etc.) influence the performance of the micro-spectrometer?
- 4: Is the model developed accurate enough to predict system performance?

The word 'demonstrator' is chosen deliberately and shows that the work done in this thesis is not that of a product design, but the important gathering of the required knowledge and demonstration of the concept including its limitations. It may act as the foundation on which further research and development can be performed, making it important to try many different options and identify those that show the biggest potential.

The choice for infrared absorption spectroscopy is made because it is a well established technique which can be cheap and very reliable, two of the most important requirements as described in section 3.2. The downside of this technique is that it will not be able to measure the concentrations of monoatomic molecules like Nitrogen (N_2), Hydrogen (H_2) and Oxygen (O_2), as is described in more detail in section 5.2. As said before, two other sensing principles will be developed in parallel, which will compensate for this limitation. It is therefore not considered an issue.

As this thesis will be the ground work for future research on the topic of micro spectrometer for the measurement of gas compositions, it will also be part of this thesis to document the required knowledge. Because only limited knowledge is present within our research group regarding optics in general and infrared absorption in particular, this particular knowledge will have to be gained from other sources.

1.3 Contributions

This thesis presents the first steps towards a micro-spectrometer capable of measuring the concentrations of several different gases for a very wide dynamic range.

To make any sort of prediction on system behaviour, a model is presented which takes every part of the system into account from the source to the detector, including all optics and of course the absorbing gas. To develop this model, the theory and physics behind every part of the system have been researched and discussed.

Also presented are a detector chip design and the design of two Linear Variable Optical Filters (LVOF's) as dispersive elements. The chip includes several detector arrays and other test

structures which should be able to give good insight in which paths to pursue further. Each of the LVOF's is designed to disperse a different part of the spectrum. One is designed for the 3-4μm window and the other for the 4-5μm window.

Besides these more theoretical contributions, there also has been put quite a bit of effort into the characterization of both the materials and fabrication process, which should further support any future design iterations. Unfortunately many fabrication issues were encountered while processing the designed chip. These issues were partly due to design errors, but mostly due to inoperable machines. This limited the amount of measurements that could be conducted on the chip and thus limits the amount of conclusions to be drawn.

However, a lot of knowledge is gained during this thesis work, which should be able to be a good foundation for further research on this topic. This thesis presents this information without skipping the problems and mistakes, giving a heads up for any future work.

1.4 Outline of the thesis

As may have become apparent already, in my opinion a thesis is a document which should present information such that knowledge can be transferred. It is therefore that a lot of effort has been put in discussing all directly related subjects into fair detail, including all the theory and physics. It is tried to present this theory such that people with only limited knowledge of optics, thermodynamics and mechanics, can still understand. This thesis should at least give a good overview of what knowledge is required to understand the problems and give a good starting point on gaining that knowledge.

In this introductory chapter the motivations for this project are stated, together with the goals and objectives that we would like to reach. A small summary on the contribution that has been made can also be found here.

Chapter two continues by introducing the concept of optical spectroscopy, including a system and model overview. It will also present a historical overview of spectroscopy and some basic knowledge about several spectral quantities that are encountered frequently in this thesis. This chapter is mainly present to give people without prior knowledge of spectroscopy a chance of understanding what this thesis is about.

Chapter three discusses the functions and requirements. These are very important to specify the project's borders, but are not considered strict as this thesis work is only part of the early stages of a bigger project.

The four subsequent chapters (Chapter four to seven), discuss the individual parts of the spectroscopy system. Depending a little bit on the part, the chapters will discuss different concepts that could fulfil the function(s) of this part by presenting the state-of-the-art, together with some of the physics involved. Thereafter the choice is made on which concept looks most promising and what research opportunities are considered interesting and useful. This concept is then further refined by presenting a model and its final design. These chapters are concluded by a description of the fabrication process.

Chapter eight will discuss the integration of several different parts and describe the read-out circuit which has been designed for the measurements to be conducted.

Chapter nine presents all the findings and performed measurements, including the setups used. The results will be discussed, which may lead to suggestions for later research.

Finally, chapter ten will summarize the conclusions and presents an overview of the suggested possibilities for future work.

The appendices include a summary of the used material properties, a detailed process flowchart and schematics and board layout designs of the read-out circuit presented in chapter eight.

Chapter 2

Background

Before we go into details, let's first get up to speed with a little bit of background information. We will start with an introduction to spectroscopy and spectroscopic systems. This section is followed by the section which will give an overview of the system. The overview presented, will be used as a guideline through this thesis. Since the field of infrared spectroscopy is closely related to many of the major scientific breakthroughs made in the past two centuries, it seems fit to continue with a short historical overview, which will directly explain some more of the terminology used. Thereafter we will discuss a couple important spectral quantities that will be used throughout this thesis. People who are comfortable with spectroscopic systems and the related terminology may skip this chapter.

2.1 Introduction to optical spectroscopy

As will be shown in more detail in the next section, more than two centuries of scientific research has discovered that the 'spectrum' of light contains a wealth of information on the matter that emits or interacts with the light. Strictly speaking, the concept of a spectrum is defined as a representation of a time function in the frequency domain. In the wave theory of light, light is considered as a sum of electromagnetic waves characterized by the oscillating frequency and direction of propagation. Applying the definition of a spectrum to the wave theory of light, it implies that a spectrum is a representation of all the intensities of waves constituting the light, depending on their frequencies (or wavelengths). A typical spectrum of the sun is shown in figure 2.1. The dips in the spectrum indicate the absorption of light by the atmosphere. Analysis of this spectrum can therefore give us information on the state of the atmosphere.

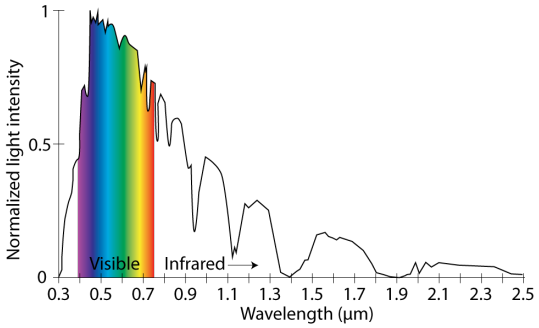

Figure 2.1: Spectrum of the sun as measured from within the atmoshpere.

To decode the information stored in a spectrum, one has to separate the light into its components and measure all the intensities. This is the task of *optical spectroscopy*; A branch of science

that extracts information about matter, by analyzing spectra. The separation of the light and the measurement is done by a so called spectrometer, the design of which is what this thesis is about.

Also several of the gases which we can expect in the future gas composition, have a distinct spectrum. It is therefore that we can use optical spectroscopy to identify these gases. Their spectra are characterized by absorption lines. This means that to obtain the spectra, we will have to shine a light with known spectrum through the gas sample and detect the difference. The amount of absorption and the wavelength at which the absorption is present, indicates how much of which gas is present in the mixture.

2.2 System overview

Now we have some knowledge of what a spectrometer is all about, we can now identify the different parts that will be required for a spectrometer. As also illustrated in figures 2.2 and 2.3, it all starts with the infrared source, which may or may not have some sort of optical filter to limit its output spectrum to the desired band. From this source, the light will travel through the sample chamber (i.e. gas cell), where the light is being absorbed by the sample material, depending on its concentration and the length of the optical path. The chamber may have further optics to direct and/or bundle the light as desired. The remaining light will then be absorbed and turned into an electrical signal by the infrared detector, which again may or may not have an optical filter to make it sensitive to a certain wavelength or band of wavelengths. This is of course also very much dependent on the type of source used.

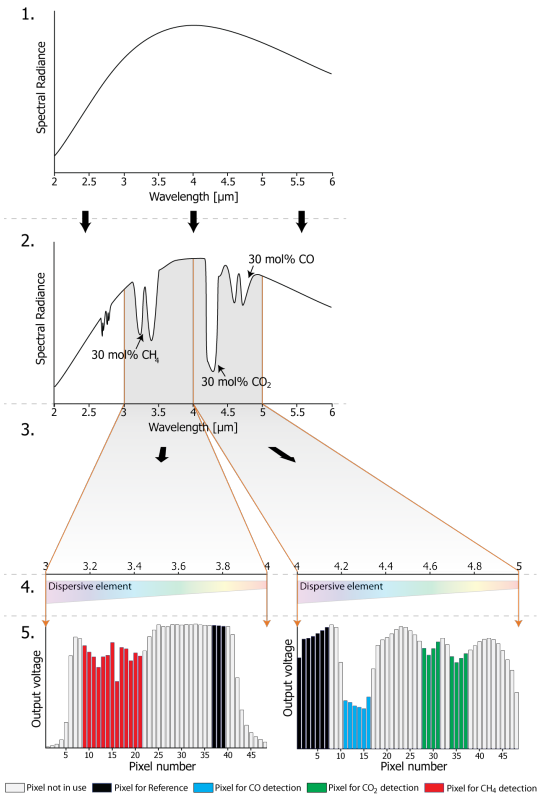

Figure 2.2: Schematic representation of a possible implementation of a spectrometer. 1. Source spectral radiance, 2. Absorption of radiance by gases, 3. Filtering and focusing optics, 4. Optics to disperse the light on the detector array, 5. Signal output of detector array.

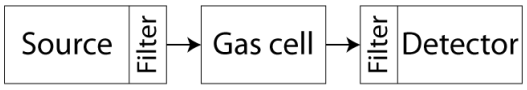

Figure 2.3: Universal schematic representation of a gas spectrometer setup. This figure will be used throughout this thesis to indicate which part of the spectrometer will be discussed

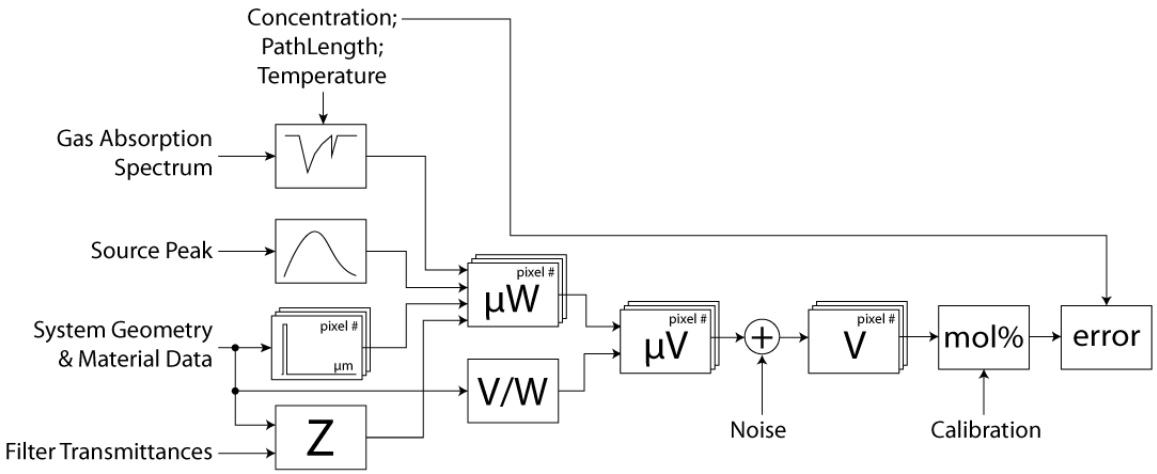

Figure 2.4: Schematic block diagram of the system's model.

2.2.1 System model overview

To predict the system's performance and compare different design concepts, a model has been written using the MathWorks® MATLAB® software. A schematic overview of the model is shown in figure 2.4.

As shown, it models the complete system. Key features are the broad range of possible designs it can simulate, its modular build up and capability to calculate the outputs for several different gas compositions in a single iteration. Because of the modular build up, users can easily adapt the model to their needs.

It starts by calculating four parameters as a function of the user inputs: Gas absorption spectrum; Source output; Spectral window for each individual pixel as a result of the dispersive element; Optical throughput of the system. These will be used to determine the absorbed power by each pixel. Next to this, also the responsivity of each pixel is calculated. Together the latter two will give the output voltage of each pixel. The noise of the pixel and the amplifier are added before the amplification stage, after which the read-out algorithm can calculate the gas composition with the help of calibration data. Finally the calculated gas composition can be compared to the input to reveal the error.

All the different parts of the model will be discussed in much more detail throughout this thesis. The sections where the models of the different parts are presented, will start with "Cell title" and "Sub-function(s)". These are to indicate where to find this part model in the system model and which sub-functions are related. The system model is build up from several MATLAB™ files. All the parameters that may be changed by the user are found in the "NDIR_Sensor_Model_UI.m" file. The actual work is done by the "NDIR_Sensor_Model" function which will occasionally call sub-functions. All functions are saved as a separate file to keep it orderly. All the part models are put in a separate cell, which can easily be identified by the cell title.

2.3 A short historical overview

As will be shown in detail in chapter 5, the absorption lines of interest for this application are all situated in the mid to far infrared of the spectrum (>3μm). Infrared radiation itself was only discovered in 1800 by Sir Frederick William Herschel. He performed an experiment where he basically build a crude monochromator that used a glass prism to disperse the light and a thermometer to measure the temperature across the spectrum. Two decades later in 1821, Thomas Johann Seebeck discovered the thermoelectric effect and soon thereafter demonstrated the first thermocouple. This discovery was followed in 1829 by the first thermopile by Leopoldo Nobili and a further refined version by Macedonio Melloni in 1833. The development of the thermopile proved to be the key to unlock many of the mysteries of thermal radiation. [8]

Melloni also first speculated about the presence of absorption bands in the earth's atmosphere, which would later be verified by Armand Hippolyte Louis Fizeau and Jean Bernard Leon Foucault. The first study into possible absorption bands in different gases was made by John Tyndall. Although many more studies would be performed using Melloni's detection system, there soon was a need for still higher sensitivity. In response to this need, the decade 1880-1890 saw the introduction of three new high-sensitivity devices: The bolometer by Samuel Pierpont Langley, the radiometer by Ernst Pringsheim Sr. and the radiomicrometer (or microradiometer) by Sir Charles Vernon Boys. [8]

Figure 2.5: Sir Frederick William Herschel during his experiment with which he discovered infrared radiation. [9]

With improvements in detectors of infrared radiation came an accompanying need for improvement in optical materials and components. Joseph von Fraunhofer played a very important role in this part. First of all, he managed to create the world's finest optical glass. Later in 1814, he would invent the spectroscope which utilized a prism to disperse the light. Several years later in 1821 he would improve his spectroscope by developing a diffraction grating [8, 10]. In 1880 Albert Abraham Michelson devised an interferometer together with Edward Morley with which they would conduct the later called Michelson-Morley experiment to disprove the existence of "luminiferous aether" (e.i. light-bearing ether). This basic design is still very much in use in so called Fourier Transform Infrared (FTIR) spectrometers (See also section 6.3.1). About a decade later, Charles Fabry published two papers on the visibility and orientation of interference fringes. Working closely with Alfred Pérot between 1896 and 1902 resulted in the development of the now widely used Fabry-Pérot interferometer. Which in Fabry's own words was "partly by chance, following an observation in an electrical problem". [11]

In 1889, Langley said that there was one great problem to be solved: The relation between

temperature and radiation. At that time there were only two useful radiation laws for blackbody radiation. The first is the well-known relationship established by Gustav Robert Kirchoff. The second, the empirical relation of Joseph Stefan defined in 1879, which was theoretically validated by Ludwig Edward Boltzmann in 1884, and is now known as the Stefan-Boltzmann law. A major step forward in blackbody theory was the derivation of the Displacement Law by Wilhelm Wien, which related the position of maximum energy in a blackbody spectrum and the temperature of the source (see also Section 7.5.2.4). Most importantly, the work of Wien provided the experimental data used by Max Karl Ernst Ludwig von Planck to check the accuracy of his equation he derived around 1900. The consequences of his assumption that energy was not continuous, but quantized, was of course an indescribable breakthrough in physics, leading to the completely new field of quantum physics. This in turn lead again to a much better understanding of the infrared absorption peaks and would improve both thermal and photodetectors. In the particular case of photodetectors for example it lead to Albert Einstein's explanation of the earlier discovered photoelectric effect by Heinrich Hertz, on which many photodetectors are based today.

Although some very basic infrared spectroscopy had been done by Langley and several other physicists, William Weber Coblentz laid the real groundwork for infrared spectroscopy. Starting in 1903 he investigated the spectra of hundreds of substances, both organic and inorganic. The fact that infrared absorptions arise from molecular, not atomic, activity was first established by the work of Knut Johan Ångström, when he showed that carbon monoxide and carbon dioxide had different spectra. The end result of these early studies was the recognition that each compound had a unique IR spectrum and that certain groups, even when they were in different molecules, gave absorption bands that were at approximately the same wavelength. [8, 12]

At the beginning of the new century most of the physics involved in spectroscopy was well understood and had a proper mathematical description. Only the semiconductor physics was still in its infancy and needed further development. Other challenges were improving the fabrication and material technologies to further increase sensitivity and reliability, whilst reducing cost. They would all be developed for the extremely fast growing microelectronic industry sparked by the invention of the transistor in 1947 by John Bardeen, Walter Brattain and William Shockley.

In 1958, Jack Kilby of Texas Instruments built the first integrated circuit (IC) using germanium (Ge) devices. Later that same year, Rober Noyce of Fairchild Semiconductor announced the development of a planar double-diffused silicon (Si) IC.

Richard Feynman's "There's plenty of room at the bottom" was presented at a meeting of the American Physical Society in 1959. This talk popularized the growth of micro- and nanotechnology by challenging the audience to write the entire 24 volumes of the Encyclopaedia Brittanica on the head of a pin by scaling it down 25000 times and to create an operating electric motor which fits in 1/64 inch^3. Both challenges were awarded \$1000 and kick-started the development of MicroElectroMechanical Systems (MEMS).

In 1964, Harvey Nathanson from Westinghouse produced the resonant gate transistor. It was the first batch fabricated MEMS device, which joined a mechanical component with electronic elements and served as a frequency filter for ICs. It was also the first demonstration of the surface micromachining technique, where layers are grown or deposited on top of the substrate which can than act as sacrificial or structural layer. By etching away the sacrificial layers, the structural layers remain and define the desired geometries. The term surface micromachining would only come into existence in the early 1980s.

During the early 1960s, germanium was quickly replaced by silicon. Silicon emerged as the dominant material, because it was found to have two major processing advantages. Silicon can easily be oxidized to form a high-quality electrical insulator, and this oxide layer also provides an excellent barrier layer for the selective diffusion steps needed in the IC fabrication. Silicon was also shown to have a number of ancillary advantages. Having sand (SiO_2) as the base ingredient

for the production of silicon, it is a very abundant element in nature, resulting in potentially lower material costs. It also has a wider bandgap than germanium and can therefore operate at higher temperatures [13]. Due to the popularity of Si, much effort was put into developing Si processing and characterization tools, which is why there still is a more abundant amount of information on the use of Si then any other material.

Since the invention of the microprocessor in 1971 by Intel, the complexity of ICs has doubled every two to three years, leading nowadays to the integration of just shy of a billion transistors on a 216 mm^2 chip [14]. To be able to keep up with this trend, also known as Moore's law, IC fabrication depends on increasingly sensitive sensors and actuators to provide input and control the surrounding environment. As is the case for all other control systems, ranging from those in the transportation sector to health-care to consumer electronics.

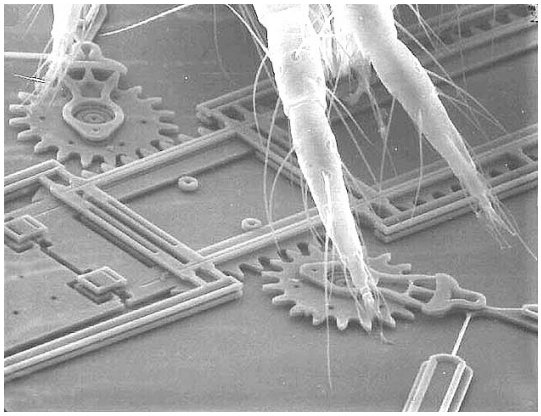

Figure 2.6: A MEMS device, where the gears are dwarfed by the legs of a spider mite.
Photo: Sandia National Laboratories, SUMMiT Technologies.

One of the first MEMS considered to be a commercial success, was the Si pressure sensor. The success of this MEMS sensor was mainly due to the discovery in 1954 that the piezoresistive effect in Ge and Si is about 10-20 times greater than that of their metal counterparts. The first high volume pressure sensor was marketed by National Semiconductor in 1974. Si pressure sensors are now a billion-dollar industry.

This increasing demand for highly sensitive sensors and actuators kept the research into MEMS devices going. Since the 1960s many new fabrication techniques have been developed like Bulk micromachining, the LIGA process and (Deep) Reactive Ion Etching (DRIE). Bulk micromachining refers to the selective etching of the Si substrate (i.e. bulk), in order to leave behind the desired geometries. The LIGA process allows for manufacturing of high aspect ratio microstructures. DRIE is a highly anisotropic etch process used to create deep, steep-sided holes and trenches in wafers.

Also advances were made in the growth and depositioning of different materials on the glass or Si substrate. Examples of this are the (further) developments of molecular beam epitaxy (MBE), chemical vapor deposition (CVD) and sputtering. The challenge here is often to create uniform and defect free materials.

Combining these techniques, more and more structures were developed including beams, gears, diaphragms, springs, electrostatic actuators and mirrors. In the 1990s manufacturing processes also started to allow for the monolithic integration of microelectromechanical structures with driving, controlling and signal-processing electronics. This integration promises to improve the performance of MEMS devices as well as reduce the cost of manufacturing, packaging and instrumenting these devices, increasing the amount of applications where MEMS could be used.

Even today, still a lot of work is to be done. Application specific devices are being researched and developed every day, while technology progresses and gives rise to new opportunities.

2.4 Spectral and radiometric quantities

Throughout this thesis one will encounter several spectral and radiometric quantities that will keep reoccurring. The nomenclature, symbols and units of these quantities may vary throughout literature. This section will therefore briefly discuss these quantities as they are used in this thesis and may prove useful for later reference during reading. The definitions of the radiometric quantities are adopted from [15].

2.4.1 Wavelength, frequency and wavenumber

Depending on spectral region and application, different ambiguous quantities are used to describe the radiation wave. It is for example common to describe a monochromatic radiation by its *wavelength*, λ, rather than by *frequency* [Hz], ν. In the infrared region of the electromagnetic spectrum, the usual measurement unit of wavelength is micrometer (μm), where in the visible the nanometer (nm) is more convenient. In spectroscopy, *wavenumber*, $\bar{\nu}$[cm^{-1}], is the most commonly used quantity.

In fact they all describe the amount of energy present in a radiation package (i.e. photon):

$$E = h\nu = hc_0\bar{\nu} \cdot 10^2 = \frac{hc_0}{\lambda_{\text{nm}} \cdot 10^{-9}} = \frac{hc_0}{\lambda_{\mu\text{m}} \cdot 10^{-6}} \tag{2.1}$$

where h [J s] is Planck's constant and c_0 [m s^{-1}] is the speed of light in vacuum.

This thesis will be using the wavelength in [μm] as quantity to describe the electromagnetic waves. The main reason for this is that the dispersive element chosen in the final design is linearly dependent on the wavelength. Modeling in wavelength is therefore considered the most intuitive.

2.4.2 Resolving Power

The *resolving power*, RP, quantifies the ability of an element to separate (i.e. resolve) adjacent spectral lines of average wavelength λ_0. It is defined as a dimensionless number:

$$RP = \frac{\lambda_0}{\Delta\lambda} \tag{2.2}$$

Here, $\Delta\lambda$ is the minimum difference of wavelengths that generates two intensity peaks that can be discriminated. Depending on which criterion is used, slightly different values for $\Delta\lambda$ can be found as illustrated in figure 2.7. Classically, the Rayleigh criterion is used, which is determined by what the human eye can distinguish. A more modern approach is the Full Width Half Maximum (FWHM) (i.e. Taylor) criterion, which is based on the use of detectors, slightly relaxing the Rayleigh criterion and simplifying the equations.

2.4.3 Free Spectral Range (FSR)

Dispersed light almost always exhibits some sort of periodicity. This reoccurance of light of the same wavelength at different positions limits the spectral range of the dispersive element before several wavelengths will occur at the same spot, resulting in an unambiguous signal. The spectral range within which no overlap of wavelengths will occur is called the *free spectral range* and is illustrated in figure 2.8.

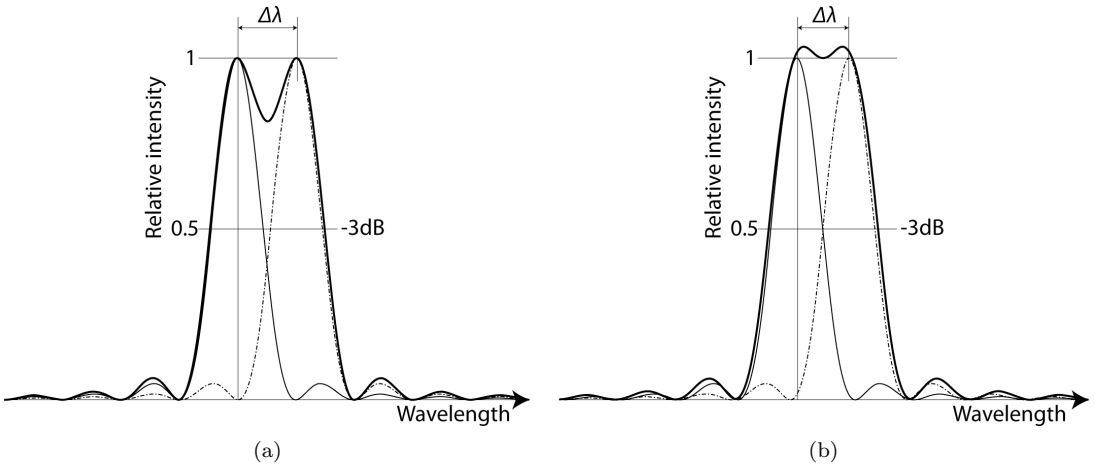

Figure 2.7: Two spectra at minimum resolvable distance according to (a) the Rayleigh criterion and (b) the FWHM (i.e. Taylor) criterion.

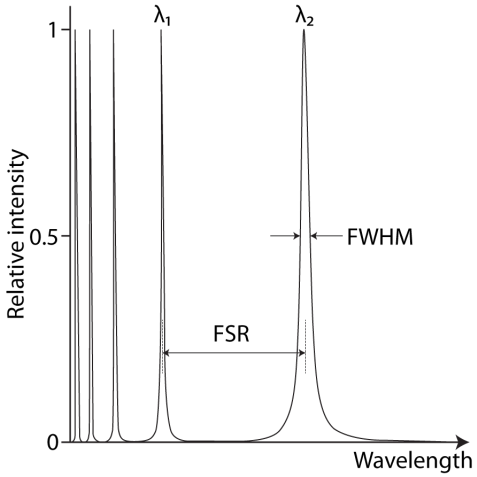

Figure 2.8: Free Spectral Range in a Fabry-Perot interferometer.

2.4.4 (Spectral) Power

The amount of energy transferred per unit time is defined as power, P [W] and is given by:

$$P = \mathrm{d}Q/\mathrm{d}t \tag{2.3}$$

Where Q is the amount of energy and t is the time.

We refer to spectral power, $P_\lambda(\lambda)$ [W μm^{-1}], as the power around wavelength λ, found in the wavelength interval dλ. We denote the spectral quantities with the subscript λ, explicitly indicating a derivative with respect to the wavelength. The majority of sources, emit the radiation

in a wide wavelength interval. For those, the spectral power is defined as:

$$P_\lambda(\lambda) = \mathrm{d}P(\lambda)/\mathrm{d}\lambda \tag{2.4}$$

2.4.5 (Spectral) Exitance and Incidence

One of the important concepts to keep in mind is that the radiation is only generated or absorbed by matter, whose spatial extent is defined by its surfaces. As the surface of a material modifies the radiation, it is found to be preferable to differentiate between the radiation before it is incident on the surface and after it is reflected of the surface. The power density for the radiation incident on the surface is called the *incidence* (also often named *irradiance*) and is denoted by E in [W m^{-2}]:

$$E(x, y, z) = \mathrm{d}P/\mathrm{d}A \tag{2.5}$$

The spectral incidence, E_λ [W m^{-2} $\mu\mathrm{m}^{-1}$], is similarly defined for each spectral component:

$$E_\lambda(x, y, z) = \mathrm{d}P_\lambda/\mathrm{d}A \tag{2.6}$$

The radiation leaving the surface, either generated by the matter or reflected from it, is described by the term *exitance* and is denoted by M with units [W m^{-2}]:

$$M(x, y, z) = \mathrm{d}P/\mathrm{d}A \tag{2.7}$$

The spectral exitance, M_λ [W m^{-2} $\mu\mathrm{m}^{-1}$], is similarly defined for each spectral component:

$$M_\lambda(x, y, z) = \mathrm{d}P_\lambda/\mathrm{d}A \tag{2.8}$$

2.4.6 (Spectral) Radiance

The propagation of the radiation may be guided or manipulated using one or more optical components. This will result in a change in power density from one point to the next, along the propagation path. The imaging optics, such as lenses and mirrors, change the angular distribution of the radiation in order to modify the spatial extent and direction of propagation of radiation.

Sources typically emit radiation with an angular dependence that is a consequence of the source's physical characteristics, shape, form, layout and construction. Additionally, the sources typically do not generate the power uniformly over its surface area, due to the surface non-uniformity.

The *radiance*, L [W m^{-2} sr^{-1}], is a quantity that is suitable to characterize both these spatial and angular radiative properties of an extended source (i.e. a source that has appreciable area compared to the square of the viewing distance) and is given by:

$$L(x, y, z; \theta, \phi) = \frac{\partial^2 P}{\partial A_p \partial \omega} = \frac{\partial^2 P}{\partial A_s \cos\theta_s \partial \omega} \tag{2.9}$$

where ω is the solid angle in steradians, [sr], A_p is the projected source area in [m^2], A_s is the source area and θ_s is the angle between the normal of the source and the line of sight. A more detailed explanation of the (projected) solid angle can be found in section 5.3.1 and [15].

Again we can also define the *spectral radiance*, L_λ [W m^{-2} sr^{-1} $\mu\mathrm{m}^{-1}$], as:

$$L_\lambda(x, y, z; \theta, \phi) = \frac{\partial^2 P_\lambda}{\partial A_p \partial \omega} = \frac{\partial^2 P_\lambda}{\partial A_s \cos\theta_s \partial \omega} \tag{2.10}$$

The radiance is considered to be the most appropriate quantity to characterize the transfer of radiative power in an optical system.

Chapter 3

Functions and requirements

Before any attempt is made to make a detailed design of any of the parts, it is important to properly describe the functions and requirements that have to be fulfilled. The project definition is more or less already given by the motivation and goals as described in chapter 1. The next step is to make an abstraction of this description and look for the fundamental functions. This abstraction will allow for a clear view of what has to be designed, hopefully leading to a better design in the end.

3.1 Functional description

Using a top-down approach, first a description of the function of the complete sensory system is made.

- The measurement of the composition of the (new) gas at the end-user to extract data required for the control of the combustion process.

The fact that the physical principle on which the sensor is based is determined to be infrared absorption, narrows this very general function down to a more manageable one:

- The quantitative measurement of Carbon Monooxide (CO), Carbon Dioxide (CO_2) and Hydro Carbons (C_xH_{2x+2}) in the gas sample provided, using infrared absorption.

Without making any design choices, this can be further specified as a function for the emitter, the sample chamber and the detection system.

- Emitter: A source of light with a spectrum that has sufficient output in the absorption bands of the gases to be detected.
- Sample chamber: A container for the gas sample, such that it will allow for a proper measurement.
- Detector: The transduction of infrared light into an electric signal that can be used to determine the amount of CO, CO_2 and C_xH_{2x+2} in the gas sample.

3.2 Requirements

To further specify the project, a list of requirements is set-up based on those described in [1,16,17]. Important to notice here is that these requirements were merely used as a guideline. As described in section 1.2, the purpose of this thesis is to design a demonstrator only, which is also why some requirements might be considered somewhat vague or under defined. Still, the definition of requirements is considered important to give the proper focus to the project and allow for certain design decisions to be made.

One such requirement is the spectral window in which to look for the absorption peaks. Although one gas can have several absorption peaks, the choice has been made to focus on the 3-5 μm window. This window is chosen for several reasons. First there are clear absorption peaks for carbon monoxide, carbon dioxide and hydrocarbons. Second, the photon energies are still big enough to allow for fairly easy detection (0.414 eV to 0.248 eV). Last, the thickness of optical thin-film filters scales with the center wavelength, so long wavelengths require thick films, making production of these filters more difficult and expensive.

The range of gases that have to be detected is still under investigation by KEMA. Still a preliminary table has been presented which shows what can be expected. The numbers are given in mol %.

	CH_4	**C_2H_6**	**CO_2**	**CO**	**N_2**	**H_2**
Ideal range	0-100%	0-14%	0-40%	0-40%	0-30%	0-100%
Groningen gas	81%	2%	1%	-	14%	-
LNG	87%	12%	-	-	1%	-
Gasification of coal	0-0.03%	-	2.1-5.9%	1.6-5.5%	7.5-11.3%	79.6-84.9%
Gasification of Biomass*	0-22%	0-5%	2-22.9%	8.9-70%	0-53%	5-45%
Fermentation gases*	48-85%	-	15-52%	-	0-3%	-

Table 3.1: Preliminary overview of the range of gas compositions that ideally should be acceptable in the future, the compositions of the gases currently in use and the compositions of gas which can be expected from different resources. *Strongly dependent on the raw material and the technique used.

- Reliable
  - Should not need recalibration during lifetime
  - Has an average lifetime of several years
- Small
  - Source and detector fit on 1/3 of a 15x15 mm^2 die each
  - Sample chamber is only a couple cubic centimeters
- Cheap (Up to €100 or so)
- Works in a temperature range of 260 - 320 K
- Is able to cope with a gas pressure of 38mBar (+/- 5mBar) (overpressure)
- Has a selectivity which is within 5% of the physical limit (i.e. the limit due to overlapping absorption spectra).

- Has a dynamic range suitable for the detection of the range of gas compositions that ideally should be acceptable in the future as stated in table 3.1, excluding the undetectable monoatomic molecules (e.g. H_2 and N_2)
- All gases can be detected simultaneously
- Uses the absorption peaks with a wavelength between 3 and 5 μm
- Production process is IC compatible, such that the basic detector and any on-chip circuitry are realized with a standard CMOS process and further post processing is kept to a minimum

The selectivity requirement is dependent on the spectral window used to determine the quantity of a certain gas.

Chapter 4

Infrared sources

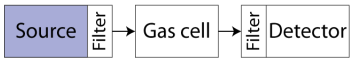

4.1 Introduction

The development of an infrared micro-spectrometer basically starts with the choice of its source. This choice is very important because it may have a big influence on the whole system design. Important parameters are:

- Shape and/or tunability of the emitted spectrum
- Its external quantum efficiency (i.e. the ratio of the radiated power and the input power)
- Maximum modulation depth for a certain operating frequency
- Cost
- Possibility of integration

The operating frequency can be important for two reasons. First, it will allow for coherent detection with a lock-in amplifier, improving the signal-to-noise ratio. Second, if pyroelectric detectors are used, one requires the amplitude modulation for them to work at all.

We can identify three different types of sources which are commonly used in infrared systems: Thermal sources, Light Emitting Diodes (LED's) and lasers. All will be discussed only briefly since this thesis will not report about the design of an infrared source, but will merely decide on which type fits this application best. The final choice of which will be made in section 4.5. Thereafter, a model to describe the optical output of the source will be discussed, which is used in the earlier presented full system model.

4.2 Thermal sources

This is the most basic and therefore cheapest infrared source. A filament is heated to radiate a wide band infrared spectrum depending on the temperature of the filament. Temperatures may rise up to $\gg$1000 K, depending on the required position of the spectral peak. This temperature is a source of concern for several reasons. First, we are dealing with flammable gases, which we obviously do not want to ignite. Second, the heat may cause the filament itself to burn if oxygen is present. Third, the heat may cause the structural integrity of the filament to degrade. It would therefore be required to operate this type of source in a vacuum chamber, such that it is not in contact with both the gas to be detected and the outside air.

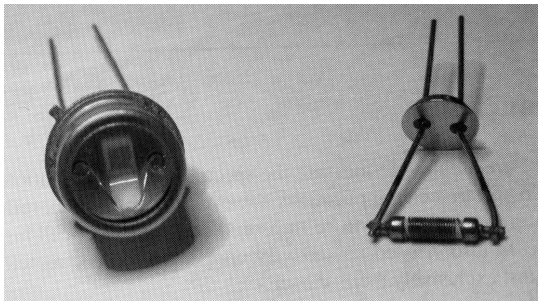

Figure 4.1: A thin-film (left) and a wire-wound (right) thermal infrared source. [18]

As said, the emission spectrum of a thermal source is very wide band and can be approximated by that of a grey or black body source, as will be further discussed in section 7.5.2.4. The main dependency of output spectrum on the temperature of the filament, makes it very easy to tune the output spectrum. This allows the emitted infrared radiation to be stabilized against environmental changes (e.g. ambient temperature, air flow, humidity) as well as against the effects of long-term drift (e.g. electro-migration, inter-diffusion, etc.) [19]. The efficiency is very much dependent on how well one can make the source approximate the perfect black body.

One area where the thermal source is always outperformed is that of modulation speed. The thermal inertia of the source makes it a relatively slow device. By minimizing the thermal mass, one can improve the speed. Reports have been made of sources that have a nearly full-scale modulation depth up to 50 Hz [20]. However, the amount of radiated power is also dependent on the size of the source. Therefore a trade-off will have to be made between output power and modulation speed.

4.3 Light Emitting Diodes (LED's)

LEDs also offer a possible alternative for wavelengths < 5 μm. However, they are expensive and the obtained output power is in the range of only a few μW, with an FWHM linewidth in the order of 0.1 λ_{max}. In contrast to thermal sources, LEDs can be modulated at frequencies >100 Hz and could be safely used in direct contact with the gas. For the physical principles behind the workings of an LED, the reader is referred to [21].

4.4 Lasers

Mid-infrared lasers exist in the form of, for example, Quantum Cascade (QC) lasers or lead-salt lasers [22–25]. These have a very high and narrow emission. Their biggest disadvantage is cost

and the difficulty of downscaling. At this moment there is no report yet on cheap, micro-sized mid-infrared lasers.

4.5 Concept choice

Looking at the application, it seems quite clear that a laser is not going to fulfill the requirements. First of all, it has a very narrow output spectrum, requiring several lasers to detect all the gases. Second, lasers are usually relatively expensive. Last, infrared lasers are, at this moment, considered bulky.

Although the LED has a somewhat broader spectrum, it is still fairly small ban and only has limited output power. Moreover, mid infrared LED's may require non-standard IC materials or processes limiting their ability to be integrated, and are still considered somewhat expensive with tens of Euro's per LED. On the other hand, LED's are very simple to modulate up to high frequencies, which gives the ability to do coherent detection at frequencies far from the main noise sources, increasing the signal-to-noise ratio.

Depending a little bit on the design, a thermal source can closely represent a black body source and could be easily integrated with the other parts. The thermal source is thus very wide band and can cover the complete range with a single device. Even better, the source could be easily tuned by simply changing the temperature of the filament. On the other hand, the thermal inertia of such a source can be quite large, reducing the maximum modulation frequency.

All-in-all, the thermal source seems to be the infrared source that fits the specifications of this application best, mainly because of cost and integration issues. As said before, the design of a source is considered outside the scope of this thesis.

4.6 Modeling

Cell title(s): SOURCE OUTPUT CALCULATIONS
Sub-function(s):

Since this thesis does not include the design of an infrared source and assumes the source to be of the thermal type, the basic source is modeled as a black body with both its emissivity as a function of view angle, ε_θ, and as a function of wavelength, ε_λ, as input parameters. It is assumed that the emissivity as a function of view angle is symmetric around the normal axis of the source. A more detailed discussion on radiation, including derivations of the equations used, can be found in section 7.5.2.4. The user can define the wavelength at which the emission peak should occur, λ_{peak}, and the physical dimensions of the source. The emission peak is used to calculate the temperature of the source, T_s [K], as:

$$T_s = \frac{b}{\lambda_{peak}} \tag{4.1}$$

where $b = 2.898 \cdot 10^{-3}$ is Wien's constant. The outcome of which is used to calculate the spectral radiance of the perfect black body as also shown in figure 4.2.

$$L_{\lambda,bb}(\lambda, T) = \frac{2 \cdot 10^{-6} h c_0^2}{\lambda^5 e^{hc_0/\lambda k T_s} - 1} \tag{7.30}$$

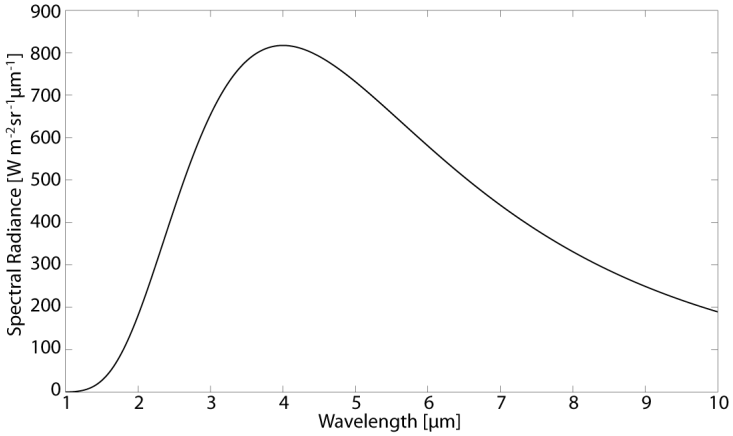

Figure 4.2: Perfect black body example of a possible simulated source output.

The user can define data files, in which the emissivity factors can be found, where $0 \leq \varepsilon \leq 1$ and $-\pi/2 \leq \theta \leq \pi/2$. The look-up table, "*Source.Radiance*", is created in which one can find the spectral radiance of the source as function of both the view angle and wavelength.

As a sanity check, also the total emitted power by the source, P_s [W], is calculated by using the Stefan-Boltzmann equation:

$$P_s = A_s \cdot \sigma \cdot T_s^4 \tag{4.2}$$

where A_s is the area of the source and $\sigma = 5.6704 \cdot 10^{-8}$ is the Stefan-Boltzmann constant .

Chapter 5

Gas cells

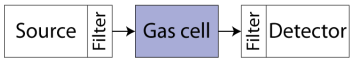

5.1 Introduction

The gas cell is that part, through which the gas will flow, such that it can be measured. Except for the containment of the gas, it might also act as part of the optics to direct the light from the infrared source to the detector.

This chapter will mainly discuss the physics of the optics, how infrared light is absorbed by the different gases and different options on how to use both of these theoretical backgrounds in a computer model. This model is subsequently used to determine the required length of the path along which the light has to travel through the gas composition, in order to meet the requirements as stated in section 3.2.

5.2 Infrared absorption: The physical origin

When we look at the resulting spectrum of light traveling through a composite gas, we can see that some of the gases will absorb part of the light. How much is absorbed and at which wavelength depends on both the quality and quantity of the composite gas. This section will explain the physics behind this mechanism and explain several options on how to model it. In figure 5.1, the line intensities of the gases on which this thesis will be focused are given. From this we can derive the absorption, as will be explained subsequently.

The absorption of light by matter originates from the interaction between the radiation from a light source and the chemical bonds of the sample. More precisely, if the atoms situated at the two extremes of a bond are different, they form an electric dipole that oscillates with a specific frequency. Only those photons that are radiated with an energy corresponding exactly to the energy gaps (as defined by the selection rules dependent upon the quantum numbers), will be absorbed by the molecule. Since the allowed energies (and therefore frequencies) are dependent on the bond and the atoms of the dipole itself, every molecule has a certain fingerprint. Mainly the mid infrared is a spectral range in which many gases have their uniquely defined absorption peak(s). It is therefore that the structure of the infrared absorption spectrum of a gas can be used to derive its composition. Also this simplified approach can be used to rationalize that in the absence of a permanent dipole, which is the case with molecules like Oxygen (O_2), Nitrogen (N_2) and Hydrogen (H_2), there will be no coupling with the electromagnetic wave and therefore

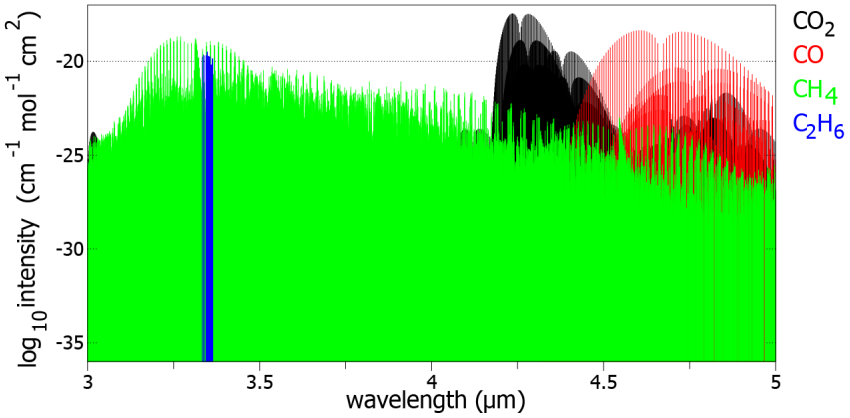

(a)

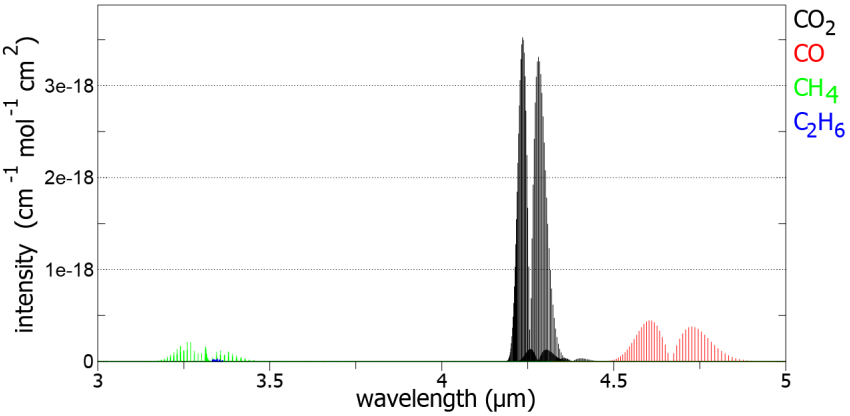

(b)

Figure 5.1: Molecular line intensities of Carbon Dioxide (CO_2), Carbon Monooxide (CO), Methane (CH_4) and Ethane (C_2H_6) at $T_0 = 296K$ as presented in HITRAN2008. Plotted (a) on a log scale and (b) on a linear scale. (At the courtesy of SpectralCalc.com)

no absorption of energy will take place, making these bonds transparent to the mid infrared radiation. [26]

Except for when the temperature is 0 K, atoms within molecules are in perpetual motion. For the purpose of study, we can compare molecules with harmonic oscillators (rotators and vibrators) kept in a stable dynamic state which depends on the interactions between the atoms and varies with temperature. Each atom within the polyatomic molecule possess three degrees of freedom, which refer to the three classic Cartesian coordinates. All these movements confer upon each isolated molecule a combined mechanical energy. The total energy of a molecule is represented to a first approximation by an expression of the form:

$$E_{\text{tot}} = E_e + E_v + E_r \tag{5.1}$$

Where:

- E_e is the electronic molecular energy, associated with the distribution of electrons in the orbits of atoms;
- E_v is the vibrational energy, associated with the vibrations of the nuclei of the atoms around an equilibrium configuration of the molecule;
- E_r is the rotational energy, corresponding to the movement of the whole molecule around its center of mass.
- $E_e >> E_v >> E_r$

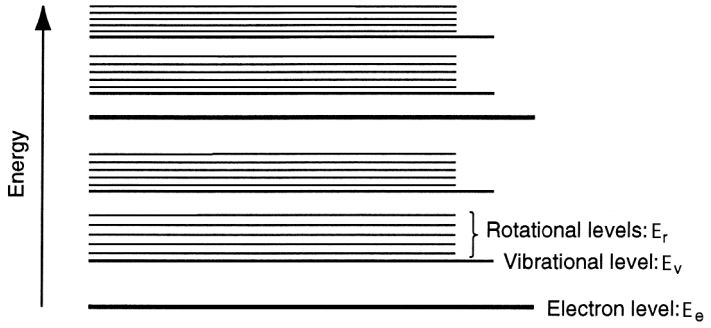

Figure 5.2: Energy states

The values of these energy levels are in different orders of magnitude and, according to the Born-Oppenheimer approximation, they can vary independently of each other, though they are all quantified. Figure 5.2 makes the relative spacing of these energy levels clear: The electron levels are resolved into a number of vibrational levels, each being in turn composed of more closely spaced rotational sublevels. The amount of energy involved in a transition between two energy levels is directly dependent on the frequency of the photon being absorbed or excited and is described by (see also section 2.4.1):

$$\Delta E = \Delta E_e + \Delta E_v + \Delta E_r = h\nu = hc_0\bar{\nu} = \frac{hc_0}{\lambda} \tag{5.2}$$

Each of the left hand terms represents a variation between the electron, vibrational and rotational energy levels, respectively. We can therefore observe the following three types of spectra:

1. **Rotation spectra**: the electronic molecular energy and the vibrational energy do not change ($\Delta E_e = \Delta E_v = 0$). These low energy spectra appear in the spectral region covering from the far infrared through to microwaves;
2. **Vibration-Rotation spectra**: these are linked to the changes in E_v to which some variations in E_r are generally associated. Only the electronic molecular energy remains unchanged. The spectrum is formed of bands corresponding to the vibrational transitions which are composed of lines associated with the rotational transitions. Because the steps between the rotational energy levels are greater (~ 0.1 eV), these spectra are encountered in the near and medium infrared.
3. **Electron spectra**: constituted of a system of bands, each associated with a value of $\Delta E_e/h$. The steps are again greater ($\sim 1 - 10$ eV) and are therefore located in the ultraviolet to near infrared.

As described in section 3.2, this thesis is focused on the mid infrared region. Therefore only Vibration-Rotation spectra will be further discussed.

A molecule formed from N atoms possesses $3N$ degrees of freedom, defined with respect to its center of gravity. In general, we can also identify 3 translational modes and 3 rotational modes. From this, we infer that there remain $3N - 6$ normal vibration modes. If the molecule is linear (like CO_2), there remain $2N - 5$ vibration modes. Calculation reveals that even simple molecules such as propane, C_3H_8, has 27 fundamental vibrations, and therefore, it might be predicted that it will have 27 bands in the IR spectrum! Happily this is not entirely true. First of all, not all of these vibrational states are active, since there must first be variation in the dipole moment to get an absorption. Second, some bands might be either superimposed or degenerate. Still, such a high number of energy levels, to which are added combinations of levels and harmonics, can only lead to complex and unique spectra for each compound. This is why this technique is so interesting for the purpose of gas composition determination.

Theorists have come up with several models to try and predict the absorption spectra of different molecules. [26]. Treatment and discussion of these models is considered outside the scope of this thesis, since they will not be used. However, some notes, which can be deducted from the study of these models, will be mentioned to further understand the empirically gathered absorption data.

The vibrational transitions rarely appear on their own. They are usually accompanied by a change in the rotational level as well, which has the effect of giving rise to series of lines associated with the rotational transitions around the vibrational transition frequency ν. The set of lines constitute a band, each band being composed of two branches situated either side of ν. The frequency at which the lines are positioned are defined by equation (5.2), which , if we assume a constant electronic molecular energy, can be rewritten as:

$$\nu = \frac{1}{h}(\Delta E_v + \Delta E_r) \tag{5.3}$$

Nevertheless only certain transitions can be seen. They are determined at first by the vibrational selection rules, then by the rotational rules for the band considered. For the quantum vibration number, V, and quantum rotation number, J, a diatomic molecule will have the selection rules: $\Delta V = \pm 1$ and $\Delta J = \pm 1$. The transitions $\Delta V = \pm 2, 3, ...$ equally produce some harmonic lines, but the probability of the transition, and therefore the line intensity, decrease very quickly as ΔV increases.

In an absorption spectrum, the lines $\Delta J = -1$ compose the so called P-branches and the $\Delta J = +1$ compose the R-branches. Certain molecules, amongst them being linear triatomic molecules such as CO_2, produce as well as P- and R-branches, a Q-branch, associated with the transition $\Delta J = 0$. The lines belonging to this branch appear in the neighborhood of the center of the band.

The amplitude of a line is tied to its intensity which depends on the probability of the occurrence of the transition concerned. The bands have consequently a characteristic envelope whose general shape is represented in figure 5.3. The R-branch is in general more intense than the P-branch.

It can be imagined fairly easy now that the shape of the spectrum will be dependent on temperature as well, since this will increase the energy state of the gas. This will result in a higher probability for the higher order lines to occur, increasing their intensity. Obviously, the total probability remaining 1, this will result in a reduced probability of the lines closer to the center frequency, shifting the maxima of the branches away from the center of the band as shown in figure 5.4

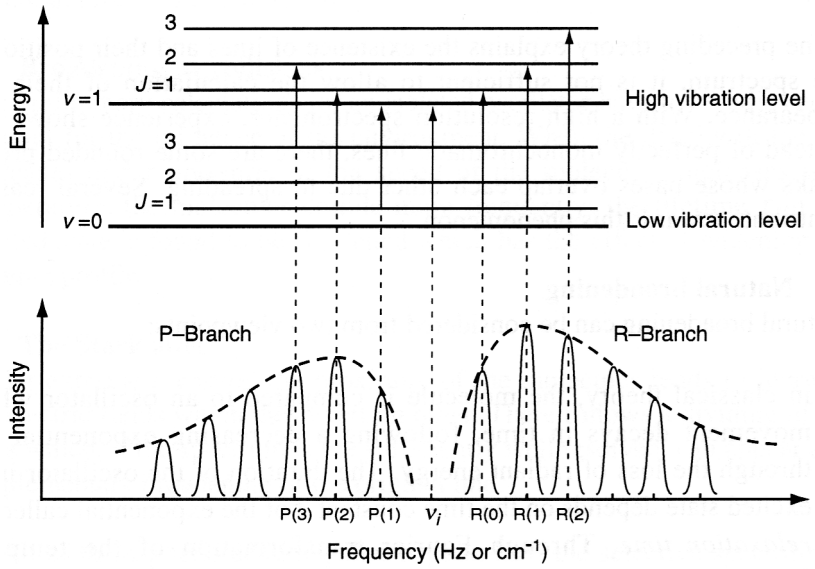

Figure 5.3: Resulting absorption spectrum as a result of the vibrational and rotational selection rules. Note also the width of the individual absorption lines due to Doppler and pressure broadening.

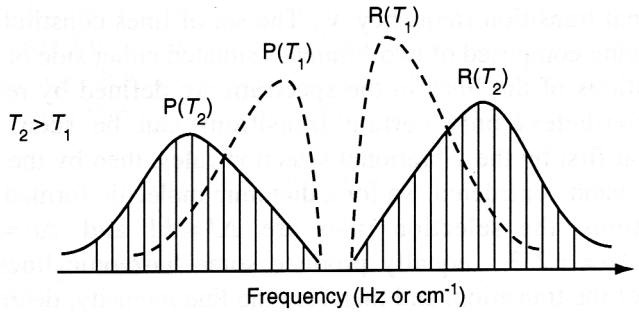

Figure 5.4: Resulting shift of the maxima of the branches due to an increase in temperature.

5.3 Geometrical optics

Whereas the dispersive element will dictate the resolution of the spectrometer (as will be discussed in chapter 6), the geometrical optics will dictate the throughput (i.e. etendue) of the system. The throughput defines how well the spectral lines can be determined and is given by [27]:

$$Z = \frac{\mathcal{T} A_e \cos\theta_f A_f \cos\theta_i}{f^2} = \mathcal{T} A_f \cos\theta_i \Omega = \mathcal{T} A_f \cos\theta_i \frac{\pi}{4F^2} = \mathcal{T} A_f \pi \mathrm{NA}^2 \tag{5.4}$$

where $\mathcal{T}$ is the transmittance of the spectrometer, A_e is the area of the entrance pupil, A_f is the area of the field stop, Ω is the projected solid angle, f is the focal length, F is the optical speed in terms of the F-number, and NA is the numerical aperture.

Since this has not been the main focus of this thesis, only very basic optical analysis has been

performed. Its only purpose is to give a rough idea on what can be expected from the complete system. Later studies may further refine the optical analysis and modeling. In this thesis, the throughput as a function of projected solid angle will be used. Later studies may of course also use one of the other definitions as given in equation (5.4).

5.3.1 (Projected) Solid Angle

The *solid angle*, ω, is an angle in a 3-Dimensional space. The unit of a solid angle is a steradian [sr]. A (full) sphere subtends 4π steradians. As illustrated in figure 5.5, an infinitesimal area $\mathrm{d}A$ at a distance r from the origin subtends an infinitesimal solid angle $\mathrm{d}\omega$ equal to the size of the projection of this small area $\mathrm{d}A$ on a unit sphere.

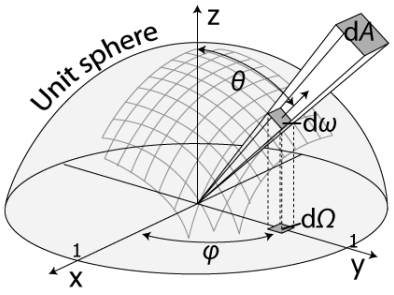

Figure 5.5: Differential solid angle, $\mathrm{d}\omega$ subtended by an element of area $\mathrm{d}A$ at a distance r from the point of observation **P** and the associated differential projected solid angle $\mathrm{d}\Omega$. [15]

The definition of a solid angle is given correctly only in its differential form:

$$\mathrm{d}\omega = \frac{\mathrm{d}A}{r^2} = \sin\theta \mathrm{d}\theta \mathrm{d}\phi \tag{5.5}$$

Integrating over the zenith angle, θ, and azimuthal angle, ϕ, we can write an expression for the solid angle subtense of a flat disc of planar half-angle θ_{max}:

$$\omega = \int_0^{2\pi} \int_0^{\theta_{max}} \sin\theta \mathrm{d}\theta \mathrm{d}\phi = 2\pi(1 - \cos\theta_{max}) \tag{5.6}$$

For sufficiently small numbers of θ_{max}, (5.6) may be approximated by:

$$\omega = \frac{A}{r^2} \tag{5.7}$$

The solid angle subtended by a square or rectangular area is much more complex and is considered outside the scope of this thesis.

The *projected solid angle*, Ω [sr], is visualized as shown in figure 5.5. In spherical coordinates it is given by:

$$\mathrm{d}\Omega = \cos\theta \mathrm{d}\omega = \sin\theta\cos\theta \mathrm{d}\theta \mathrm{d}\phi \tag{5.8}$$

The projected angle for a circular disc subtending the apex semi-anlge of θ_{max}, is obtained again by integrating equation (5.8) over the zenith and azimuthal angles:

$$\Omega = \int_0^{2\pi} \int_0^{\theta_{max}} \sin\theta\cos\theta \mathrm{d}\theta \mathrm{d}\phi = \pi(\sin^2\theta_{max}) \tag{5.9}$$

The numerical value of the projected solid angle is equal to the value of the solid angle with less than 5% error for the values of θ_{max} equal or less than 10°.

5.3.2 Incidence calculation

One proposal is to have both the source and detector on the same chip as a means of cost and size reduction. This would require a reflector at the far end. The most obvious option would be to have a concave ellipsoidal mirror. The main advantage of using an ellipsoidal mirror would be the equal length of all the light paths from one focal point to the other and thus an image free of spherical aberration when the image and object are located at each of their foci. As will be seen in section 5.4, the length of the light path is of direct influence to the absorption of light by the gas mixture. Having equal lengths for all optical paths therefore also makes for more simple modeling and post-processing of measured data.

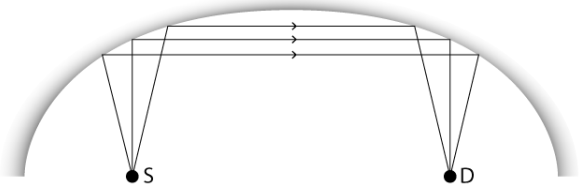

Figure 5.6: Shematic drawing of proposed setup. Source and detector are located on the same chip with a concave ellipsoidal mirror as reflector.

However, not all gases absorb as much. With clever design, one can increase the resolution of a certain gas by creating different light paths for different wavelengths. Carbon Monooxide for example absorbs much less compared to Carbon Dioxide. Having equal path lengths, the resolution of Carbon Monooxide is therefore limited by Carbon Dioxide. Unfortunately no time was left to pursue this path. We therefore continue this discussion with an elliptical mirror in mind.

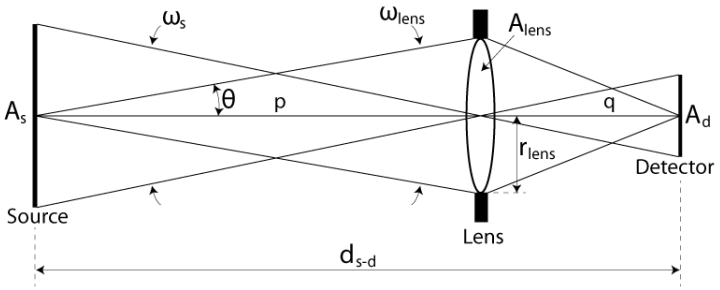

Figure 5.7: Incidence of a detector through a lens system. [28]

If we would assume a perfect lens and compare this to a perfect elliptical mirror, from a solid angle point of view, there is no difference. Looking at figure 5.7, we see that the optics are on axis, so the cosine is 1 reducing the throughput as described by equation 5.4 to:

$$Z = \mathcal{T} A_{lens} \omega_s = \mathcal{T} A_s \omega_{lens} = \mathcal{T} A_s 2\pi(1 - \cos\theta) \tag{5.10}$$

where the lens aperture, A_{lens}, acts as an intermediate receiver and the view angle, θ, is calculated using:

$$\theta = \tan^{-1}\left(\frac{r_{lens}}{p}\right) = \tan^{-1}\left(\frac{r_{lens}(M+1)}{Md_{s-d}}\right) \tag{5.11}$$

where r_{lens} is the radius of the lens in [m] and M is the magnification, determined by the maximum of the two length ratios (x and y direction):

$$M = \max\left(\frac{\text{length}_{d_x}}{\text{length}_{s_x}}, \frac{\text{length}_{d_y}}{\text{length}_{s_y}}\right) \tag{5.12}$$

The incidence on the detector, E_d, will be reformatted because of the lens, and will form an image of the original object, at the appropriate magnification. The incidence may therefore be calculated by:

$$E_d = LZ = L\mathcal{T}A_s 2\pi(1-\cos\theta) \tag{5.13}$$

If no lens is present in the system, equation (5.13) is still valid, but with:

$$\theta = \tan^{-1}\left(\frac{r_d}{d_{s-d}}\right) \tag{5.14}$$

where r_d is the radius of the detector.

5.4 Modeling

Now we have a better understanding of the physics behind infrared absorption by the gas molecules and how the optics influence the incidence on the detector, it is possible to create a model. The model will be broken up in two major components: Modeling of the absorption spectra of the different gases and the modeling of the throughput of the system.

5.4.1 Modeling of the absorption spectra

Based on empirical data, this part of the model will be able to calculate the absorption spectra of the different molecules with a fair amount of accuracy. Fully theoretical models have been developed as well, but are either extremely computational intensive or do not have a satisfactory accuracy. Using empirical data, there are two options. First, it is possible to use measured spectra of which parameters like pressure, optical path length and temperature are known, and adapt this measured spectrum to create the required or customized spectrum as will be explained further in section 5.4.1.2. Second, we can use line lists like HITRAN, in which parameters can be found that are extracted from very high resolution measurements, as further discussed in section 5.4.1.3. The main difference between these two options is that the latter option requires the spectrum to be build up from scratch. The two main advantages of this is first of all that all dependencies like pressure, temperature and so on, can all be taken into account directly and in a known fashion. Secondly, the spectral range is, within limits, completely self defined, whereas the first option will be limited by the range of the original measurement. The downside of using the database is that it will require a lot more computing power compared to the first one and is therefore a lot more time consuming.

5.4.1.1 Beer-Lambert law

The transmission of light through a medium can be expressed by the Beer-Lambert law as:

$$I = I_0 e^{-OD} \tag{5.15}$$

where I is the intensity of the light after passing through the medium, I_0 is the initial light intensity and OD is the Optical Depth given by $OD = \alpha(\lambda) \cdot l$, with $\alpha(\lambda)$ the absorption coefficient [μm] and l the optical path length [cm] (i.e. the total distance the light has to travel through the gas sample). This can be related to the more common parameter of transmittance, $\mathcal{T}$ as:

$$\mathcal{T}(\lambda) = \frac{I}{I_0} = e^{-OD(\lambda)} = e^{-\alpha(\lambda) \cdot l} \tag{5.16}$$

If we would assume the reflection to be 0, the absorption, A, would be given by $A = 1 - \mathcal{T}$. This should not be confused with the absorbance, $\mathcal{A}$, which is defined as:

$$\mathcal{A} = -\log_{10}(\mathcal{T}) = \frac{OD}{\ln(10)} = 0.434 \cdot OD \tag{5.17}$$

According to Dalton's law of partial pressures, we can state that the total pressure, P_{tot} [atm], exerted by a gaseous mixture of m gases, is equal to the sum of the partial pressures, P_i [atm], of each individual gas.

$$P_{tot} = \sum_{i=1}^{m} P_i \tag{5.18}$$

If each of the gases behaves independently of the others then we can apply the ideal gas law to each gas component of the sample:

$$P_i = 9.869 \cdot 10^{-6} \frac{n_i R T}{V} \tag{5.19}$$

where the coefficient in front is the conversion factor to [atm], n_i [mol] is the number of moles of gas i, $R = 8.314$ J mol^{-1} K^{-1} is the Molar gas constant, T [K] is the absolute temperature and V [m^3] is the volume in which the gas mixture is present.

Using equations (5.18) and (5.19), we can see that at constant temperature and volume, the total pressure of a gas sample is determined solely by the total number of moles of gas present, whether this represents a single substance or a mixture.

$$n_{tot} = \sum_{i=1}^{m} n_i \tag{5.20}$$

So, if the total and partial pressures of a gas mixture are known, we can determine the mole percentages and the other way around.

In a similar fashion it can be shown that the total attenuation or composite transmittance is related to the summation of the individual optical depths as:

$$OD_{tot} = l \cdot \sum_{i=1}^{m} \alpha_i(\lambda) \tag{5.21}$$

The absorption coefficient can be related to the molecular line intensity, S, by:

$$\alpha(\lambda) = S(\lambda) \cdot g(\lambda) \cdot N = k(\lambda) \cdot N \tag{5.22}$$

where $S(\lambda)$ [μm/(molecule/cm^2)] is the molecular line intensity, $g(\lambda)$ [μm^{-1}] is the normalized lineshape function, N [molecules m^{-3}] is Loschmidts' number and $k(\lambda)$ [cm^2 molecule^{-1}] is called the *cross section*. It is preferable to keep the units for wavenumber and area separated. Loschmidts' number is defined as:

$$N = \frac{N_A \cdot P_p}{R \cdot T} = \frac{P_p}{k_b \cdot T} = \frac{qP_{tot}}{k_b \cdot T} \tag{5.23}$$

where $N_A = 6.022 \cdot 10^{23}$ mol^{-1} is Avogadro's constant, P_p [atm] is the partial pressure of the gas, $k_b = 1.380$ J K^{-1} is the Boltzmann constant, q is the volume mixing ratio and P_{tot} [atm] is the total pressure. Using all of the above, the transmittance, $\mathcal{T}$, of monochromatic light is given by:

$$\mathcal{T}(\lambda) = e^{-S(\lambda)\cdot g(\lambda)\cdot N\cdot l} = e^{-k(\lambda)\cdot N\cdot l} \tag{5.24}$$

where $N \cdot l$ is also referred to as the *mass path*.

5.4.1.2 Method 1: Adaptation of measured spectra

If we now know the spectral transmittance data of a gas measured at a certain pressure and temperature, with a known optical path length, we can define the cross section as:

$$k_0(\lambda) = -\frac{\ln(T_0)}{N_0 \cdot l_0} = -\frac{R \cdot T_{k,0} \cdot \ln(T_0)}{N_A \cdot P_{p,0} \cdot l_0} \tag{5.25}$$

where the subscript, 0, refers to the values of the original measurement data. With this new variable, we can reconstruct the spectrum with the partial pressure and optical path length of our own setup by using:

$$\mathcal{T}(\lambda) = e^{-k_0(\lambda)\frac{N_A\cdot P_p}{R\cdot T} l} = e^{-k_0(\lambda)\frac{qP_{tot}}{k_b\cdot T} l} \tag{5.26}$$

The accuracy of this method is questionable, but it is fast and should give a fair indication of the absorption spectra.

5.4.1.3 Method 2: Using a line list for a line-by-line model

Line shapes

The bulk of the effort in line-by-line molecular spectra simulation, as for example done by [29,30], lies in computing the line shape, $g(\bar{\nu})$, for each individual absorption line. The dependency on wavenumber has been chosen consciously, as most line lists will be based on wavenumbers. Great care is required if one would like to transform the presented equations to wavelength based ones. More information on this topic is discussed in section 7.5.2.4

First, the position of the line is determined. The wavenumber of the line center, $\bar{\nu}_c$, increases linearly with pressure from its zero-pressure position, $\bar{\nu}_{c,0}$:

$$\bar{\nu}_c = \bar{\nu}_{c,0} + \delta_{air}\frac{P_{tot}}{P_0} \tag{5.27}$$

where P_0 is the pressure at reference state (1 atm). The parameters $\bar{\nu}_c^0$ and δ are found in an appropriate line list such as HITRAN [31]. In figure 5.3, we saw that the absorption of light due to a particular molecular transition is not confined to a single wavenumber, but is spread over a range of wavenumbers. This spreading of the absorption line arises from three mechanisms. First, every spectral line has a natural width arising from the Heisenberg uncertainty principle,

but this is almost always negligible compared to other broadening effects. Second, thermal motions impart a random Doppler velocity to each molecule, causing the ensemble absorption to be blurred over some range. Finally, random collisions perturb energy levels of individual molecules slightly differently, and the cumulative effect is known as pressure broadening.

At low pressures (less than 0.01 atm = 1013 Pa), Doppler broadening is most important. This results in a Gaussian line shape with Half Width Half Maximum (HWHM), γ_D, given by [32]:

$$\gamma_D = \bar{\nu}_c \sqrt{\frac{2k_b T}{mc_0^2}} \tag{5.28}$$

where m is the molecular mass.

At higher pressures (above 0.1 atm = $1.013{\cdot}10^4$ Pa), pressure broadening dominates, and produces a Lorentz line shape. The amount of broadening depends somewhat on the type of molecules involved in the collisions. Collisions between molecules alike, can produce a noticeable different broadening than collisions between different species. The Lorentz HWHM, γ_L, is therefore computed as the weighted sum of air- and self-broadened HWHMs, γ_{air} and γ_{self}, adjusted for pressure and temperature:

$$\gamma_L = [(1-q)\gamma_{air} + q\gamma_{self}] \left(\frac{P_{tot}}{P_0}\right) \left(\frac{T_0}{T}\right)^{n_{air}} \tag{5.29}$$

where T_0 is the temperature at reference state (296 K). Note also that we have made the common assumption that the same temperature exponent, n_{air}, applies to both air- and self-broadening. Once again, the parameters γ_{air}, γ_{self} and n_{air} are obtained from a line list such as HITRAN. The combination of Doppler and Lorentz broadening yields the more general Voigt profile [32]:

$$f(\bar{\nu}) = \frac{1}{\sqrt{\pi}\gamma_D} \frac{1}{\pi} \frac{\gamma_L}{\gamma_D} \int_{-\infty}^{\infty} \frac{e^{-t^2}}{[(\bar{\nu}-\bar{\nu}_c)/\gamma_D - t]^2 + (\gamma_L/\gamma_D)^2} \mathrm{d}t \tag{5.30}$$

The final line shape equation is formed when the far-wing effects are corrected [32]:

$$g(\bar{\nu}) = \frac{\bar{\nu}}{\bar{\nu}_c} \frac{\tanh(hc_0\bar{\nu}/2kT)}{\tanh(hc_0\bar{\nu}_c/2kT)} f(\bar{\nu}) \tag{5.31}$$

According to Whiting [33] this can be rewritten in a first approximation by:

$$\frac{g(\bar{\nu})}{I_{g,max}} = \left(1 - \frac{\gamma_L}{\gamma_V}\right) e^{-2.772\left(\frac{\bar{\nu}-\bar{\nu}_c}{2\gamma_V}\right)^2} + \left(\frac{\gamma_L}{\gamma_V}\right) \frac{1}{1 + 4(\bar{\nu} - \bar{\nu}_c/(2\gamma_V))^2} \tag{5.32}$$

Note that when $\gamma_L/\gamma_V = 0$, equation (5.32) redurces to the Gaussian profile and when $\gamma_L/\gamma_V = 1$ it reduces to the Lorentzian profile. Hence, this approximate expression is exact at those limits. It is also exact when $(\bar{\nu}-\bar{\nu}_c)/(2\gamma_V) = 0$ and 1/2. Generally, the accuracy of this approximation is reasonable except in the far wings of the line profile near the Gaussian limit. A large percentage error is presented in this region, but the absolute error is quite small. If we would require a more accurate approximation in the far wings, a second approximation can be stated:

$$\begin{aligned}\frac{g(\bar{\nu})}{I_{g,max}} = &\left(1 - \frac{\gamma_L}{\gamma_V}\right) e^{-2.772\left(\frac{\bar{\nu}-\bar{\nu}_c}{2\gamma_V}\right)^2} + \left(\frac{\gamma_L}{\gamma_V}\right) \frac{1}{1 + 4(\bar{\nu} - \bar{\nu}_c/(2\gamma_V))^2} \\ &+ 0.016 \left(1 - \frac{\gamma_L}{\gamma_V}\right) \left(\frac{\gamma_L}{\gamma_V}\right) \left[e^{-0.4\left(\frac{\bar{\nu}-\bar{\nu}_c}{2\gamma_V}\right)^{2.25}} - \frac{10}{10 + (\bar{\nu} - \bar{\nu}_c/(2\gamma_V))^{2.25}}\right]\end{aligned} \tag{5.33}$$

which is accurate to within 1 to 2% [34]. In equations (5.32) and (5.33), γ_V and $I_{g,max}$ are given by:

$$\gamma_V = \frac{1}{2}\left(\gamma_L + \sqrt{\gamma_L^2 + 4\gamma_D^2}\right) \tag{5.34}$$

and

$$I_{g,max} = \frac{1}{2\gamma_V}\left(1.065 + 0.447\left(\frac{\gamma_L}{\gamma_V}\right) + 0.058\left(\frac{\gamma_L}{\gamma_V}\right)^2\right) \tag{5.35}$$

Line intensity

We now turn our attention to the last remaining term needed for calculating the transmittance given by equation (5.24): the line intensity $S(\bar{\nu})$. HITRAN and other line lists provide S_0, the line intensity at $T_0 = 296$ K, as shown in figure 5.1. To calculate the line intensity in an arbitrary temperature, T, we adjust S_0 by the Boltzmann factors, account for stimulated emission effects and include the total internal partition function, $Q(T)$ as given in a separate table of the HITRAN database [35]:

$$S(T,P) = S_0 \frac{Q(T_0)}{Q(T)} \frac{e^{-hc_0E''/kT}}{e^{-hc_0E''/kT_0}} \frac{1 - e^{-hc_0\bar{\nu}_c/kT}}{1 - e^{-hc_0\bar{\nu}_c/kT_0}} \tag{5.36}$$

where E'' is the lower state energy of the transition (also provided by the HITRAN line list).

5.4.1.4 Implemented model

Cell title: TRANSMITTANCE CALCULATIONS
Sub-function(s): Gas_Transmission_jdx_v3

Due to time limitations, the model as presented here uses the method as described in section 5.4.1.2, where the absorption spectrum is calculated by means of the evaluation of measured data. The original files were retrieved from the NIST Chemistry WebBook [36].

To be able to view the results for several different gas mixtures and retrieve sensitivity plots, the user is able to give a range of concentrations for one or several gases. The model will calculate all possible mixtures with these ranges by checking if the combined concentration $\leq 100\%$. If no mixture fulfills this requirement, an error will be given. Further calculations will be performed on all unique mixtures.

5.4.2 Modeling of the throughput

Cell title: GEOMETRICAL OPTICS
Sub-function(s): User defined

This part of the model will calculate the throughput of the system. As said before, only very basic analysis has been done so far, but the model allows for easy adaption to a more intricate and complete model. This has been accomplished by allowing the user to create his/her own sub-function which calculates the throughput (i.e. etendue) of the system. For this thesis two such sub-functions have been made. One which describes a system where the detector is lit directly by the source (called "*Throughput_Direct.m*") and one where there is intermediate optics like a lens or elliptical mirror (called "*Throughput_Focused.m*").

Both functions are based on equations (5.6) and (5.4). At this stage, only the transmission of the optics is incorporated. As shown before, the transmission of the gas is calculated separately.

This will allow for a better insight into the influence of the optics and the gas on the system performance.

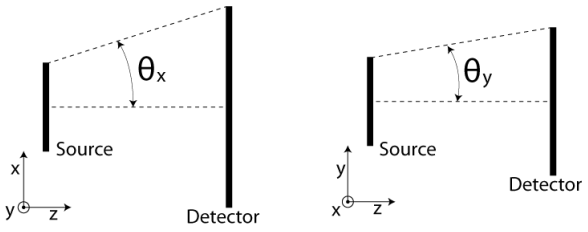

Figure 5.8: Definition of the view angles, θ_x and θ_y.

"Throughput_Direct.m" directly implements equations (5.6) and (5.14) to the light transmitted from the source to the dispersive element on top of the detector. θ is determined by the maximum of θ_x and θ_y as shown in figure 5.8. It is also checked if the Lambertian assumption is valid by checking if $\theta < 20°$.

"Throughput_Focused" calculates the throughput using equations (5.10) and (5.11).

5.5 Optical path length design

As should be clear by now, the length of the path which is traveled by the light is one of the main parameters that determines the final dynamic range and accuracy. Since the absorption is related to the total amount of gas the light traveled through, a long path will have a high accuracy, because a small amount of added gas will still have a significant influence on the resulting signal. On the other hand, it means that for a certain amount of gas, the light will be absorbed completely, saturating the system (i.e. any amount of gas further added, has little to no influence on the signal).

Let us remember the required dynamic ranges as stated in section 3.2:

- CH_4: 0-100%
- C_2H_6: 0-14%
- CO_2: 0-40%
- CO: 0-40%

If we simulate the sensitivity of the system to several of the key gases for an arbitrary, but comparable set of parameters, we will get something as presented in figure 5.9. It clearly shows that the system is most sensitive to CO_2. Compared to pure CH_4 gas, CO_2 will already absorb a comparable amount of light at a concentration of only 20%. CO and CH_4 have a similar amount of absorption. These results are perfectly in line with what we would expect if we would look back at the line intensities in figure 5.1.

Since the system is most sensitive to CO_2, it will be the first to saturate and thus dictates the path length design. Unfortunately the optical path length is not the only parameter influencing the dynamic range and resolution. Other parameters that play a very significant role are the pixel size, read-out electronics and post processing algorithm as can be seen in figure 5.10.

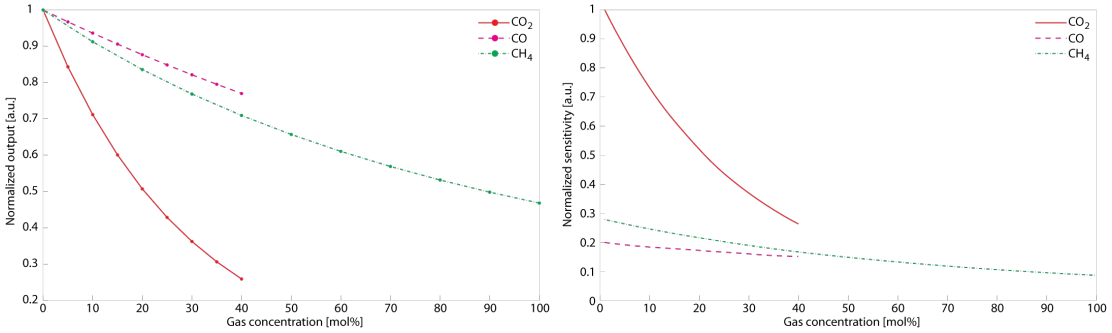

(a) (b)

Figure 5.9: a) Normalized output and b) Normalized sensitivity of the system to several of the key gases for an optical path length of 25mm, a pixel width of 200μmand a narrow set of pixels used for read-out.

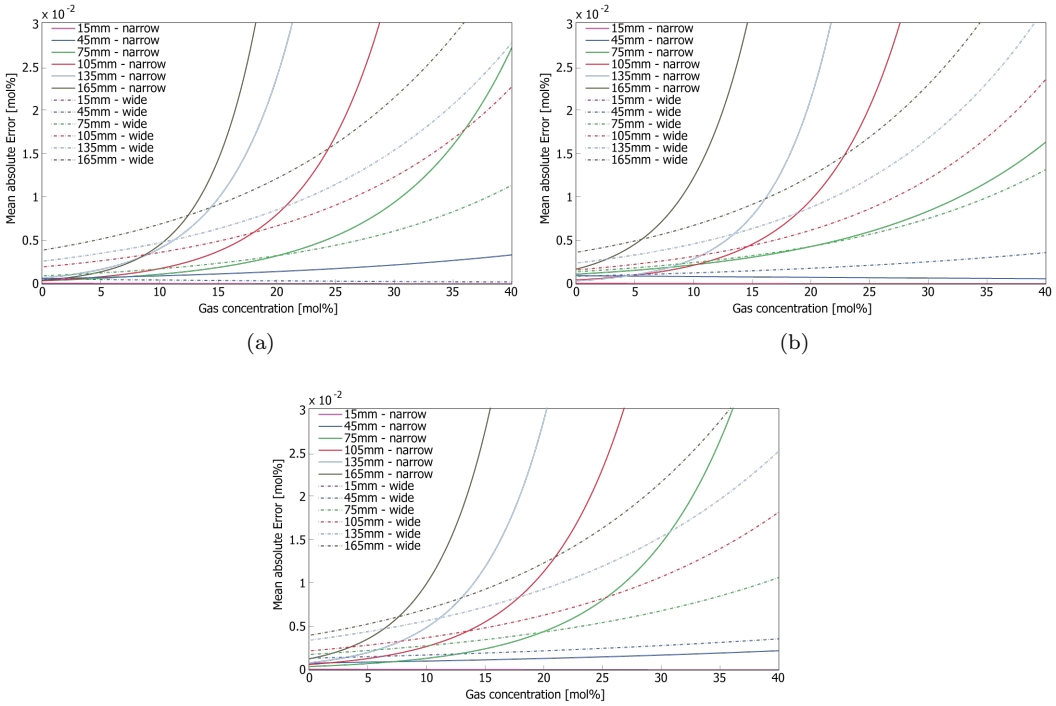

(a) (b)

(c)

Figure 5.10: Trend lines of the mean absolute error as function of CO_2 concentration for several optical path lengths and a pixel width of a) 200μm, b) 150μm and c) 100μm. 'Narrow' refers to a small set of pixels used to determine the final value, whereas 'wide' refers to a large set, including pixels that are less sensitive.

If we would only use the most sensitive pixels to determine the gas concentration, saturation kicks in quickly and the error shoots up almost vertically. Including less sensitive pixels will reduce this effect significantly since the mean value of the pixels is used.

The final optical path length is thus very much dependent on many other parameters and can not be determined independently. However, if we would assume, for example, a pixel size of 200μm and a narrow set of pixels for the read-out algorithm, we can use the model to predict the optimum path length for the different gas concentrations as shown in figure 5.11.

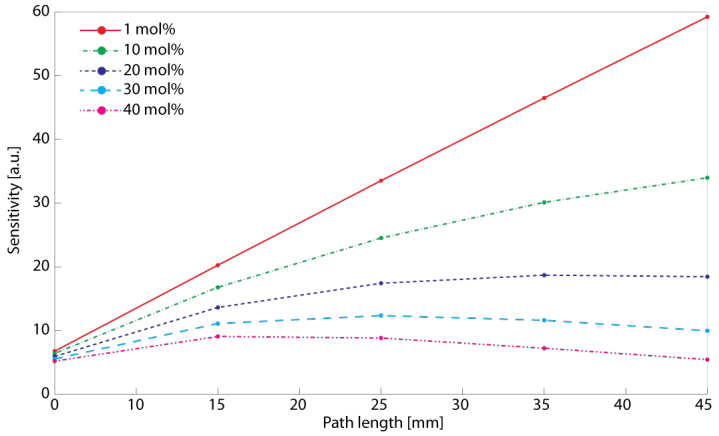

Figure 5.11: Simulated sensitivity of the system versus the length of the optical path for several concentrations of CO_2. It is assumed that the pixel width is 200μm and that a narrow set of pixels is used for read-out.

Obviously there is a maximum volume that the system may occupy. Getting the longest optical path length in a given volume has always been one of the key aspects of spectrometry. Typical designs include the White cell [37] and Herriott cell [38].

Unfortunately it is impossible at this stage to state any conclusive remarks on what the best optical path length would be. Measurements may give more insight.

Chapter 6

Dispersion, Filters & Spectrometers

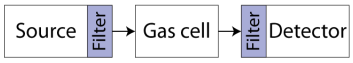

6.1 Introduction

Since we will use an infrared source with a broadband spectrum (as discussed in section 4.5, there will have to be at least one piece of optics that can 'disperse' the spectrum into its components, such that we can look at the specific parts of the spectrum where absorption may occur. The word 'disperse' in this particular case is used to describe the transition of the broad spectrum infrared light into a spatially distributed form (i.e. where the wavelength depends on the position). Typical examples of such a device would be a prism or grating, but also an array of several narrow band filters can be considered an option, since there is no particular need for a 'continuous' spatial distribution. The latter is also considered to include detectors that are inherently sensitive to only a small band, but these will be discussed in more detail in chapter 7.

The first sections of this chapter will discuss the different dispersing elements. For proper comparison, we will use the resolving power and free spectral range as figures of merit as explained in sections 2.4.2 and 2.4.3, respectively. Because the type of dispersing element is what defines the type of spectrometer, also discussions on the state-of-the-art spectrometers are included in these sections.

Only micro-spectrometers will be reviewed, since it would not make sense to try and make a comparison to their macro counterparts. It is already because of size only, that when purely looking at performance, micro-spectrometers will never win. On the other side the macro spectrometers are bulky, require complex lens systems and fine mechanics, making them very expensive [39–41]. So it all depends on application. In this particular case small size, low cost and wide dynamic range (see section 3.2) are of premium importance, making micro-spectrometers the most suitable.

The obvious characteristic performance parameters of spectrometers include resolution/accuracy, spectral range, sample time, multiplex advantage, cost, size and weight. Since most spectrometers are designed with an application in mind, it becomes very difficult to directly compare the different concepts and configurations according to these system parameters. Therefore, these discussions can be seen best as a description of what has been done so far. By discussing the strengths of these designs and where they are either flawed or just build for a slightly different

purpose, it should start to become clear which concept to further pursue and which research opportunities are to be identified as interesting and useful, conclusions of which are found in section 6.5

In section 6.6 we continue with a discussion on infrared filters. As most theory will already be discussed in the former sections, this discussion will be brief. Moreover, this part is not considered a main focus of this thesis.

Thereafter, the computer models for the dispersing element and the filters are presented. In the subsequent section, the detailed design is performed by using these models to do simulations. The fabrication of this design is then discussed, followed by the experimental results and the final conclusions.

6.2 Refraction

When light travels from one medium into another, the difference between the speed of light in these media causes the light to refract as shown in figure 6.1. It is the same effect that causes a rainbow by sunlight traveling through water droplets.

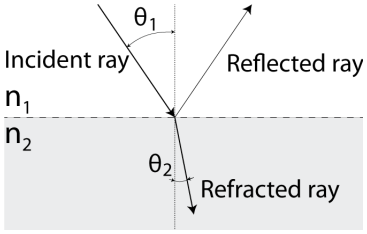

Figure 6.1: Light refraction and reflection at an interface.

The angle of refraction is given by Snell's equation:

$$\sin\theta_2 = \frac{n_1 \sin\theta_1}{n_2} \tag{6.1}$$

Where n_x is the *refractive index* of medium x given by $n = c_0/c_x$, with c_0 being the speed of light in vacuum and c_x the speed of light in medium x.

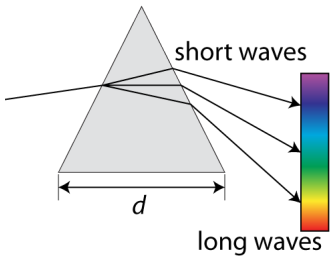

Figure 6.2: Path of a single ray in a prism

If the speed of light in the medium would be wavelength dependent, the refraction angle would also be wavelength dependent. This principle is used by a prism to spatially disperse the light

into its spectral components, as illustrated in figure 6.2. A prism shows a non-linear relationship between wavelength and refraction angle. If we assume an optimally used prism, theoretical or intrinsic resolving power is defined as [42]:

$$RP = d\frac{\mathrm{d}n}{\mathrm{d}\lambda} \tag{6.2}$$

Where d is the base width of the prism and $\mathrm{d}n/\mathrm{d}\lambda$ is a material property. As can be seen, for a high resolving power, the material of a prism should have the biggest variation in refractive index for the smallest variation in wavelength, while being very transparent in the relevant spectral region. These two properties however are not independent, limiting the intrinsic resolving power [42, 43]. It is therefore not often used in state-of-the-art equipment and will not be further discussed.

6.3 Interference

Apart from refraction we can also use interference to disperse the light. Interference is the addition (i.e. superposition) of two or more waves to result in a new wave pattern as shown in figure 6.3. This effect can for example be seen in oil films on water or soap bubbles.

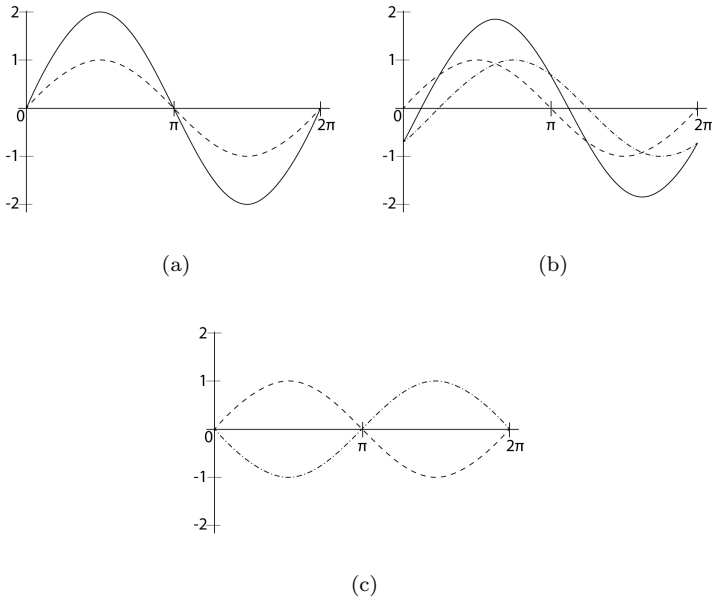

Figure 6.3: Interference of two waves (dashed lines) leading to (a) perfect constructive interference; (b) arbitrary interference; (c) perfect destructive interference.

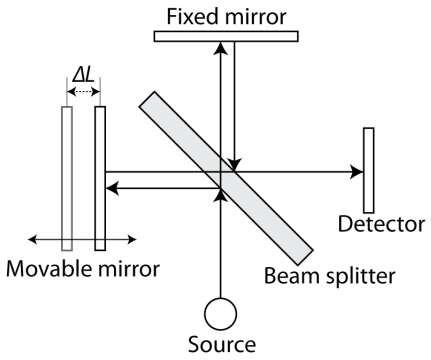

Figure 6.4: Michelson interferometer based spectrometer

6.3.1 Dual beam interferometers

6.3.1.1 Introduction

A dual beam interferometer uses two different light paths which are later combined again to let the two waves interfere. The resulting wave is then detected. The most common type of dual beam interferometer is the Michelson interferometer as illustrated in figure 6.4. Although there are other setups, the basic behavior is similar. Therefore only the Michelson interferometer will be reviewed here.

In the Michelson interferometer, an incident wavefront strikes an angled semi-transparent mirror (i.e. beam splitter), which partly reflects and partly transmits the beam. These waves continue to their respective mirrors, which will reflect them back to the beam splitter. A common implementation of the Michelson interferometer has one movable mirror mounted on a slider so that the length of that particular light path can be varied. The difference in optical path length between the two arms of the interferometer is known as the retardation, ΔL. An interferogram, $I(\Delta L)$, is obtained by varying ΔL while recording the detector's signal. For light with a spectral distribution of S(λ) the intensity as a function of the path length can be written as:

$$I(\Delta L) = \left(1 + \cos\left(\frac{2\pi\Delta L}{\lambda}\right)\right) \int_0^\infty S(\lambda) d\lambda$$

or: (6.3)

$$I(\Delta L, \lambda) = \int_0^\infty S(\lambda) \cos\left(\frac{2\pi\Delta L}{\lambda}\right) d\lambda$$

The original input spectrum can then be obtained again by calculating the inverse cosine Fourier transform of the measured interferogram:

$$S(\lambda) = \frac{1}{2\pi} \int_{-\infty}^{\infty} I(\Delta L) \cos\left(\frac{2\pi\Delta L}{\lambda}\right) d(\Delta L) \tag{6.4}$$

Basically, this type of interferometer, converts the power spectrum of an optical input signal into spatial information (i.e. fringe patterns) by a Fourier transform. The minimum resolvable

power is therefore limited by the number of samples taken for the FFT operation and the Nyquist criterion. [18]

6.3.1.2 State-of-the-art

A very well established device using the dual beam interference principle is the Fourier Transform Infrared (FTIR) spectrometer. As is clear from equation (6.4), the accuracy of such a system is directly related tot the ability to accurately measure ΔL. For this purpose, most Fourier spectrometers use a stable monochromatic reference light source like a HeNe laser, which follows the same light path.

MEMFIS is a project currently busy with miniaturization of FTIR spectrometers. Their motivation: "To promote a widespread use of these analysers and sensors, a small, robust and easy to use FT-spectrometer, that could be built inexpensively, is needed." [44]. The aim is to get the spectral resolution down to 5 cm^{-1}, while keeping fast measuring times and the size down to about the size of a smaller cigar box. One paper by Kraft published as part of this project [45] describes, among other things, the work on the translational MEMS mirror (more detailed descriptions of which can be found in [46] and [47]) and how this mirror fits in the complete system. It is clear that the system has great potential, but is still very complex due to the required drive electronics for the movable mirror and the cooler for the HgCdTe detector.

Advantages of FTIR systems include:

- High resolution
- Wide spectral range
- Only one detector required for the full spectrum
- High scanning speed

Disadvantages of FTIR systems include:

- Complex optics (e.g. Moving mirror, Beam splitter)
- Reference beam required
- Difficult to miniaturize
- Zero measurement required
- Relatively complex calculations

6.3.2 Fabry-Pérot interferometers

6.3.2.1 Introduction

A Fabry-Pérot interferometer (i.e. etalon) is (as illustrated in figure 6.5) a stack of two highly reflecting mirrors with a resonator cavity in between. By having the light reflect multiple times between the reflecting surfaces, an interference pattern is created. Constructive interference occurs if the transmitted beams are in phase, corresponding to a high-transmission peak. The transmission minima result from destructive interference of out-of-phase beams. Whether the reflected beams are in-phase or not depends on the wavelength (λ) of the light, the angle of

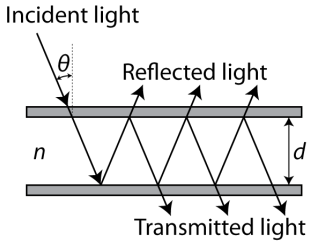

Figure 6.5: Fabry-Pérot interferometer.

incidence of the light on the etalon (θ), the thickness of the cavity (d), the reflectivity of the mirrors (R) and the refractive index of the resonator cavity material (n_r) at wavelength λ. These will create a transmittance spectrum given by [18] (also known as the Airy function):

$$T = \frac{I}{I_0} = \frac{1}{1 + F\sin^2(\frac{\delta}{2})} \tag{6.5a}$$

$$\text{With: } F = \frac{4R}{(1-R)^2} \tag{6.5b}$$

$$\text{and: } \delta = \left(\frac{4\pi n_r}{\lambda}\right) d\cos\theta \tag{6.5c}$$

Where F is called the coefficient of finesse, which is an optical parameter of the mirrors.

As can be seen from equation (6.5a), the function will be periodic for $\delta = m \cdot 2\pi$, with $m = 0, \pm1, \pm2, etc.$ Therefore the center wavelength of the peak of order m is given by:

$$\lambda_m = \frac{2n_r d\cos\theta}{m} \tag{6.6}$$

We can now calculate the free spectral range as defined in section 2.4.3 as:

$$\text{FSR} = \lambda_m - \lambda_{m+1} = \frac{\lambda_{m+1}}{m} = \frac{\lambda_m}{m+1} \tag{6.7}$$

Similarly, we can look at it from the phase point of view:

$$\begin{aligned} \Delta\delta = \delta_1 - \delta_2 &= \frac{4\pi n_r d\cos\theta}{\lambda_1} - \frac{4\pi n_r d\cos\theta}{\lambda_2} = 2\pi \\ \rightarrow \frac{2n_r d\cos\theta}{\lambda_1} &= \frac{\lambda_2 + 2n_r d\cos\theta}{\lambda_2} \\ \rightarrow \frac{\lambda_2 - \lambda_1}{\lambda_2\lambda_1} &= \frac{1}{2n_r d\cos\theta} \end{aligned} \tag{6.8}$$

Which means that the FSR of a Fabry-Pérot interferometer is also given by:

$$\text{FSR} = \lambda_2 - \lambda_1 = \frac{\lambda_2\lambda_1}{2n_r d\cos\theta} = \frac{\lambda_2^2}{\lambda_2 + 2n_r d\cos\theta} \tag{6.9}$$

Clearly showing that the FSR is dependent on the wavelength and the distance between the two mirrors. In practice, the FSR is limited by the stopband of the reflector as will be discussed in section 6.3.2.2.

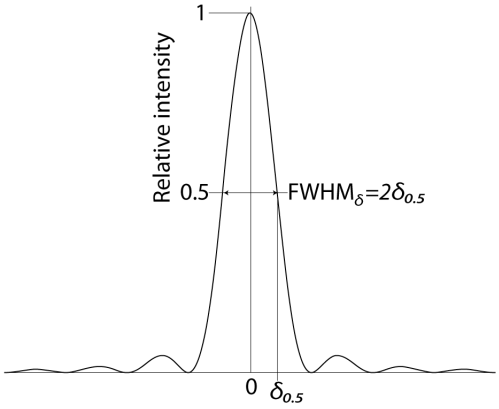

Figure 6.6: Phase plot

Probably the most important figure to define the performance of a Fabry-Pérot type filter in a spectral measurement setup, is called the *finesse*, f. The finesse can most easily be seen as the amount of resolvable peaks that fit within the free spectral range. Using the FWHM criterion, as illustrated in figure 2.7(b), for resolvability, we can write:

$$f = \frac{\text{FSR}}{\text{FWHM}} \tag{6.10}$$

Again, we can also look at it from the phase point of view and define the finesse as the amount of resolvable peaks that fit within one period of 2π. Again using the FWHM criterion for resolvability ($T = 0.5$) and equation (6.5a), the width of the peak (as illustrated in figure 6.6) is defined as:

$$\text{FWHM}_\delta = 2\delta_{0.5} = 4\sin^{-1}\left(\frac{1}{\sqrt{F}}\right) \tag{6.11a}$$

Which, for the common case of a rather large F, reduces to:

$$\text{FWHM}_\delta = \frac{4}{\sqrt{F}} \tag{6.11b}$$

From this point of view, we can now define the finesse as caused by the reflective properties of the mirrors as:

$$f_R = \frac{2\pi}{\text{FWHM}_\delta} = \frac{\pi}{2\sin^{-1}\left(\frac{1}{\sqrt{F}}\right)} \approx \frac{\pi\sqrt{R}}{1-R} = \frac{\pi}{2}\sqrt{F} \tag{6.12}$$

Assuming the mirrors to be perfectly parallel, we could state $f = f_R$. If this assumption cannot be made, we have to include a term to describe the deviation from parallelism. According to [48, 49] this term can be described by:

$$f_p = \frac{\lambda}{\sqrt{3\delta_p^2}} \tag{6.13}$$

where δ_p is the plate deviation from parallel. These terms can than be used to describe the finesse as:

$$f = \frac{1}{\sqrt{\frac{1}{f_R^2} + \frac{1}{f_p^2}}} \tag{6.14}$$

In contrary to the coefficient of finesse as defined in equation (6.5b), finesse is a structural quality factor of the filter and increases dramatically with increasing reflectivity. It shows how many spectral channels can be defined in its operating bandwidth and thus is a measure of spectral selectivity. To achieve high finesse, mirror reflectivity needs to be extremely high (e.g. above 0.997 for a finesse of above 1000).

Using the same basic steps we can also derive the resolving power for a Fabry-Pérot interferometer. The FWHM criterion gives us $\text{FWHM}_\delta = \Delta\delta$. Using the earlier stated periodicity of $\delta = m \cdot 2\pi$ and equation (6.11) we can write:

$$RP = \frac{\delta}{\Delta\delta} = \frac{\delta}{\text{FWHM}_\delta} = \frac{m\pi}{2\sin^{-1}\left(\frac{1}{\sqrt{F}}\right)} = mf_R \tag{6.15}$$

Another design parameter we can define, is the *contrast*, C. This is the ratio of the maximum and minimum transmittance [50]:

$$C = \frac{T_{max}}{T_{min}} = \frac{(1+R)^2}{(1-R)^2} \tag{6.16}$$

Linear Variable Optical Filter (LVOF)

A special case of the Fabry-Pérot filter is a so called Linear Variable Optical Filter (LVOF). An LVOF can best be described as a long Fabry-Pérot etalon where the resonator cavity is tapered along its length (see figure 6.7). This will cause a difference in the central wavelength of the bandpass filter along the length of the LVOF, creating a dispersed spectrum.

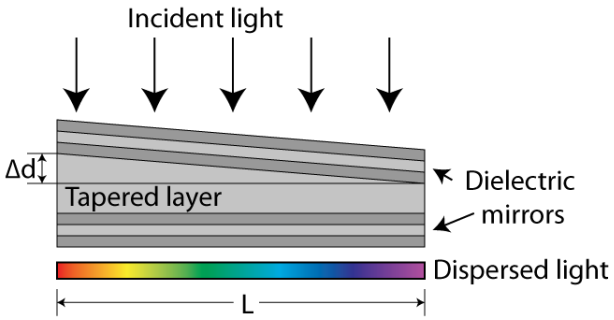

Figure 6.7: Basic setup of a Linear Variable Optical Filter with Bragg reflectors.

Due to the fact that the Full-Width Half Maximum (FWHM) of the LVOF is not practically zero, a collimated, monochromatic light within the free spectral range will illuminate a region underneath the LVOF given by [51]:

$$\Delta x = \frac{\text{FWHM}}{\theta} \tag{6.17}$$

Where $\theta = \Delta d/L$ [rad] denotes the slope of the tapered cavity layer.

6.3.2.2 Reflectors

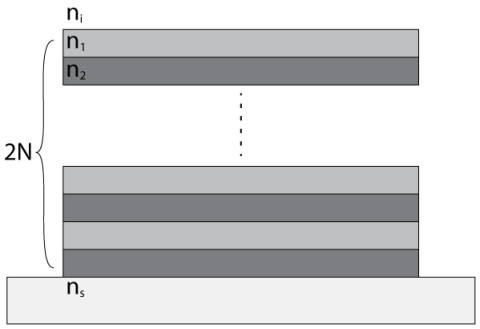

Figure 6.8: The structure of a Bragg reflector.

As became clear in the previous section, the performance of a Fabry-Pérot interferometer is highly dependent on the reflectance of its reflectors. To achieve a high reflectance, several reflector implementations are possible. One such implementation is of the Bragg type as shown in figure 6.8. A Bragg reflector is the basic type of multi-layered dielectric mirrors. The structure in its simplest form consists of N pairs of high-n/low-n layers of quarter wavelength optical thickness (QWOT), also described as $(\mathbf{HL})^{\mathbf{N}}$. Adding one more high-n layer at the substrate, will increase the reflectivity, giving a complete structure described by Medium/$(\mathbf{HL})^{\mathbf{N}}\mathbf{H}$/Substrate. One QWOT means that the optical thickness $(n \cdot d)$ is one quarter of the reference wavelength, λ_0, typically chosen in the center of the wavelength range of interest. Thus, QWOT $= \frac{\lambda_0}{4n}$, where n is the refractive index of the dielectric material at the reference wavelength. The reflectivity, R, and stopband of the mirror can then be expressed analytically by [51]:

$$R = \frac{n_i n_2^{2N} - n_1 n_s^{2N}}{n_i n_2^{2N} + n_1 n_s^{2N}} \tag{6.18}$$

$$\frac{\Delta\lambda}{\lambda_0} = \frac{4}{\pi} \sin^{-1}\left(\frac{n_2 - n_1}{n_2 + n_1}\right) \tag{6.19}$$

The maximum FSR from a Bragg reflector is half of its maximum bandwidth [51]:

$$FSR_{max} = \lambda_0 \frac{2}{\pi} \sin^{-1}\left(\frac{n_2 - n_1}{n_2 + n_1}\right) \tag{6.20}$$

Where N is the amount of layers of a single dielectric, and n_i, n_1, n_2 and n_s are the refractive indices of the incident medium, the first dielectric, the second dielectric and the substrate, respectively. It reveals the benefit of using materials with a refractive index as far apart from the other as possible. Higher difference between the refractive index of the two dielectric layers results in a larger stopband region of the mirror, reducing the amount of layers required to achieve a specific level of reflectance. The influence of the order of the Bragg reflector on its transmission is shown in figure 6.9, which clearly shows an increased reflectance in the stopband region, $\Delta\lambda$, for increased order.

When a wider stopband is required or when the rippels are considered too big, two or more edge filters can be used. An edge filter is similar to a Bragg reflector, but has either two **0.5H** layers instead of **H** as the first and last layer of the stack (i.e. $\mathbf{0.5H}(\mathbf{LH})^{\mathbf{N-1}}\mathbf{L0.5H}$, also written

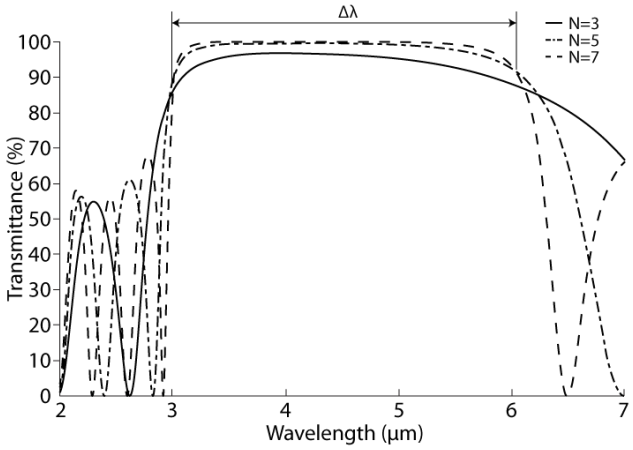

Figure 6.9: Transmission plots for different orders of bragg reflectors.

as $\mathbf{0.5HL0.5H})^{\mathbf{N}}$) to remove the ripples on the long wavelength region after the stopband, or two **0.5L** layers (i.e. $(\mathbf{0.5LH0.5L})^{\mathbf{N}}$) to remove the ripples on the short wavelength region after the stopband.

Design of a Bragg reflector based Fabry-Pérot structure, has some important design issues. As said before, to achieve a high finesse requires a high reflectance. Using eq. (6.18), gives an N of 8 in order to achieve a reflectivity of $R > 0.997$. This results in 16 dielectric layers for each reflective mirror and a total of 33 layers for the complete Fabry-Pérot structure (including the resonance chamber), which is considered to be quite a lot. Also, the maximum FSR which can be expected from any Fabry-Pérot structure is only half of the maximum bandwidth of its Bragg reflector as presented in equation (6.19). As can be seen in equation (6.9), the FSR is also dependent on the cavity thickness, d. Increasing the thickness (e.g. from λ to 2λ), will decrease the FSR, implying that the FSR decreases with increasing order. However, such higher order Fabry-Pérot, also creates a smaller FWHM. Therefore, a design trade-off between selectivity and FSR results.

It is also possible to use metallic reflectors. The advantage would be the increase of free spectral range, but it comes at quite a hefty price. For one, the reflectivity is not that high, reducing the finesse. An even worse property is the relatively high absorption of the metals, decreasing the throughput (i.e. amount of light transmitted) to only 15-30%.

6.3.2.3 State-of-the-art

Spectrometers in which Fabry-Pérot filters are used as dispersing elements are called Non-Dispersive Infrared (NDIR) spectrometers. In the world of micro-spectrometry, the NDIR micro-spectrometer is often considered as the best choice. Main reason for this includes the simplicity of the system, which in turn makes for a simpler and cheaper production. Although the basic setup is the same for all NDIR spectrometers, it is definitely possible to identify different concepts on how to best use this setup.

A dedicated natural gas composition detector utilizing, among others, the NDIR principle, is the Gas-Lab Q1 [52, 53]. Although designed for the detection of the composition of natural gas, its dynamic range is still a bit limited and it requires a high purity methane gas for automatic calibration. A 10 Liter bottle should last about a year. Moreover, the whole unit cannot really

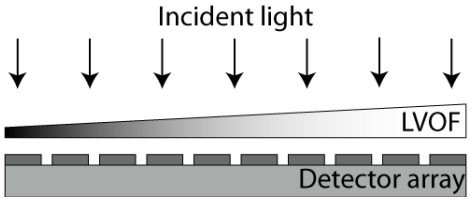

Figure 6.10: Example of a non-dispersive infrared micro-spectrometer by using a Linear Variable Optical Filter (LVOF).

be considered compact, making it a good proof of concept for the main project, but also leaving a lot of work to be done. Unfortunately not much is known about the NDIR part of the system except that it measures CO_2 and CH_4 with two separate sensors.

The most traditional and common found NDIR setup is that of an array of detectors where each detector or set of detectors has its own specific filter in front. This setup was first described in a series of publications by López *et al.* [54–57]. Although it wouldn't be considered a micro-spectrometer anymore these days, it was the first step in that direction and shows some interesting design features. As said, the most interesting feature is the exchange of the filter wheel by a set of filters on top of 20 thermo-electrically cooled PbSe detectors. Another interesting design feature is the use of three mirrors in a so called white-cell configuration [37] and the spectrally-selective coating on these mirrors to block any light outside the region of interest. The white-cell is designed such that the light beam reflects 24 times before it is directed to the detector. Except that this increases the path length of the light and therefore its resolution, the coatings on the mirrors also only have to be about one third of the thickness for a single pass filter, greatly reducing their cost and production complexity. The resolution, although not mentioned with great detail is thought to be in the order of tens of ppm of gas. It is also mentioned that the use of pyroelectric detectors might be a better option, but no further reports are found on this topic. The dynamic range of this system is not mentioned, but is expected to be small due to the long optical path of 600 cm. With the gas cell alone being 25 cm long, it is, as already implied, still considered too big.

A more modern approach to this same concept is described by Tan [58]. Here each gas to be detected has its own pyroelectric detector with a thin-film filter in front, plus one detector with filter to act as a reference channel. By referencing the output signal of the gas detection channels to the reference channel, changes in source power or environment should be canceled quite well. Although the design of the complete spectrometer is small (60x44x28 mm^3), light (280 g) and fairly accurate ($\pm$ 0.05%) it only has a dynamic range of several percent depending somewhat on the gas, which is clearly too small for the purpose of natural gas detection. This is mainly dependent on the length of the optical path though and is not a fundamental problem of this design. A shorter path will increase the dynamic range at the cost of worsening the accuracy.

A completely different approach is taken by Rubio *et al.* [59–61]. They designed a so called non-specific NDIR detector. It is composed by an array of broadband infrared filters and a matching array of thermopile detectors joint together by means of flip-chip bonding. The elements of the filter array are not tuned for the specific measurement of any gas. Instead, they use a multivariate regression technique (Partial least squares) to predict the gas concentrations. This omits the traditionally required reference channel by using digital component correction techniques. The main advantage of this system is that it 'only' requires an array of 3x3 or 4x4 filters and detectors to be able to detect any number of gases that have their absorption peak in the 2.5 to 10 μm range. Also this design is focused on a high accuracy, low dynamic range

market.

At the other side we can find several devices which have been designed to detect a single specific gas (mostly CO_2) [62–64]. The most interesting probably being the SensorChip^{TM}designed by ICx^{TM}Photonics [64]. This miniature device generates narrow band infrared radiation tuned to CO_2 by using a hot filament source in combination with photonic crystals, eliminating the need for optical filters. A miniature vacuum encapsulation and very high power conversion efficiency combine to provide a low case temperature and intrinsically safe operation. The chip only contains the source, but can also act as a narrow band infrared bolometer detector, when the setup it's used in, is designed as a retro-reflecting optical cell. It's detection range can be up to 100% and sensitivity down to 100ppm, depending on the optical path length of the setup.

Tunable Fabry-Pérot filters

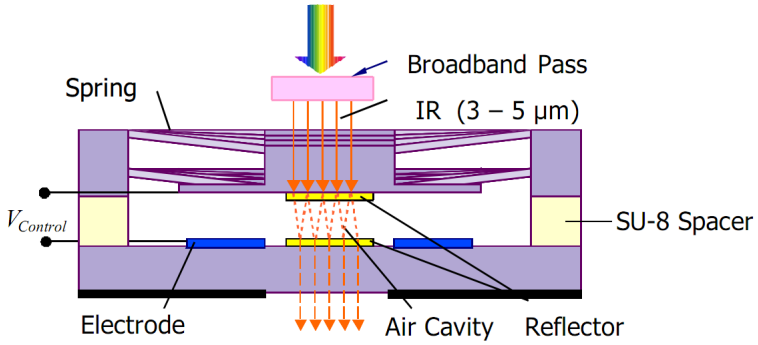

Figure 6.11: Tunable Fabry-Pérot filter as designed by Neumann [50].

If it would be required to dynamically select a wavelength, there is the option of the tunable Fabry-Pérot filter. One such design is described by Lammel [65], in which a micromachined porous silicon interference filter is tuned by thermally actuating the filter such that the angle of incidence of the light is changed. According to the report a resolving power of 25 is possible for a device of about 2.5 by 3 mm^2. Which although inferior to other options, they still consider good enough for the purpose of gas detection. Another advantage according to them is that this device may result in a single pixel multi-gas spectrometer, without the complexity of a grating based system. There are several things to this system though, which may be considered downsides. First of all, the gas concentrations would be measured sequentially, because there is only one pixel. Second, the central wavelength of the filter can be tuned only by a factor 1.16, which in this particular case will only allow for CO and CO_2 detection with one such device. Gases which have their absorption bands somewhat further a part, will therefore still require their own detection system. Third, the cantilever actuators may be considered fragile. Last, integration with the detector on the same chip will not be possible because of the construction and setup of the filter.

A more interesting design is that presented by Neumann [50]. Here two electrostatically actuated filters are designed to together cover the complete range of 3-5 μm. One filter covers the range of 3.0 - 4.3 μm, the other 3.7 - 5.0 μm. The splitting of the spectral range into two parts was mainly because they were unable to produce Bragg reflectors with more than 2 layers without a dramatic increase in the roughness of the stack. However, the typical FWHM bandwidths of the filters are 100±20 nm and 80±20 nm, which seems in the order of what we

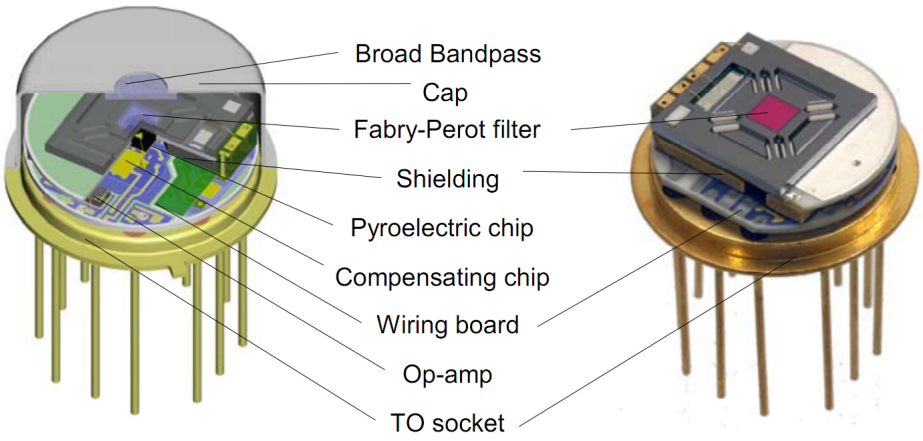

Figure 6.12: Schematic drawing (left) and picture of a sample (right) of a tunable pyroelectric detector with integrated filter [50].

would like. According to the authors, a limited finesse of 57 was probably due to the warping of the reflectors, which means that with more effort, even better results can be accomplished. A downside that will always remain is high drive voltage required to tune the filter. In this case the maximum required drive voltages are 27 V and 60 V, depending on the filter used. It incorporates a pyroelectric detector with a responsivity of 160,000 V/W. The specific detectivity of the tunable detector was finally found to be higher than $4 \cdot 10^6$ cm $Hz^{1/2}$ W^{-1}. As has been seen often, the system only includes a detector and the wavelength selecting device. Therefore it cannot be called a complete micro-spectrometer system, since it would still require a sample chamber and source to be designed before it can detect any gases.

Linear Variable Optical Filters (LVOF's)

When movable optics cannot fulfill the requirements, but there is the need for a variable filter, another option is to utilize a Linear Variable Optical Filter (LVOF) as described by Emadi in [51]. He reports the design of an LVOF with a resolving power of 70-80 with a spectral range of 3 - 5.5 μm.

Another device utilizing an LVOF is the Wilksir InfraSpec VFA-IR Spectrometer [66]. Although it is not strictly considered a micro-spectrometer, it still requires attention. This fairly small (15.2x16.5x7 cm^3), light (1.5 kg) and cheap spectrometer is designed to be portable and is based on a linear variable filter with a 128 pixel pyroelectric array. It covers the 2000 - 4000 cm^{-1} range with a resolution of 25 cm^{-1}. Although it is not designed to cope with gases, it does show the potential of this concept.

Other proofs of concept are given by Nogueira and Wiesent [67, 68]. Both systems are build with discrete components to analyze several gas and liquid compositions. Noquiera uses an LVOF on top of a 64 pixel pyroelectric detector array, from which the data is further processed to get the final results. No further figures are given on the resolution or dynamic range. Wiesent describes a setup with 32, 64, 128 or 256 pyroelectric pixels for lubricant condition monitoring.

Hara [69] describes the use of an LVOF in a CO_2 detector. Two bolometers with a detectivity of $1.1 \cdot 10^8$ cm $Hz^{1/2}$ W^{-1} were tuned to the CO_2 absorption band and the reference band. It detects CO_2 up to 5000 ppm.

Advantages of NDIR systems:

- Lack of fragile components
- Self calibrating
- High resolving power over a narrow spectral band
- High optical throughput
- Relatively simple

Disadvantages of NDIR systems include:

- Not as good for wide spectral band operation
- Might need several filters to be able to detect all the required gases

6.4 Diffraction

From a physical point of view, there is no significant distinction between diffraction and interference, in that the pattern created by diffraction is also an interference pattern. However, diffraction is often considered a somewhat special case. It has become customary to speak of interference when considering the superposition of only a few waves and diffraction when treating a large number of waves. [70]

6.4.1 Introduction to the grating equation

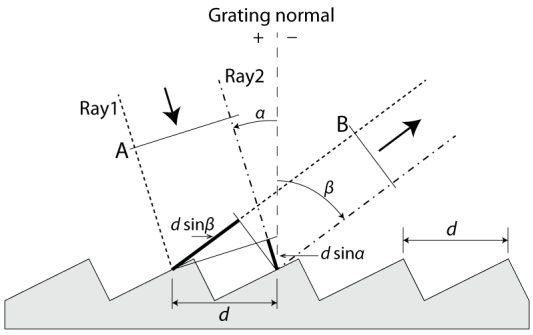

Figure 6.13: Geometry of one diffraction angle for a planar wavefront. Rays 1 and 2 are in phase at wavefront A and will also be at wavefront B if and only if the geometry fulfills the grating equation, leading to constructive interference. The sign convention for the angles is given by the + and - signs.

When monochromatic light is incident on a grating surface, like that shown in figure 6.13, it is diffracted into discrete directions. We can picture this process by thinking of each grating groove as being a very small, slit-shaped source of diffracted light. This light combines to form a set of diffracted wavefronts. Figure 6.13 shows one such wavefront. The usefulness of a grating depends on the fact that there exists a unique set of discrete angles along which the diffracted light from

each facet is in phase with the light diffracted from any other facet, leading to constructive interference. This process is expressed by the grating equation [71]:

$$\begin{aligned} &m\lambda = d(\sin\alpha + \sin\beta) \\ &\text{or:} \\ &\beta(\lambda) = \sin^{-1}\left(\frac{m\lambda}{d} - \sin\alpha\right) \end{aligned} \tag{6.21}$$

Where m is an integer number called the diffraction or spectral order, λ is the wavelength of the light, d is the groove spacing, α is the angle of incidence and β the angle of the refracted wave. An important note here is that this equation is restricted to the case in which the incident and diffracted rays lie in a plane which is perpendicular to the grooves (at the center of the grating). The majority of grating systems fall within this category, which is called classical or in-plane diffraction. Also, although the + sign in the first equation might not seem to make sense, it is correct because of the right hand plane position of β, making $d\sin\beta$ negative.

Since $|\sin\alpha + \sin\beta| \not> 2$, only those diffraction orders for which $-2d \leq m\lambda \leq 2d$ will exist, limiting the amount of possible diffraction orders for any given λ. However, it does show that most light will have multiple orders of diffraction. The most troublesome aspect of multiple order behavior is that successive spectra overlap as shown in figure 6.14(a). It is evident from the grating equation that light of wavelength λ diffracted along direction β will be accompanied by integral fractions $\lambda/2$, $\lambda/3$, etc. A detector sensitive to both wavelengths would see both simultaneously. This superposition of wavelengths is inherent in the grating equation itself and must be prevented by suitable filtering (i.e. order sorting).

Looking at equation (6.21) and figures 6.13 & 6.14, several interesting things can be seen. First we can identify two special cases. When $m = 0$, the grating acts as a mirror and the wavelengths are not separated ($\beta = -\alpha$ for all λ); this is called *specular reflection* or simply the zero order. The other special, but common case is that in which the light is diffracted back towards the direction from which it came (i.e. $\alpha = \beta$); this is called the *Littrow configuration.*

Second, the width of the incident beam, is clearly not the same as that of the diffracted beam. This is called *anamorphic magnification* and is given by [71]:

$$\frac{a}{b} = \frac{\cos\beta}{\cos\alpha} \tag{6.22}$$

Where a and b are the widths of the incident (A) and refracted (B) wavefronts, respectively. Since α and β are dependent on λ through the grating equation (6.21), this magnification will vary with wavelength. The grating equation also guarantees that this ratio will not equal unity unless specular reflection or the Littrow configuration is used.

The primary purpose of a diffraction grating is obviously to disperse light spatially by wavelength. A beam of white light incident on a grating will be separated into its component wavelengths upon diffraction from the grating, with each wavelength diffracted along a different direction (except for $m = 0$). Dispersion is a measure of the separation between diffracted light of different wavelengths. The angular dispersion, D in [deg/nm], of a spectrum of order m between wavelengths λ and $\lambda + \Delta\lambda$ can be obtained by differentiating the grating equation, assuming the incidence angle α to be constant [71]:

$$D = \frac{\mathrm{d}\beta}{\mathrm{d}\lambda} = \frac{m}{d\cos\beta} = \frac{\sin\alpha + \sin\beta}{\lambda\sin\beta} \tag{6.23}$$

As the groove pitch, d, decreases, the angular dispersion increases, meaning that the angular separation between wavelengths increases for a given order m. Except that d is limited by the

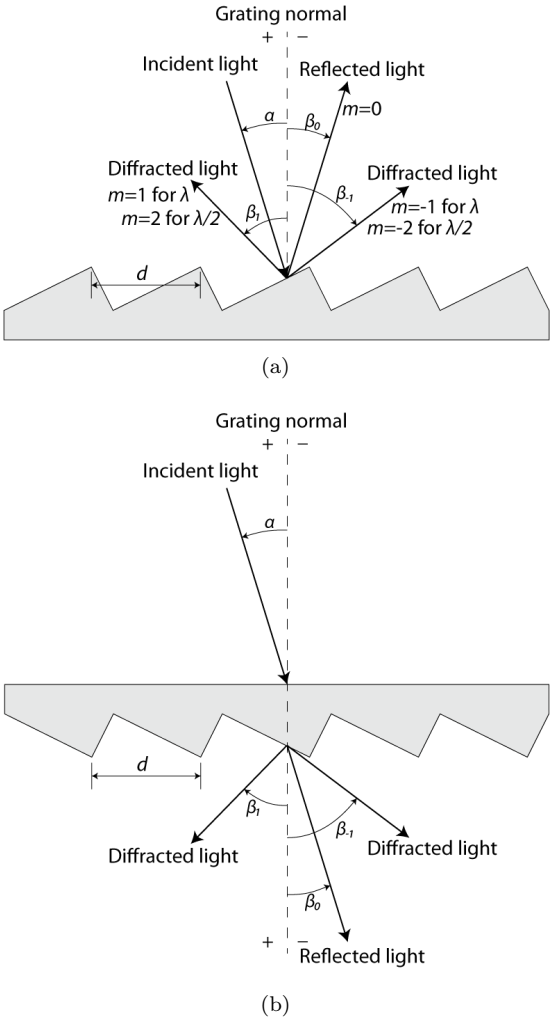

Figure 6.14: Overlapping of spectral orders. The light of wavelength λ will, in the first order, be diffracted in the same direction as the light of wavelength $\lambda/2$ in the second order. Specular reflection is present for $m = 0$. (a) Reflection grating: the incident and diffracted rays lie on the same side of the grating, (b) Transmission grating: the diffracted rays lie on the opposite side of the grating from the incident ray.

minimum feature size of the lithographic process, it is also important to realize again that the quantity m/d is not a ratio which may be chosen independently of other parameters. It still has to fulfill the same requirements as stated above, where $-2 \leq \frac{m\lambda}{d} \leq 2$.

Now, given a diffracted wavelength λ of order m (corresponding to an angle of diffraction β as described by equation (6.21)), the linear dispersion in [mm/nm] of a grating system is the

product of the angular dispersion D and the effective focal length $r'(\beta)$ of the system [71]:

$$\begin{aligned} r'D &= r'\frac{\mathrm{d}\beta}{\mathrm{d}\lambda} = \frac{mr'}{d\cos\beta} \\ &\text{or its reciprocal:} \\ P &= \frac{d\cos\beta}{mr'} \end{aligned} \tag{6.24}$$

6.4.2 Resolving power of gratings

The resolving power of a grating also adheres to equation (2.2). In a grating it is useful to consider the resolving power as being determined by the maximum phase retardation of the extreme rays diffracted from the grating. The theoretical resolving power of a uniformly grooved, planar diffraction grating, which is illuminated by a collimated light beam, is given by [43, 71]:

$$RP = \frac{\lambda}{\Delta\lambda} = mN = \frac{W(\sin\alpha + \sin\beta)}{\lambda} \tag{6.25}$$

where W is the illuminated, ruled width of the grating given by $W = Nd$, with N the number of grooves illuminated on the surface of the grating and d is the groove spacing. Since $|\sin\alpha + \sin\beta| < 2$ still applies, the maximum attainable resolving power becomes:

$$RP_{max} = \frac{2W}{\lambda} \tag{6.26}$$

regardless of the order m. This maximum condition corresponds to the grazing Littrow configuration, i.e. $|\alpha| \approx 90°$ (grazing incidence) and $\alpha \approx \beta$ (Littrow). Of course, the practical resolving power of any grating does not only depend on the angles α and β, but also on the optical quality of the grating surface and the uniformity of the groove spacing.

Still though, the resolving power of a grating can be much higher than that of a prism of comparable size. For example, a 7mm grating with a groove spacing of 2 μm has a first order resolving power of 3500, while the resolving power of a prism with a 7mm long base is only 1000. [43]

6.4.3 Free Spectral Range of gratings

As explained before, light of several wavelengths (each in a different order m) will be diffracted along the same direction. The free spectral range of a grating is therefore defined as the range of wavelengths in a given spectral order, for which superposition of light from adjacent orders does not occur. It can be calculated directly from its definition (as also illustrated in figure 6.14 and from equation (6.21)): the wavelength of light in order $m+1$, that is diffracted along the same direction of light of wavelength λ_m in order m, is λ_{m+1}, such that:

$$\beta(\lambda_m) = \beta(\lambda_{m+1}) \rightarrow m\lambda_m = (m+1)\lambda_{m+1} \tag{6.27}$$

from which we can define the free spectral range as:

$$\mathrm{FSR} = \lambda_m - \lambda_{m+1} = \frac{\lambda_{m+1}}{m} = \frac{\lambda_m}{m+1} \tag{6.28}$$

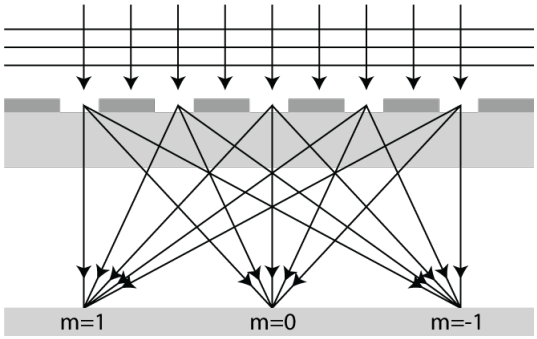

Figure 6.15: Multi-slit transmission grating

6.4.4 Downscaling a grating

Trying to implement a grating in a micro-system, comes with its own difficulties. The most efficient grating is for example the standard reflective diffraction grating as shown in figure 6.14(a). However, the fabrication of this type of grating is less IC compatible compared to, for example, a multi-slit type grating as shown in figure 6.15, which is much more planar. The choice on which to use is application dependent.

6.4.5 State-of-the-art

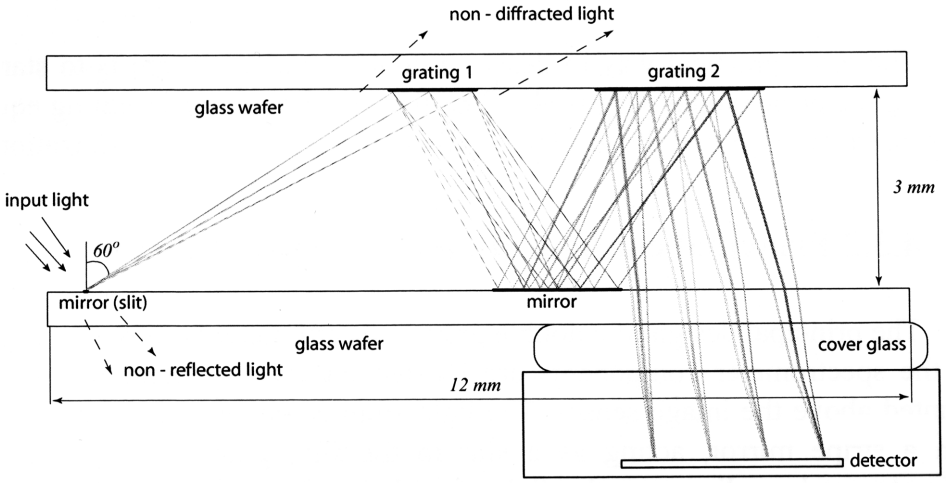

Figure 6.16: Example of a dispersive infrared micro-spectrometer. [43]

Gratings are at the heart of Dispersive Infrared (DIR) spectrometers. Two basic grating setups can be found in both macro- and micro-spectrometers: reflection and transmission gratings. As was already illustrated earlier in figure 6.14, reflection gratings have both diffracted and incident light on the same side of the grating, whereas transmission gratings have the diffracted and incident light on opposite sides.

Imaging gratings are relatively easy to implement in waveguide-based systems. Several reports of such compact spectrometers are found in literature [72, 73]. Classical spectrometers with a planar diffracting grating have also been demonstrated [74]. These spectrometers have a volume typically in the 1 cm^3 range with a 5 nm resolution within 100 nm spectral range within the visible region. In [73] the authors expect, based on numerical simulations, a theoretically feasible FWHM resolution of 2 nm within a 300 nm FSR for a waveguide spectrometer.

In [43, 75–77] Grabarnik describes two possible setups and compares these. Both take a volume of about 50 mm^3, where one uses a single grating and one a double grating setup. He concludes that the double gating setup provides superior performance in both FWHM resolution (6-10 nm for the single and 3 nm for the double grating) and FSR (100 nm for the single and 200 nm for the double grating) at the obvious cost of complexity.

All these reports are within the visible range though and do not describe systems capable of proper diffraction in the mid infrared. One device that is designed for the mid infrared is described by Kong [42]. Here, a multi-slit transmission grating as that shown in figure 6.15 is used to diffract a collimated beam onto a thermopile detector array, resulting in a FWHM resolution of 0.6 μm at an FSR of about 6 μm, with a response of about 0.4 V/W over the full FSR.

Miniaturized setups can also be realized with tunable gratings as those described in [78, 79]. These will allow for a tunable range of 8-10% from the visible all the way up to the mid infrared. Looking at the spectrum to be covered for this particular application, the tunable range of 8-10% is simply too small and will therefore not be of much benefit compared to an array type spectrometer.

No grating based mid-infrared micro-spectrometer was found which was tested for the purpose of gas detection. Therefore no figures of resolution or dynamic range can be stated.

Advantages of DIR systems may include:

- Relatively high resolution for the wide free spectral range

Disadvantages of DIR systems include:

- Gratings are considered relatively fragile and expensive components
- More difficult to miniaturize

6.5 Concept choice

As also discussed in [18], NDIR spectrometers are probably the most promising spectrometers for further research, because these are most likely to fulfill all earlier stated requirements by means of a straight forward and reliable construction with good optical performance.

As described, a lot of work has been done in the field of infrared spectroscopy (in particular the field of NDIR spectroscopy), which might leave the impression that there are no more research opportunities left. However, with the request for a super small and cheap gas composition sensor, which should be able to cope with an extremely wide dynamic range in gas compositions, new efforts will have to be put into a reevaluation of what can be done. Comparison of what has been done and what is required identifies the main research opportunities:

- Many of the systems presented are developed for trace gas detection (small dynamic range, high accuracy), where the requirements of this sensor stated the a dynamic range of up to 0-100%.

- Although many micro-spectrometers have been presented, none is a complete device that really covers the small size and large amount of integration we are looking for.

Since we would like to use an NDIR micro-spectrometer, we basically have three options: One interferometer for every pixel, a tunable filter with a single pixel or a Linear Variable Optical Filter (LVOF) across a complete array of pixels. Designing an interferometer that is different for every pixel would create a design that is very difficult to produce because of all the different layer thicknesses. The LVOF on the other hand is really simple to produce and also may give us the opportunity to detect the complete spectrum with a single dispersing element. This makes the system more flexible to be used in other applications, either by a small redesign for spectra outside the 3-5 μm or even only by using different read-out software if the absorption peak of interest is within this band.

The use of a tunable filter can also be interesting. The main disadvantage would be the more complex production process, fragility, high operating voltages and the sequential detection. Since the transition time within the gas composition is considered to be much larger than the scanning time, the sequential detection should not be a big issue. A major advantage of a tunable filter would be that you would only need two pixel-filter components to cover the whole 3-5μm range, which gives the opportunity to design very large pixels, limited solely by the thermal inertia of the pixel. This would therefore probably give a smaller footprint with a higher detectivity at the cost of complexity (as well as in the production process as in the drive electronics) and a greater chance of decreased reliability.

The final choice for the LVOF has been made because the advantages of the tunable filter do not seem to outweigh the disadvantages. Also important of course, has been the knowledge of LVOF design already present within our research group.

6.6 Infrared filters

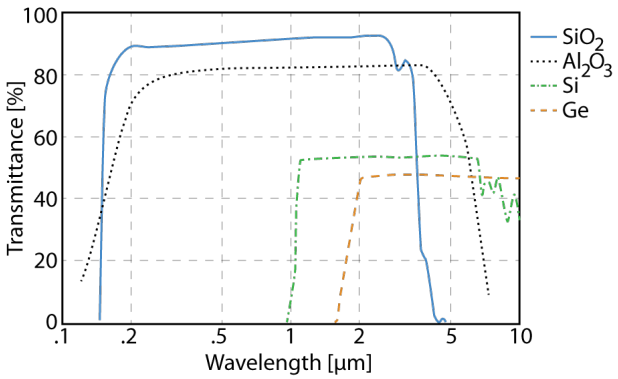

Figure 6.17: Typical transmission plots for some materials that are (semi-)transparent in the mid-IR. [80]

Except the prism, all dispersing elements suffer from higher order transmission. If these wavelengths would not be blocked by some sort of filter, the signal could have offset, or even worse, could be sensitive to another gas. On the other hand, every added layer of material through which the light has to travel, will decrease the light intensity either by absorption or reflection. Proper filter design is therefore very important.

6.6.1 Infrared windows

Some materials are natural filters, in that they quickly change from being transparent or translucent at one wavelength and opaque at the next. These materials can easily be used as windows to block unwanted parts of the spectrum. As shown in figure 6.17, examples of materials that may act as infrared pass filters are: Crystalline Quartz (SiO_2), Sapphire (Al_2O_3), Germanium (Ge) and crystalline Silicon (Si).

The major advantage of using a single material as filter is that there is no interference and thus no higher order transmission. The downside is obvious as well: the transmission spectra cannot really be engineered.

6.6.2 Thin-film filters

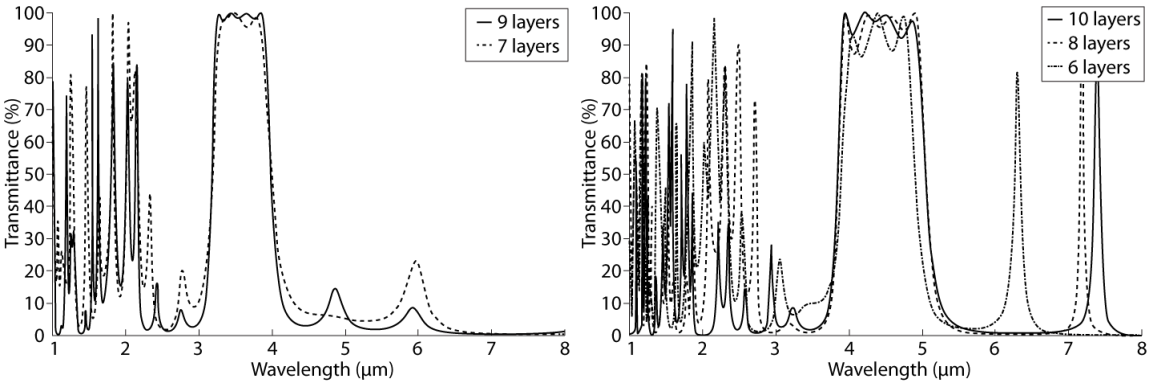

(a) (b)

Figure 6.18: Examples of bandpass filters to be used for a) C_xH_{2x+2} and b) CO and CO_2 detection.

If we look at the cause of the maximum transmittance of Si, we see that it is limited solely by its reflectance. Therefore we could create an anti-reflection coating which suits the required wavelength range. Because of its dependence on wavelength, this anti-reflection coating acts as a thin-film pass-band filter as shown in figure 6.18 and table 6.1.

However, there is more to it of course. One can fairly easy design and simulate a filter, with very sharp drop-off and very little ripples, but this will require many layers. Each layer will already be quite thick due to the wavelength. Stacking over 10 layers to create a filter would make not only for a very thick filter, but also one that is very difficult, if not impossible, to produce. Obviously this will also not affect the cost positively.

6.7 Modeling

Cell title: TRANSMITTANCE CALCULATIONS
Sub-function(s):

Filters are designed with the Essential Macleod software as described in more detail in the next section. The outcome of this design is then exported to a .tbl-file. For the LVOF, this .tbl-file

(a)

Material	**Thickness [nm]**
SiO_2	387
PolySi	502
SiO_2	213
PolySi	624
SiO_2	1325
PolySi	223
SiO_2	1213
PolySi	757
SiO_2	1225

(b)

Material	**Thickness [nm]**
PolySi	58
SiO_2	538
PolySi	646
SiO_2	505
PolySi	568
SiO_2	1228
PolySi	58
SiO_2	1694
PolySi	427
SiO_2	1494

Table 6.1: Infrared bandpass filters as shown in figures 6.18(a) (9 layers) and 6.18(b) (10 layers), respectively.

may be converted to a .txt-file with the right layout by using the "*Macleod_to_Matlab_LVOF.m*" function. Others may use the "*Macleod_to_Matlab.m* function.

The function for conversion of LVOF data will require several .tbl-files, each being the transmittance of a Fabry-Pérot structure where the thickness of the resonator cavity is different for each file. All the files will be combined to create some sort of envelope which gives the full transmittance spectrum of the LVOF in the region of interest. It is assumed that outside this region, the exact transmittance is less important since most of this light will be either blocked by other optics or not absorbed by the detector.

6.8 Detailed design

Material	**n**	**k**	**Deposition temp. [°C]**	**Melting point [°C]**
SiO_2	1.39	0	700	
SiN (PECVD)	2.05	8E-5	350	
SiN (LPCVD)	2.15	0	850	
Mo	2.32	22.98		2650
SiC	2.56			
PolySi	3.93	0	580	
Ti	4.66	7.27	350	1670
TiN	5.90	10.97	350	2930
Al	6.10	30.40	350	660

Table 6.2: Listing of IC compatible materials available at DIMES in order of increasing refractive index n. Optical properties are given for a wavelength of 4 μm. Deposition temperatures are approximate.

Since the filters are intended for use in an integrated system, it is important that the materials used are IC compatible. We therefore should list the available IC compatible materials with their optical properties and process temperature as shown in table 6.2

As discussed in section 6.3.2.2, the best performance for the LVOF is obtained when reflector materials have a negligible extinction coefficient and refractive indices that are far apart. Therefore, Polycrystalline Silicon (poly-Si) and Silicon Dioxide (SiO_2) have been chosen as the high-n and low-n materials, respectively. In the mid infrared, poly-Si has an extinction coefficient (k) which is practically zero. If one would look at the dependence of the extinction coefficient of SiO_2 on wavelength, one can see a sharp increase beyond 3 μm. However, up to 6.5 μm it is still considered small enough to be negligible for the small layer dimensions we are interested in.

The next step is to determine the order of the filter. Higher order will theoretically give higher reflectivity as shown earlier in figure 6.9, but at the cost of a more complex fabrication process.

Using the commercially available Essential Macleod software, the layer thicknesses of the stack have been defined. The layer thicknesses of the original designs are given in table 6.3. Unfortunately due to a mistake in communication, other designs were fabricated. These designs are presented in table 6.4. The transmittance plots of all four designs are shown in figure 6.19. It can be seen clearly that the transmittance of the fabricated design is significantly lower, on the other hand, the free spectral range is slightly enlarged, increasing the finesse.

Layer#	**Material**	**Physical thickness 3-4μm range [nm]**	**Physical thickness 4-5μm range [nm]**
Medium	Air		
1	SiO_2	278	370
2	PolySi	200	261
3	SiO_2	556	740
4	PolySi	200	261
5	SiO_2	1000-1700	1400-2200
6	PolySi	200	261
7	SiO_2	556	740
8	PolySi	200	261
9	SiO_2	278	370
Substrate	Si		

Table 6.3: Original Linear Variable Optical Filter designs for the 3-4μm and the 4-5μm range.

To be able to cover the whole detector array, the LVOF should be 10 mm long. Having a long LVOF for a certain bandwidth will also reduce the slope and thus the FWHM according to equation (6.17), where Δx is equal to the pixel width.

6.9 Fabrication

The fabrication of LVOF's has been extensively researched by Emadi [51]. This research resulted in a fully IC-compatible, reflow based process, where the taper angle is fully defined by mask design.

Layer#	**Material**	**Physical thickness 3-4μm range [nm]**	**Physical thickness 4-5μm range [nm]**
Medium	Air		
1	SiO_2	593	697
2	PolySi	229	269
3	SiO_2	593	695
4	PolySi	229	269
5	SiO_2	830-1600	1250-2100
6	PolySi	229	269
7	SiO_2	593	697
8	PolySi	229	269
9	SiO_2	593	697
10	PolySi	229	269
Substrate	Si		

Table 6.4: Fabricated Linear Variable Optical Filter designs for the 3-4μm and the 4-5μm range. NOTE: Thicknesses are not the true thicknesses after fabrication.

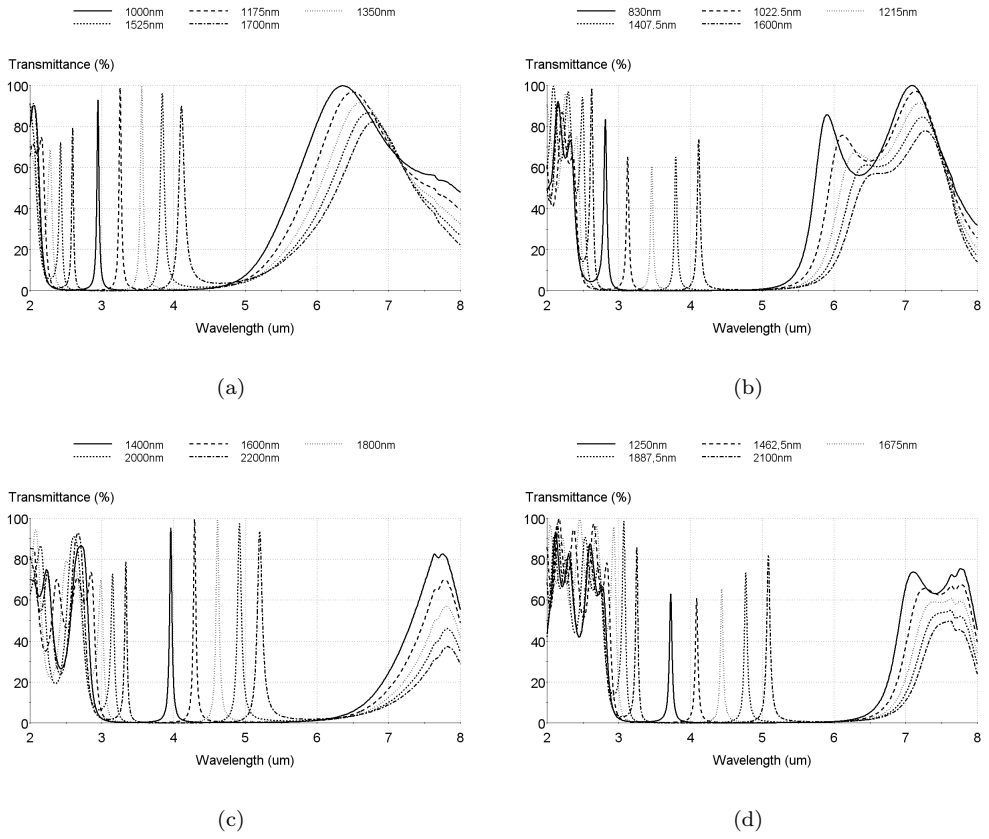

Figure 6.19: Transmittance plots of a) original design for 3-4μm window, b) fabricated design for 3-4μm window, c) original design for 4-5μm window and d) fabricated design for 4-5μm window.

Because there was already a mask available from previously fabricated LVOF's this mask will be used for fabrication. This does mean that the LVOF will not be shaped as initially designed. The mask does have 10 mm long LVOF's, but these are double tapered, resulting in a triangular shape as shown in figure 6.20. Their bandwidth will therefore be only half of that intended.

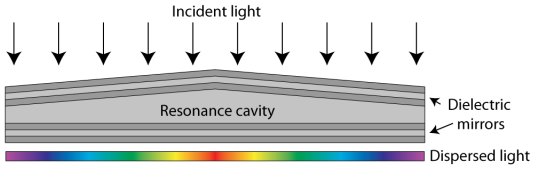

Figure 6.20: Schematic drawing of LVOF layers for a double tapered LVOF.

After the bottom dielectric mirror, the tapered cavity layer is to be deposited. In the particular case of the 3-4μm LVOF, initially a 1800 nm thick layer of SiO_2 is deposited, followed by about 4 μm of AZ4562 photoresist. To create the taper, only one masked lithography step is required. During this step, trenches are created in the photoresist. Subsequently, the material in the tranches is removed and followed by a reflow process. This effectively reduces the resist layer thickness by a value defined by localized trench density. Hence a taper can be flexibly programmed by mask design to be from 0.001° to 0.1°.

At this point, it is the resist which is tapered, which still has to be transferred to the cavity material. The transfer is done by etching up to the point where the resist is gone completely. The etching is performed using a CHF_3 + Ar plasma etch, which is operated at minimum pressure (about 3 mTorr). Because the etch rate may change quite a bit every time the process is performed, it is important to have in-situ measurements of the etch rate. This is done by reflecting a laser of the resist during the etching. The period of the reflection is a measure of the etch rate [nm/min] by:

$$\text{Etch rate} = \frac{1500 \text{ nm}}{\text{Time of one period}} \tag{6.29}$$

Because the refractive index and etch rate of both the resist and SiO_2 are very similar, one period is added to the etch time. This over etch should reduce the cavity thickness about 200nm leaving a cavity which is 1600nm at its thickest point. All together the total etching time will be about 4 hours.

Chapter 7

Infrared detectors

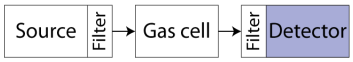

7.1 Introduction

Observing the history of the development of the IR detector technology, a simple theorem, after Norton [81], can be stated: "All physical phenomena in the range of about 0.1-1eV can be proposed for IR detectors". This makes the world of infrared detectors a vast one. To be able to keep an overview there is one easy distinction to be made. Infrared detectors can be put in either of two categories: photodetectors (i.e. Photon detectors) or Thermal detectors. As the names suggest, their detection principle is fundamentally different as will be explained below.

To be able to compare the different types of detectors a figure of merit is used that is referred to as the normalized or specific detectivity, D^* [cm $Hz^{1/2}$ W^{-1}], given by:

$$D^* = \frac{\sqrt{A\Delta f}}{NEP} = \frac{\mathcal{R} \cdot \sqrt{A}}{S_n} \tag{7.1}$$

where A is the surface area of the radiation absorber [cm^2], Δf is the noise bandwidth [Hz], NEP is the Noise Equivalent Power [W], $\mathcal{R}$ is the responsivity in [V/W] or [A/W] and S_n is the accompanying noise spectral density in [$V/Hz^{1/2}$] or [$A/Hz^{1/2}$], respectively.

It should be noted that the definition of specific detectivity, D^*, was originally proposed for photodetectors, in which the noise power is always proportional to the detector area. However, the noise in thermal IR detectors does not always obey this scaling trend (e.g. temperature fluctuations or the effects of Joule heating by the read-out circuit). Therefore, D* should be very cautiously interpreted when applied to thermal IR detector. In fact, D* tends to overestimate the performance of larger absorbing area thermal detectors and underestimates the performance of smaller ones [82]. However, since most detectors under consideration will be moderately sized and the detectivity will only be used to give a rough idea about the performance of several different types of detectors, it is still considered to be good enough for comparison purposes.

Using this figure of merit, spectral detectivity curves for a number of commercially available infrared detectors are shown in fig. 7.1. For the purpose of natural gas detection, the region of interest is mainly focused on the $3 - 5\mu m$ window (i.e. Mid Infrared (MIR) or Mid-wave Infrared (MWIR)) as is also stated in the requirements in section 3.2. Looking at this figure we can identify the difference in the fundamental limits of photdetectors and thermal detectors: photodetectors will have a high sensitivity with a low bandwidth, whereas thermal detectors will have a relatively low sensitivity with a high bandwidth.

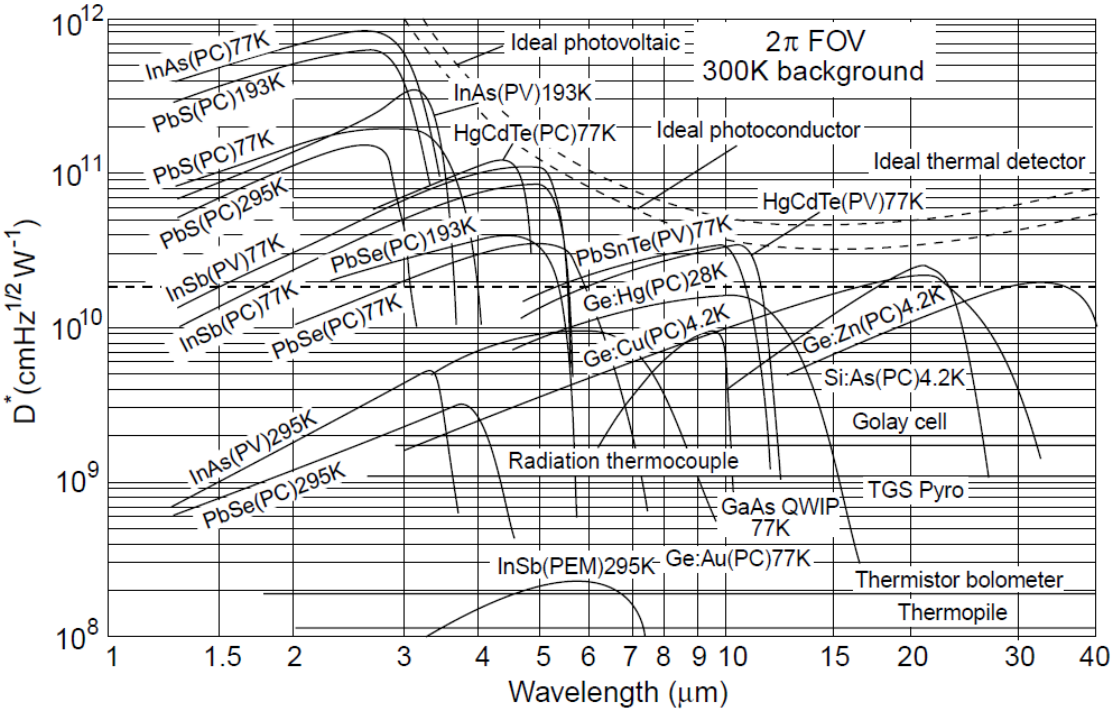

Figure 7.1: Comparison of the specific detectivity, D^*, of various commercially available infrared detectors when operated at the indicated temperature. Chopping frequency is 1000 Hz for all detectors except the thermopile (10 Hz), thermocouple (10Hz), thermistor bolometer (10Hz), Golay Cell (10 Hz) and the pyroelectric detector (10 Hz). Each detector is assumed to view a hemispherical surrounding at a temperature of 300K. Theoretical curves for the background-limited D^* (dashed line) for ideal photovoltaic (PV), photoconductive (PC) and thermal detectors are also shown. PEM - photoelectromagnetic detector. [83]

7.2 Photodetectors

Still the slightly smaller area of photodetectors can prove quite overwhelming. Here it is important to know what is a fundamental physical effect, what is a group of effects, what is a mode of operation and what is 'just' a type of photodetector. This thesis will give a short overview of the field of photodetectors from the perspective of the fundamental physical effects, since this is most likely a more exhaustive way (e.g. Newly developed types of photodetectors are more likely to fit in any of the described categories than the other way around).

We can already distinguish two different groups or categories of physical effects. The first categorie comprises of the so called interband effects, which includes the Photoemissive effect and the Intrinsic and Extrinsic Photoelectric effects. The second category is that of the intersubband or Quantum effects like Superlattices, Quantum Wells and Quantum Dots. A visual explanation of these effects can be seen in figure 7.2. Depending on how the electric or magnetic fields are developed, there are various modes of operation such as photoconductive, photovoltaic, photoelectromagnetic (PEM) and photoemissive ones. Each material system can be used for different modes of operation [83]. These are not to be confused with the fundamental physical interaction

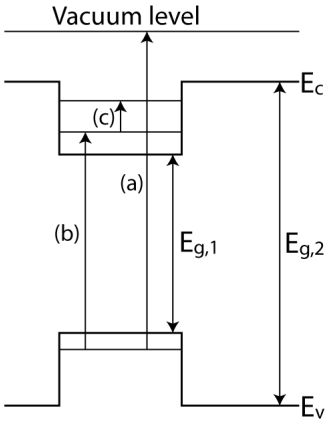

Figure 7.2: Basic band diagram for a sandwiched semiconductor with bandgap $E_{g,1}$, by a semiconductor with bandgap $E_{g,2}$. (a) is an interband transition of the photoemissive effect (b) is an interband transition of the intrinsic photoelectric effect and (c) is an intersubband transition.

between the incident photons and the excited electrons. The mode of operation can be seen as a description of what is done with the excited charge carriers, not how they are created.

By definition a photodetector is a device which absorbs the incident radiation by interaction with electrons. These electrons can either be bound to lattice atoms or impurity atoms, or they can be free electrons. To be able to excite an electron to a higher energy state, the incident photon should contain at least the same amount of energy as the energy gap to get to this state. The energy associated with a photon is described by $E = hc_0/\lambda$, where h is Planck's constant, c_0 is the speed of light in vacuum and λ is the wavelength. Since in this particular case the highest wavelength in the region of interest is $5\mu m$, the associated energy is only 0.248 eV. This means that, for the detector to work, the work function, ϕ of a metal or the bandgap energy (i.e. activation energy), E_g, of a semiconductor can only be a maximum of 0.248 eV.

If we would look at the bandgap energy of several common semiconductors, we see that this will not be an easy task [21]. Fortunately some clever tricks have been invented to decrease the bandgap to a point where detection in the mid-IR is perfectly possible as will be shown later. Unfortunately there is an intrinsic problem to the decrease of the bandgap. Lowering the bandgap energy, exponentially increases the charge carriers generated due to thermal agitation, making uncooled devices very noisy. On top of that there will be an increased Auger recombination, adding to the overall difficulties of making efficient devices in the infrared region. Notwithstanding these problems, the fundamental processes at play here lead to sub-nanosecond recombination rates and thus to fast devices capable of being modulated in both emission and absorption in the GHz range [84]. The cooling requirements are the main obstacle to the more widespread use of IR systems based on semiconductor photodetectors making them bulky, heavy, expensive and inconvenient to use. However, recent developments have shown that room temperature photodetectors are being developed, which might just be the holy grail in the world of infrared detection.

To fully understand the design decisions made it seems important to get a good feeling of what is there. Therefore, a brief but fairly complete overview of the different fundamental physical effects at play in photodetectors and their associated weaknesses and strengths, are all described below. For a more detailed overview the reader is referred to [83–86]. The reader should be

aware that this overview is certainly not exhaustive and that new types of photodetectors are developed continuously. Again, this section is only for the purpose of understanding the design decisions made later. Reviewing them all would be a thesis on its own.

7.2.1 Photoemissive effect

The photoemissive effect is defined as the ejection of an electron from its ground state to the vacuum level (see also figure 7.2), when struck by a photon with sufficient energy (e.g. more than the work function of the material). The charge carrier is thereby by definition a majority carrier. Two types of photoemissive effect can be distinguished, the external and the internal. Photoemissive detectors were the first photodetectors to replace photographic plates in spectrometer instrumentation.

7.2.1.1 External photoemissive effect

The external photoemissive effect is basically defined as the release of electrons to the surface of a material by incident photons, where the electron is transfered from its original electrode (the cathode) to the receiving electrode (the anode), by means of an electric field. Phototubes (PTs) and Photomultipliers (PMTs) are examples of devices that use this effect. Photomultipliers utilize several secondary electrodes (dynodes), where the first electrons released are accelerated on to the next electrode such that they release several per incident electron (i.e. every electron is multiplied). By doing this several times, the photocurrent can be amplified extensively.

Figure 7.3: An old fashioned photomuliplier. (At the courtesy of http://www.rhunt.f9.co.uk)

Although phototubes and photomultipliers can be extremely sensitive from the UV to Near Infrared (NIR), not too many materials are known which have a work function low enough to work in the mid infrared part of the spectrum, that also have a high conversion efficiency. Since they are also quite bulky and require a high operating voltage, the research into PTs and PMTs is only restricted to a couple very specific applications.

7.2.1.2 Internal photoemissive effect

The internal photoemissive effect (e.g. Free carrier effect) is basically the same as the external photoemissive effect, except that the charge carrier will never travel across a true vacuum. It stays inside the solid-state device so to speak. A PtSi Schottky barrier photodetector is a typical example of an internal photoemissive device.

7.2.2 Intrinsic Photoelectric effect

When intrinsic photodetectors absorb energy (e.g. an increase in temperature or photon energy), electrons that were at rest in the valence band will be passed into the conduction band, creating electron-hole pairs which will act as minority charge carriers. In the so called Photovoltaic detectors, an external potential difference is applied to the crystal, which causes a migration of the two types of carriers, according to the Coulombian attraction law. The potential difference can be created either by the build-in potential of a p-n junction (e.g. Photodiode or Phototransistor)

or simply by voltage biasing. This flux of charge carriers is called the intrinsic conduction current, whose density can be expressed as:

$$J = J_e + J_h = (n_e\mu_e + n_h\mu_h)qE = \sigma E \tag{7.2}$$

where the indices e and h denote the quantities which refer to electrons and holes respectively; n is the total concentration of charge carriers which is the sum of the initial thermal-equilibrium and generated excess concentrations ($n_0 + \delta n$). μ is the charge carrier's mobility defined as the quotient of the absolute value of the carrier speed and the electric field amplitude ($\mu = |v|/|E|$). σ is defined as the crystal conductivity.

The change in conductivity can itself also be used as the measurement principle. These detectors are then, non surprisingly, called Photoconductive detectors. The main difference with the photoconductive devices compared to for example the photodiode is that the charge carriers will eventually recombine.

The last type of detector utilizing the intrinsic photoelectric effect is the charge transfer device. Here the charge is stored in a potential well of a metal-insulator-semiconductor capacitor, before transferring the charge across the semiconductor substrate towards the read-out electronics.

As is said, the amount of charge carriers is not only dependent on the amount of incident photons, but on the total amount of absorbed energy, including that of heat. It can be shown that:

$$n_i = \sqrt{n_e n_h} = \sqrt{N_c N_v}\exp\frac{-E_g}{2kT} \tag{7.3}$$

where N_c and N_v denote the density of available energy levels in the conduction and valence bands respectively; E_g is the width of the bandgap. At the same time, the mobility will decrease by a factor $1/T$, because the thermal agitation will have moving charges collide with the lattice. Combining these relationships it shows that the conductivity will increase with temperature.

At this particular moment two types of intrinsic photodetectors are dominating the scene, which is why they will be treated separately, but briefly.

Figure 7.4: Mercury Cadmium Tellurium detector. (At the courtesy of Daylight Solutions).

7.2.2.1 Mercury Cadmium Tellurium (HgCdTe, MCT)

By far the most wide spread intrinsic photodetector is based on a compound of Mercury, Cadmium and Tellurium. The bandgap of MCT carries as a function of its composition from HgTe, which is a semimetal with a negative band gap, to CdTe with a band gap of 1.6eV. At a mercury composition of 80%, the band gap attains a value of 0.1eV, sufficient for detection of IR radiation up to 12μm [84]. HgCdTe has, however, serious technological problems in mass production, which result from a weak Hg-Te bond. Other basic problems are: health hazard due to the highly toxic compounds, high mercury vapour pressure over melts, the Hg-Cd-Te phase diagram shape resulting in serious difficulties in repeatable growth of uniform-composition bulk crystals and epitaxial layers [83]. These problems manifest themselves mostly in the compounds designed for the far infrared band, because of the high mercury concentration. In the mid infrared band these problems are less dramatic, making MCT the workhorse in this region. Compared to other photodetectors for example it has a high optical absorption coefficient, a high quantum efficiency

and a relatively low thermal generation rate, making it possible to operate it at somewhat higher temperatures. Still it will not be able to work properly in room temperature conditions though.

7.2.2.2 Indium Antimony (InSb)

Another compound that is fairly often used in intrinsic photodetectors is Indium Antimony. Although it does not suffer from the material uniformity problems which trouble MCT at higher wavelengths, it requires even more cooling for mid-IR operation. In part because the band gap decreases with increasing temperature, which exacerbates the enhanced thermal generation always associated with temperature elevation. It also takes the device operating cut-off wavelength above 5μm, which might result in the requirement of an extra filter, and requires systems that can cope with the temperature dependent response. [84]

7.2.3 Extrinsic Photoelectric effect

The extrinsic photoelectric effect is very similar to the intrinsic photoelectric effect. The only difference is the origin of the charge carriers. By doping a pure crystalline material with atoms that either have an excess or deficient covalent bond, intermediate levels appear within the bandgap which facilitate the formation of charge carriers. By definition these will be majority carriers. If we consider an n-type semiconductor, then, from charge neutrality, we can assume that $\delta n = \delta p \equiv \delta p$. [21] Now if we use δp as the concentration of excess carriers we can describe the change in conductivity due to the optical excitement of an extrinsic semiconductor as

$$\Delta\sigma = q(\delta p)(\mu_e + \mu_h) \tag{7.4}$$

The biggest downside of extrinsic photodetectors is that they usually have a very high thermal generation rate, requiring extensive cooling to have a proper signal.

7.2.4 Intersubband transition (ISBT)

The term intersubband transition refers to the electronic transition between the confined states in quantum wells or between two minibands in a superlattice structure. Both can be seen as a thin semiconductor layer (of the order of 100 Å) embedded in a semiconductor with a larger bandgap (see also figure 7.2. The energy levels, and therefore the spectral response, can be tuned by material choice, induced strain, thickness and in some cases the bias voltage. Depending on the structure used, ISBT photodetectors can have minority or majority charge carriers. Currently research is focused on three different types of ISBT infrared photodetectors. First there is the Type II Superlattice Infrared Photodetector (T2SLIP), first proposed by Smith and Mailhiot [87] in 1987. Around the same time, the first Quantum Well Infrared Photodetector (QWIP) was demonstrated by Levine [88]. More recently, also the Quantum Dot Infrared Photodetctor (QDIP) came into existence. All will be discussed briefly.

7.2.4.1 Superlattice Infrared Photodetectors (SLIPs)

In a superlattice, adjacent wells are separated by thin barriers. This will form minibands in the superlattice region by the coupling of electron wavefunctions. The superlattice miniband structures are divided into three different types, called type I, type II and type III. For the type I heterostructures the bottom of the conduction subband and the top of the valence subband are formed in the same semiconductor layer. In the type II the conduction and valence subbands

are staggered in both real and reciprocal space, so that electrons and holes are confined in different layers. Type III superlattice involves semimetal material. One example is HgTe/CdTe superlattice. Although the bottom of the conduction subband and the top of the valence subband are formed in the same semiconductor layer in Type III superlattice, like Type I superlattices, the bandgap of Type III superlattices can be continuously adjusted from semiconductor to zero band gap material and to semimetal with negative band gap.

Several different configurations and geometries can be found [89, 90]. Strained type II SLIPs are by far the most researched SLIPs today. Their advantage should be in the stack of thin layers. For one, it gives the opportunity for proper bandgap engineering. Second, it results in a low operational bias. The electrons in the miniband of the superlattice (SL) are conductive, where those in quantum states of multiple quantum wells are confined. The SL hence becomes a low resistance structure and thus no externally applied bias drops on the SL under low bias range. Therefore, a current blocking layer is needed to decrease the dark current in SLIPs. However this layer can also directly be used as an absorption wavelength tuner. Third, Auger scattering rates can be reduced compared to HgCdTe photodetectors, which may lead to increased operating temperature. Finally, the stack of thin layers also has good optical absorption properties and has a fairly broad spectral response compared to its quantum well competitors. [91]

Although this all sounds quite promising, at the moment of writing, reports of room temperature operated T2SLIPs could not be found. The technology is clearly still in its infancy, and is expected to be further developed in the future.

7.2.4.2 Quantum Well Infrared Photodetectors (QWIPs)

Unlike the wells in a superlattice, the wells in QWIPs are sandwiched by thick barriers in the multiple quantum well structure. Therefore electron wavefunctions in the wells would not interact with each other and discrete quantum states are formed. Depending on the relative band offsets of the two semiconductor materials, both electrons and holes can be confined in one direction in the conduction band and the valence band, respectively, and one obtains allowed energy levels that are quantized along the growth direction.

The development of QWIPs has been mostly restricted to AlGaAs/GaAs based detectors, since GaAs has mature material and processing technologies. With the mature technology it was anticipated that the cost of an imaging device based on QWIPs would be substantially less than that based on HgCdTe or InSb detectors, and that a large volume production capability could be easily established. The second advantage would be the flexibility of the QWIP approach for enhanced device functionality and for its ease to integrate with other devices (e.g. LEDs), as reported in [92]. 10 years later though GaAs QWIPs seem to be at their maximum potential and are still not able to really compete with these almost classic devices [93].

One of the biggest issues with QWIPs in general is the infamous polarization selection rule for intersubband transitions. By using Fermi's golden rule, an expression can be derived for the intersubband absorption coefficient [94]. The result shows that the electric field of the radiation must have a component perpendicular to the semiconductor layers to couple to the intersubband transition, making it impossible to have normal-incidence radiation. This of course, has consequences for the practicality of these devices. Several geometries have been developed to try and comply with this rule by using the Brewster angle, a 45° bevel or nonplanar structures.

Still convinced about the potential of QWIPs, scientists came up with several possibilities that could overcome the selection rule. For example, p-type valance-band QWIPs have been sought after and demonstrated, where the strong mixing between the different hole bands plays the critical role to get round this issue [95–97]. Normal-incidence infrared detectors based on an indirect bandgap semiconductor quantum well system such as Si/SiGe have also been suggested

and demonstrated. [98–101]

Nevertheless, the search for n-type (i.e. conduction-band) QWIPs is continued, because of its superior transport and confinement properties compared to the p-type counterpart. Specifically, this is because for most common semiconductor QWs, the conduction-band offset ΔE_c is larger than the valance-band offset ΔE_v, providing stronger quantum confinement in the conduction-band QW, thereby larger subband separations. Furthermore, the smaller electron effective mass and the higher mobility μ_e typical of the conduction-band are also highly desirable to the detector's sensitivity and speed. Reports have been made for example that high doping could theoretically lead to a large intersubband transition absorption in conduction-band QWIPs [102]. In a more recent report [103], Sherliker shows the development of QWIPs based on AlGaN/GaN operating at room temperature in the 3-5 μm band with a detectivity of $\sim 5 \cdot 10^6$ cm $Hz^{1/2}$ W^{-1}, where the incident radiation was normal to the detector. The exact mechanism at play here is not yet fully understood according to the author.

7.2.4.3 Quantum Dot Infrared Photodetectors (QDIPs)

Although the success of quantum well structures for infrared detection applications has so far been somewhat limited, it has stimulated the development of quantum dot infrared photodetectors (QDIPs). In the past decade, the QDIPs have become a topic of extensive research. At present, nearly defect-free quantum dot devices can be fabricated reliably and reproducibly.

In general, QDIPs are similar to QWIPs, but with the quantum wells replaced by quantum dots, which have size confinement in all spatial directions, whereas quantum wells only have a confinement in the growth direction. The quantum-mechanical nature of QDIPs leads to several differences/advantages over QWIPs and other available types of IR photodetectors. As in the HgCdTe, SLIP and QWIP technologies, QDIPs provide multi-wavelength detection. However, where the other technologies have a fairly broad and featureless absorbance spectrum, QDIPs have more profound individual absorption peaks corresponding to excitonic states in the QDs [104]. Furthermore, QDs provide many additional parameters for tuning the energy spacing between energy levels, such as QD size and shape, strain, and material composition. The potential advantages in using QDIPs over quantum wells are as follows [105, 106]:

- Intersubband absorption may be allowed at normal incidence (for n-type material). The selection rules in QDIPs are inherently different, and normal incidence absorption is observed.
- Thermal generation of electrons is significantly reduced due to the energy quantization in all three dimensions. Generation by longitudinal optical (LO) phonons is prohibited unless the gap between the discrete energy levels equals exactly to that of the phonon. This prohibition does not apply to quantum wells, since the levels are quantized only in the growth direction and a continuum exists in the other two directions. This QD phonon bottleneck will increase the relaxation time from photo-excited electrons, compared to that of QWs which is in the order of a few picoseconds. Thus, it is expected that the Signal-to-Noise ratio in QDIPs will be significantly larger than that of QWIPs.
- Lower dark and noise currents of QDIPs is expected than of HgCdTe detectors and QWIPs due to 3-D quantum confinement of the electron wavefuntion.

Both the increased electron lifetime and the reduced dark current indicate that QDIPs should be able to provide high temperature operation. In practice, however, it has been a challenge to meet all of the expectations above. For now the main difficulty seems to be in the large

inhomogeneous linewidth of the quantum-dot ensemble when using the very popular Stranski-Krastanow (S-K) growth method [107]. As a result, the absorption coefficient is reduced, reducing QDIP performance. Subsequently, the quantum efficiency of QD devices tend to be lower than what is predicted theoretically.

Several attempts have been made to try and reduce the inhomogeneous linewidth. Vertical coupling of quantum-dot layers might do the trick, but may also increase the dark current of the device, since carriers can tunnel through adjacent dot layers more easily. Completely different geometries are also reported by Ting, *et al.* [90] (Submonolayer quantum dots) and Stiff-Roberts [104] (Colloidal quantum dots). Most research currently performed is focusing on operating temperatures up to a maximum of 200 K. Nonetheless, reports of more traditional QDs in room temperature operation are also found with quite impressive numbers. Lim, *et al.* [106] for example, reports a QDIP device based on the S-K growth method with a detectivity of $6 \cdot 10^7$ cm $Hz^{1/2}$ W^{-1} at room temperature with normal incidence radiation and a peak in the spectral response at 4.1 μm

7.3 Thermal detectors

Thermal infrared detectors are so called tandem transducers. First the infrared light is absorbed and turned into an increase in the materials temperature. This resultant change in temperature is then transformed into an electrical signal by one of several effects. Those that are considered to be the most promising for this particular application will be discussed below. Since the signal does not depend upon the photonic nature of the incident radiation, thermal effects are generally wavelength independent; the signal depends upon the radiant power (or its rate of change) but not upon its spectral content. This does not mean though that thermal detectors are by definition wavelength independent. In fact, in most instances, the thermal detector is dependent on wavelength because of the mechanism responsible for the absorption of the radiation which is often wavelength dependent. They will however have a much broader characteristic compared to photodetectors and their characteristic can often be tailor made by a proper absorber design, making them perfect as spectrometer detectors. Also in contrast to photodetectors, thermal detectors typically do operate at room temperature. Further, they are usually characterized by modest sensitivity and slow response (because heating and cooling of a detector element is a relatively slow process), but cheap and easy to use.

7.3.1 Thermoelectric power (Thermocouples)

Traditionally, the thermoelectric effect encompasses three different effects: The Seebeck effect, the Peltier effect and the Thomson effect. Strictly speaking it is the generation of a potential difference between two junctions of a material which are at different temperatures (i.e. Seebeck effect) or vice-versa (i.e. Peltier effect). The Thomson effect describes the heating or cooling of a current-carrying conductor with a temperature gradient. Only the Seebeck effect will be further discussed.

Thermocouples are devices that work on the Seebeck principle. By coupling two materials, where the junction of the two materials is at an elevated temperature compared to the other ends, a voltage, V_{TP} is generated according to:

$$V_{TP} = (\alpha_1 - \alpha_2)\Delta T \tag{7.5}$$

where α_n is the Seebeck coefficient of material n, and ΔT is the temperature difference. Obviously, the difference in Seebeck coefficients of the two materials should be maximized together

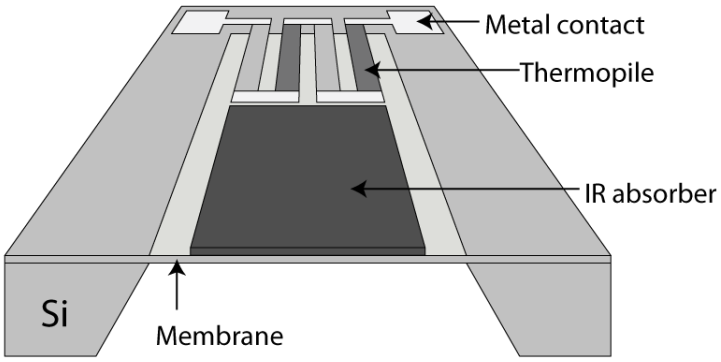

Figure 7.5: Exmample of a thermopile MEMS thermal infrared detector.

with the largest possible difference in temperature to get the highest output. There is another approach as well though. When one sees the thermocouple as a simple voltage source, one can imagine that putting N of these sources in series will also increase the output by a factor N, given that the temperature difference will not change.

The fact that its output is dependent on the relative temperature instead of an absolute temperature is in this particular case seen as an advantage, since we're merely interested in the temperature increase as caused by the incident radiation. Any slow ambient temperature variations are inherently compensated. Also thermopiles can be readily fabricated in most IC-compatible processes, depending on the materials used. The separation of the absorber and temperature measurement is a benefit in terms of IC compatibility as well.

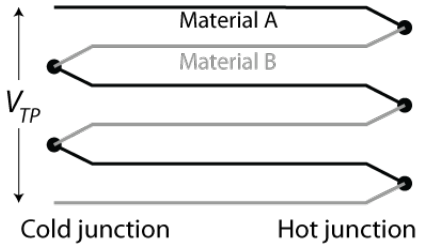

Figure 7.6: A thermopile composed of three thermocouples.

Many different configurations (e.g. used materials and geometries) of thermocouples and thermopiles can be found, very much depending on their application. If we look at those that have similar requirements to those presented in section 3.2 a normalized detectivity of about $1 \cdot 10^7$ to $1 \cdot 10^8$ cm $Hz^{1/2}$ W^{-1} can be found. [108–112]

7.3.2 Thermoresistance (Bolometers)

Bolometers can most easily be seen as temperature sensitive resistors. Traditionally, Vanadium Oxide (VO_x) [113–115] or Yttrium Barium Copper Oxide (YBaCuO) [116–118] based materials are most commonly used for high sensitivity bolometers, because of their very high temperature coefficient of resistance (TCR); α = 2-3% K^{-1} and α = 3-3.5% K^{-1} respectively. For both materials, the normalized detectivity will be in the order of 10^8 cm $Hz^{1/2}$ W^{-1}, approaching the detectivity of cooled photodetectors. However, these detectors are mainly developed for military application, and their costs are not as low as the required level for many commercial applications including this one, because of very limited CMOS compatibility, if compatible at all.

More compatible options are available as well though. The most interesting is probably the p-n diode, due to its excellent stability and low noise. Diodes as temperature sensors can

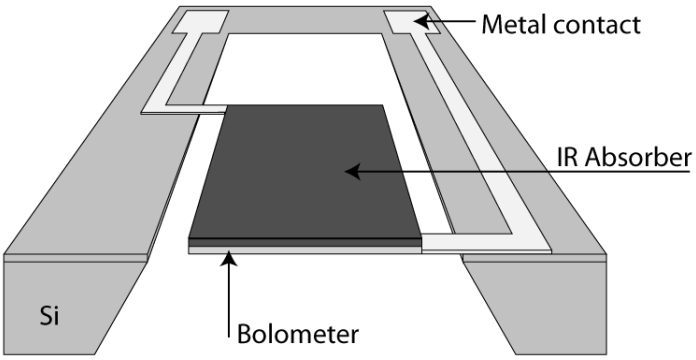

Figure 7.7: Example of a bolometer MEMS thermal infrared detector.

operate in various modes, such as constant current or constant voltage either forward or reversed biased. As with all thermal detectors, competitive detectivity can only be reached with proper thermal isolation of the absorber to the substrate. Several research groups have reported their way of solving this problem either by electrochemical (EC) etch stop technique [119], by utilizing silicon-on-insulator (SOI) wafers [120] or sacrificial etching [121]. Detectivities of $D^* = 9.7 \cdot 10^8$ cm $Hz^{1/2}$ W^{-1} have been reported [119].

The major disadvantage of using a diode is that its current as well as the sensitivity depends exponentially on the absolute temperature. For accurate measurements this requires stabilizing the substrate temperature in the μK range or including several reference temperature sensors on the substrate. Another property which should be carefully looked at is self-heating.

7.3.3 Pyroelectricity (Pyroelectric detectors)

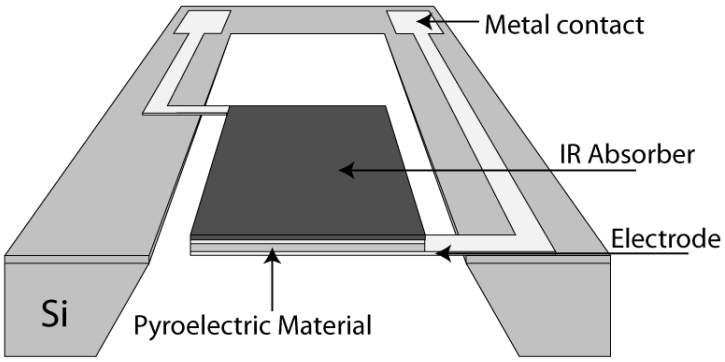

Figure 7.8: Example of a pyroelectric MEMS thermal infrared detector.

The pyroelectric effect is the change in the polarization of the electrical dipole moments in a polar dielectric due to a change in its temperature. The detector is made by placing the crystal inside a capacitor such that the two electrodes are perpendicular to the polarization axis. The variation in the polarization causes a modification of the electric charge at the surface of

the crystal. By connecting a resistor in parallel, a current will flow to restore the electrical equilibrium, resulting in a measurable potential across the resistor.

The variation in the polarization of the crystal is represented by the *pyroelectric coefficient* $\mathcal{P}$ [C K^{-1}] such that [85]:

$$dq = \mathcal{P} dT \tag{7.6}$$

where dq is the quantity of charge displaced. The resulting specific detectivity is dependent on both the shape of the incident flux signal and the type of read-out used, but reports can be found of detectivities in the order of 10^9 cm $Hz^{1/2}$ W^{-1} [122].

Pyroelectric detectors unfortunately have quite a few difficulties as well. Note for example that pyroelectric devices only detect the change of any input energy flux, instead of an absolute value, which is why pyroelectric detectors by definition need a modulated source. More difficult is the issue with the IC process compatibility. Most materials, for example, have to be deposited as a last step in the process, because they cannot withstand the temperatures of the other process steps. Others would contaminate the machinery and are therefore not compatible at all. Moreover, all pyroelectric materials are also piezoelectric, making them sensitive not only to temperature change, but also to changes in the strain of the material. Other design challenges include the matching of the material properties and size of the detector to the read-out circuit used.

Several research groups have been looking for more IC compatible materials, which still have properties that are good enough for infrared spectroscopy [123, 124]. Tang [123] for example reports the design of a pyroelectric detector using $0.74Pb(Mg_{1/3}Nb_{2/3})O_3$-$0.26PbTiO_3$ (PMN-0.26PT), which can be deposited by magnetron sputtering at 70° C and result in a device with a normalized detectivity of $\sim 10^8$ cm $Hz^{1/2}$ W^{-1}. However, it does require thinning and polishing, and although quite readily available, will not be a standard material in many IC labs.

7.3.4 Thermo-mechanical effects (bimetallic devices)

In opto-mechanical thermal detectors, yet another domain is added to the sensor's transduction process. The induced temperature increase by the incident radiation, causes a deflection of the element due to differences in thermal expansion. This deflection can be measured in many ways, including strain gauges, capacitance change, optical deflection, magnetic change, etc. [82,125,126] However, the increased complexity of another transduction is not compensated by any other property like an increased detectivity.

7.3.5 Vacuum packaging

As has become clear now, it is very important for thermal detectors to have the highest possible increase in temperature for a certain amount of incident power. As a result, it becomes paramount to reduce any heat loss to an absolute minimum. Since heat may conduct through any surrounding gas, the thermal detectors will have the highest detectivity in low pressure environments. Vacuum packaging is therefore considered an essential part of thermal detectors. Several options to retain a vacuum around a sensor have been developed over the years, but finding the right one for this application is not as straight forward as one might think. Obviously it should have a good hermetic sealing and it should be easy to integrate with the rest of the process, but the loss in optical performance should also be kept to a minimum.

Packages are identified as first-level, when the packaging occurs after the wafers are diced in chips and as zero-level when the packaging is done before the dicing. The latter is also referred

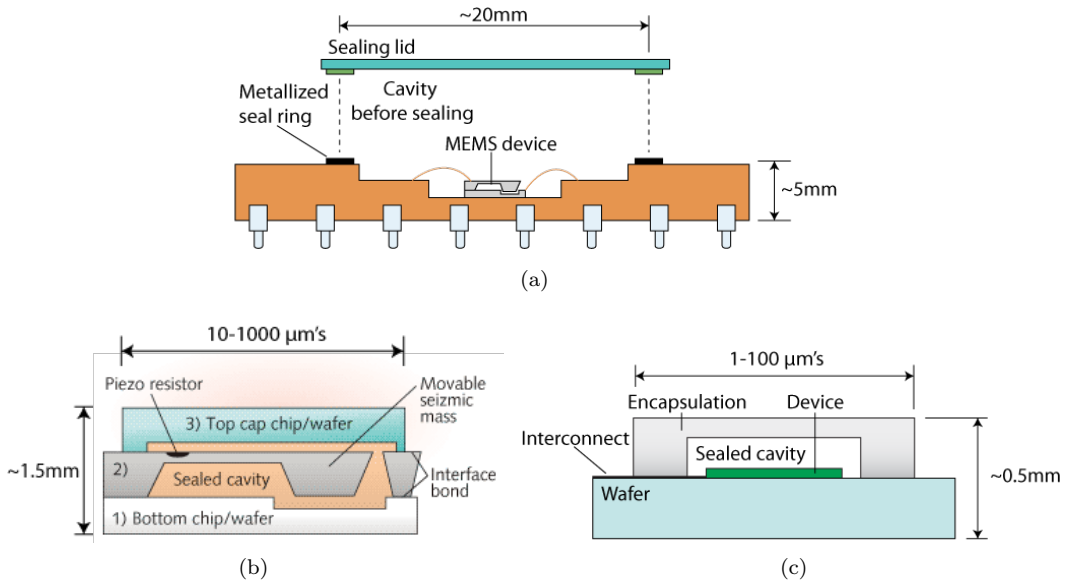

Figure 7.9: Three options for vacuum packaging with a) traditional (first-level) vacuum packaging*, b) wafer bonding (zero-level) vacuum packaging* and c) thin-film encapsulation. *At the courtesy of www.electroiq.com

to as wafer level packaging.

Several options may be distinguished as shown in figure 7.9:

1. Traditional component level vacuum packaging (i.e. first-level packaging)
2. Wafer bonding (i.e. zero-level packaging)
3. Thin-film encapsulation (i.e. zero-level packaging)

Every chip will finally require a connection to the outside world. Many different packages have been developed for this purpose. When some chips required a vacuum environment, it was obvious to try and use packages that were already available. One such option is the metal TO-transistor cap as shown in figure 7.10, which can have an optical filter mounted.

Figure 7.10: Hermetically sealed Transistor Outline (TO) Package with optical filter. (At the courtesy of Laser2000).

This type of packaging has some serious issues for this application. First and foremost, the whole idea of the system is to be able to integrate all the different sensors on the same chip, some of which need to be in direct contact with the gas. Having the whole chip packaged in vacuum is therefore no option, nor is a separate package with for example just a detector and source inside. Moreover, reports have been made that using these packages it is difficult to maintain a long-term vacuum. [127]

Wafer bonding is the stacking of several wafers to create the cavities in which the device will operate. It seems quite a good option, but will often lead to having a thick layer of silicon in the optical path, which, as can be seen in figure 6.17, will at best only transmit just over 50% of the

light if no anti-reflection coating is applied. Several methods for wafer bonding were developed. The wide variety of hermetic wafer bonding techniques include anodic bonding, silicon-silicon direct (fusion) bonding, glass frit bonding, adhesive bonding, ultrasonic bonding and metal based bonding that includes thermo-compression bonding [127,128]. Many of these have difficulties like the need for extremely low surface roughness (as for example introduced by connecting leads), IC process incompatibility due to materials used and/or temperatures involved, and no long-term preservation of vacuum.

In the thin-film approach, as for example reported by Santagata [129], the unreleased MEMS device is covered with an additional (patterned) sacrificial layer before the encapsulation material is deposited. By removing the sacrificial layer through etch holes in the encapsulation layer, the device is released and covered by a free standing membrane, as can be seen in figure 7.11. To prevent out-gassing of the remaining sacrificial material, a layer of dense material (e.g. LPCVD SiN) is deposited over the complete structure up to the point where either the etch holes are closed or the layer is considered thick enough. If the etch holes are not sealed yet, this may be done by metal sputtering. Any metal not covering the etch holes is obviously removed.

Compared with wafer bonding, thin-film encapsulation has several advantages that render it a much simpler technology, and therefore also more cost effective at the same performances [129]:

1. No need for the second substrate
2. It employs thin-film batch fabrication processes, avoiding the need for aligning two wafers and the challenges of bonding on processed (i.e., not smooth) surfaces.
3. It produces much lower topography, allowing for post-encapsulation processes for additional MEMS or IC steps.

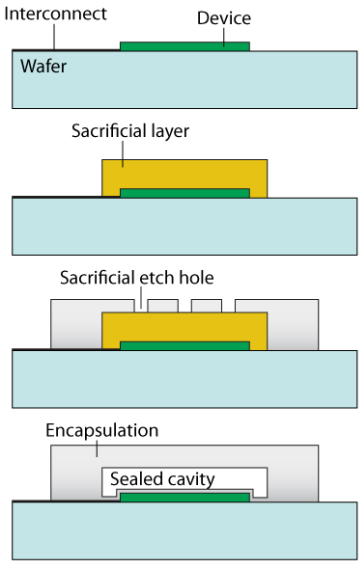

Figure 7.11: Schematic flow diagram of the fabrication of a thin-film encapsulation vacuum package.

Compared to the traditional packages, the thin-film encapsulation process allows for a much more compact design. It, for example, allows the die to be separated with dicing cuts that are within 10s of microns of the MEMS device. This reduction in device area enables devices to be fabricated at very high density in the MEMS process, reducing the cost per die. This cost reduction can overcome the added cost of the encapsulation steps, depending on the details of the process and the device design.

As is for all packaging processes, the required temperatures for the thin-film encapsulation processes play an important role in the design of the MEMS device. The kind of deposition process to be used for the MEMS encapsulation, and the choice of the sacrificial layer, are strictly linked to the thermal budget of the MEMS device itself. If we would like to keep the process CMOS compatible, the process temperatures should not be above 400 °C.

At this moment, there is no thin-film encapsulation process available which will give a good vacuum, whilst still only requiring CMOS compatible temperatures. A good vacuum is possible with a process that includes Low Pressure Chemical Vapor Deposition (LPCVD) SiN, but this is deposited at 850°C.

7.4 Concept choice

Parameter	Photodetector	Thermal detector
Sensitivity	High	Low
Detectivity	Low (Uncooled)	Moderate
Spectral response	Selective	Wide and flat
Response time	Fast	Slow
Cost	High	Low
Self-test	Impossible	Easy
Integration	Difficult	Easy

Table 7.1: Comparison of mid-infrared photo- and thermal detectors

Photodetectors might have an unsurpassable detectivity up to the near infrared, but in the mid-infrared, the photon energies are so low, that uncooled detection in this region is still dominated by thermal detectors. Progress is being made here though with the development of the Quantum Dot Infrared Photodetectors, but this technique is still very much in its infancy and, as with Quantum Well Infrared Photodetectors, it is to be seen if they will ever meet the expectations.

The requirements stated for this particular application simply exclude the use of cooling devices because of cost, weight, size and power limitations. On top of that, photodetectors lack a wide spectral response (which in this case is considered a disadvantage), an easy self-test and reliable long-term continuous operation. Another advantage of the thermal detectors is the separation of the absorption of the infrared light and the transduction from heat to an electrical signal, which gives us the ability to optimize the two separately. Therefore, thermal detectors are chosen as the way forward at this particular point and no more effort is put into discussing photodetectors.

Although it is less clear between the thermal detectors which is best suitable for the purpose of infrared spectroscopy, both the thermo-mechanical and pyroelectric devices will not be further considered as well. For the thermo-mechanical devices this stems from the fact that the complexity and fragility are not considered to be compensated by a higher detectivity or other performance parameter. The pyroelectric detector will not be further considered because of its difficult compatibility with IC processes. To decide between thermoelectric devices and bolometers there will have to be done some more research into their fundamental limits, advantages and disadvantages.

The main advantage of bolometers over thermopile detectors is the greater possible detectivity. However, using a thermopile detector gives us many other advantages: It measures the temperature difference (which is what we want to know in this case), has a linear response, its signal is self-generated and therefore requires less power, is less susceptible to self-heating, and like the earlier discussed LVOF, there is a lot of knowledge present within our research group. Table 7.3 summarizes the differences between bolometers and thermopile detectors.

Except for the type of detector, we also have to decide which type of absorber and vacuum package should be used. Although one can find reports based on other than the thin-film absorber, this type is still dominating the scene. Other options include meta materials and carbon nanotubes, but these techniques are still very much in development. For a discussion on the different types of absorbers, the reader is referred to [131].

Looking at the vacuum packages the thin-film encapsulation approach is identified as the

Parameter	**Eminoglu** [119, 130]	**Ahn** [113]	**Calaza** [108]	**Roncaglia** [112]	**Wu** [131]
Detector type	Bolometer	Bolometer	Thermopile	Thermopile	Thermopile
Detectivity [cm $Hz^{1/2}$ W^{-1}]	$9.7{\cdot}10^8$	$1.98{\cdot}10^{9}$*	$1.05{\cdot}10^7$	$1.32{\cdot}10^7$	$1.31{\cdot}10^8$
DC Responsivity [V/W]	4970	7760	15	84.7	294.7
Sensitivity	-2mV/K	2.7%/K	143μV/K	-	290μV/K
Operating pressure [mTorr]	80	3	$760{\cdot}10^3$	-	750
Material	p^+n diode	V-W-O	polySi-Al	p-n polySi	p-n polySi
CMOS compatible	yes	no	yes	yes	yes
Impedance @ T=298K [kΩ]	-	21.7	40.1	-	-
Absorber type	Thin-Film	Thin-Film	Thin-Film	Thin-Film	Thin-Film
Mean absorption [%]	45	80	56	-	80
Detection band [μm]	8-12	-	8-14	3-5	1-4
Releasing process	FS Bulk MM	Surface MM	FS Bulk MM	FS Bulk MM	Surface MM

Table 7.2: Comparison of reported bolometer and thermopile infrared detector properties. *Calculated

Parameter	**Bolometer**	**Thermopile**
Detectivity	+	0
IC compatibility	+	++
Measurement	Absolute	Relative
Response	Material dependent	Linear
Required electrical power	High	Very low
Self-heating	Very susceptible	almost impervious
Knowledge present	+	++

Table 7.3: Comparison of bolometer and thermopile infrared detectors.

most suitable option for this application. Although not CMOS compatible, there is still chosen to continue with the high temperature thin-film encapsulation. The technique used is still in its infancy and may be developed later to the extend where low temperature and good vacuum performance are united in a single process. However, we would still like to have a CMOS compatible process as well. Therefore there has been chosen for a separate process next to this high temperature process. The devices developed with this process will thus not be encapsulated, but this is not a big deal, since all the measurements can be done in a vacuum chamber. From now on these processes will be referred to as the high and low temperature processes.

The final decision is thus to continue with two designs. Both will be based on a thermopile detector with thin-film absorber, but one will have a self sustained vacuum by means of a thin-film encapsulation, whereas the other will not have a self sustained vacuum. This decision has a lot to do with the risks involved. It is very important to end up with an operative device to be able to answer the research questions stated at the beginning. The risk of a failing device is already quite big by just trying to integrate the different parts.

Still, bolometers and wafer bonding are considered very interesting as well and might be a good topic for further research later.

7.5 Theory

7.5.1 Thin-film absorbers

In the ideal case, any incident infrared light on the detector structure is absorbed, maximizing its detectivity. Therefore, we have to make sure that both transmission and reflection are negligible.

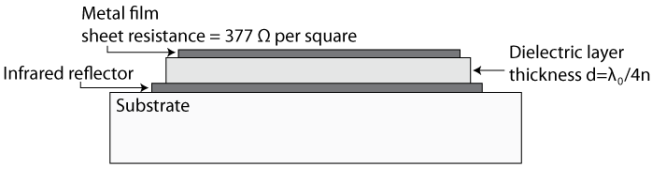

Figure 7.12: Schematic drawing of a three layer thin-film absorber stack.

One option to obtain high absorption is a three layer (e.g. metal-dielectric-metal) thin-film structure as shown in figure 7.12. Other options like Carbon Nano Tubes (CNT) or meta-materials might possibly show even higher performances, but are still under investigation by our research group [131].

The thin-film absorber structure is again based on interference, just as the optical filters discussed in chapter 6. This time though, we would like to utilize destructive interference only, such that all the light in the region of interest is absorbed. This is facilitated by having a dielectric layer with thickness:

$$d = \lambda_0/4nd \tag{7.7}$$

where λ_0 is the center wavelength and n is the refractive index of the material.

Before any interference is happening though, we will need to make sure the light is actually 'entering' the stack. In an attempt to minimize the reflection from the surface it is useful to consider the physical equations that represent the reflection process. The first equation of interest is that describing the reflection coefficient at an interface:

$$r = \frac{\eta_M - \eta_0}{\eta_M + \eta_0} = \frac{Z_M - Z_0}{Z_M + Z_0} = \frac{\frac{Z_M}{Z_0} - 1}{\frac{Z_M}{Z_0} + 1} \tag{7.8}$$

where r is the reflection coefficient and η is the admittance of the propagating medium. The subscript 0 indicates the incident medium (usually air) and M the surface material. The admittance in this equation can be replaced with the intrinsic impedance ($Z = 1/\eta$). The reflection coefficient falls to zero when $\eta_M = \eta_0$, or when $\frac{Z_M}{Z_0} = 1$. In other words, the material in the layer is impedance matched to the incident medium.

Impedance matching can be done in two ways: Intrinsic impedance matching or matching of the electric permittivity and the magnetic permeability. The intrinsic impedance of free space is effectively given by:

$$Z_0 = \frac{\mathbf{E}}{\mathbf{H}} = \sqrt{\frac{\mu_0}{\varepsilon_0}} \approx 377\Omega \tag{7.9}$$

where $\mathbf{E}$ and $\mathbf{H}$ are the electric and magnetic field vectors and μ_0 and ε_0 are the permeability and permittivity of free space, respectively. Thus a material with an impedance of 377 Ω will not reflect if the incident medium is free space.

As said, perfect impedance matching can also be realized if the electric permittivity and the magnetic permeability are equal.

$$\frac{Z_M}{Z_0} = \sqrt{\frac{\mu_r^*}{\varepsilon_r^*}} = 1 \tag{7.10a}$$

$$\text{With: } \varepsilon_r^* = \frac{\varepsilon' - i\varepsilon''}{\varepsilon_0} \tag{7.10b}$$

$$\mu_r^* = \frac{\mu' - i\mu''}{\mu_0} \tag{7.10c}$$

the prime and double prime superscripts represent the real and imaginary components of the complex numbers, respectively. If the incident medium is free space, it follows that $\mu_r^* = \varepsilon_r^*$. The implication is if both the real and imaginary parts of the permittivity and permeability are equal, then the reflectivity is zero.

The general equation for the absorption, A, as a function of wavelength, λ, for the 3-layer structure shown in figure 7.12, is given by [132]:

$$A(\lambda) = \frac{4}{Dn^2}\left\{\left[\frac{f_s(f_r+1)^2}{n^2} + f_r\right]\sin^2\theta + (f_r+f_s)\cos^2\theta\right\} \tag{7.11a}$$

$$\text{With: } D = \left[\frac{(f_r+1)(f_s+1)}{n^2} + 1\right]^2 \sin^2\theta + \left[\frac{f_r+f_s+2}{n^2}\right]\cos^2\theta \tag{7.11b}$$

$$f_r = 120\pi/R_r \tag{7.11c}$$

$$f_s = 120\pi/R_s \tag{7.11d}$$

$$\theta = 2\pi nd/\lambda \tag{7.11e}$$

R_r is the sheet resistance of the rear surface metal film, R_s is the sheet resistance of the front surface metal film (onto which the radiation is incident), d is the thickness of the central dielectric layer and n its refractive index. The dielectric layer is assumed to be non-absorbing, which is valid for many dielectric materials and low conductivity semiconductors of interest.

An alternative method to simulate and design thin-film stacks is to use commercially available software like Essential Macleod 8.14.159(ie) [133]. It offers more freedom to simulate the result in the case of more complex structures and is able to do automatic optimization of structures. Further studies have therefore been done with this software.

7.5.2 Heat transfer theory

Thermal detectors require proper isolation from any heat sink, to have the incident radiation heat up the detector as much as possible, increasing its responsivity. To be able to make any predictions on the responsivity, it is therefore important to be able to do a thermal analysis. With this analysis, it is possible to determine the temperature field in a medium, resulting from conditions imposed on its boundaries and the properties of the materials involved. That is, we wish to know the temperature distribution, which represents how temperature varies with position in the medium, to optimize the design and maximize the detector's responsivity.

The first law of thermodynamics, more gently called the law of conservation of energy, states that, for an instant t, the rate at which thermal and mechanical energy enters a control volume of $\mathrm{d}x{\cdot}\mathrm{d}y{\cdot}\mathrm{d}z$, plus the rate at which thermal energy is generated within the control volume (together called the energy inflow Q), minus the rate at which thermal and mechanical energy leaves the

control volume (i.e. the amount of work done by the system), W, must equal the rate of increase of energy stored within the control volume, ΔU:

$$\Delta U = Q - W \tag{7.12}$$

Applying this to the thermal domain only, the general form of the conservation of energy requirement on a rate basis is [134]:

$$\dot{E}_{in} + \dot{E}_g - \dot{E}_{out} = \dot{E}_{st} \tag{7.13}$$

Where $\dot{E}_{in} = P_{in}$ is the rate at which energy enters the volume, $\dot{E}_g = P_g$ is the rate at which energy is generated, associated with the rate of thermal energy generation (e.g. Joule effect), $\dot{E}_{out} = P_{out}$ is the rate at which energy leaves the volume and $\dot{E}_{st} = \frac{\mathrm{d}E_{st}}{\mathrm{d}t}$ is the rate of change of energy stored within the volume, given by:

$$\dot{E}_{st} = \mathcal{C}\frac{\mathrm{d}(\Delta T)}{\mathrm{d}t} = c_p \rho V \frac{\mathrm{d}(\Delta T)}{\mathrm{d}t} \tag{7.14}$$

where $\mathcal{C}$ [J K^{-1}] is the heat capacity, ΔT [K] is the temperature difference between the infrared absorber and the bulk material, c_p [J kg^{-1} K^{-1}] is the specific heat of the material, ρ [kg m^{-3}] is the density and V [m^3] is the volume.

Before we continue further resolving this equation, let us first review several important material properties. Thereafter we will continue with defining the three fundamental modes of heat transfer: *Conduction*, *Convection* and *Radiation*. These will later be used to derive the energy outflow equation.

7.5.2.1 Material properties

Thermal conductivity [W K^{-1} m^{-1}]

The *thermal conductivity*, κ, of a solid is primarily dependent on temperature and, although at much lesser extend, also on pressure. For a temperature range of up to a few hundred degrees we can represent the temperature dependence of the thermal conductivity of a solid by $\kappa = \kappa_0(1 + b(T - T_{ref}))$, where κ_0 is the thermal conductance at temperature T_{ref} [135]. If anisotropic materials are considered, κ is represented by a second-order tensor. Thermal conductivity should not be confused with *thermal conductance*, $\mathcal{G}$ [W K^{-1}], which is defined as:

$$\mathcal{G} = \frac{\kappa A}{L} \tag{7.15}$$

Where A [m^2] is the surface area of the material normal to the temperature gradient and L [m] is the length of the material in the same direction as the temperature gradient. For a composition of several materials that are stacked on top of each other, an equivalent thermal conductance can be easily calculated by treating them as several parallel connected thermal conductances (analogous to electrical conductances):

$$\mathcal{G}_{eq} = \sum_{i=1}^{N} \mathcal{G}_i = \sum_{i=1}^{N} \frac{\kappa_i A_i}{L_i} \tag{7.16}$$

If we assume that all materials are of equal length, we can rewrite (7.16):

$$\kappa_{eq} = \frac{\mathcal{G}_{eq} L}{A_{total}} \tag{7.17}$$

The thermal conductivity of air between two enclosed plates is a function of pressure, which is approximated in [136] by:

$$\kappa_{air} = \kappa_{air,0} \frac{1}{1 + \frac{7.6 \cdot 10^{-5} T}{Pd}} \tag{7.18}$$

where $\kappa_{air,0} = 0.0284$ W K^{-1} m^{-1}, is the thermal conductivity of air at room temperature and pressure, P is the pressure, d is the distance between the plates and T is the average temperature of the plates.

Specific heat [J kg^{-1} K^{-1}]

The *specific heat* of a substance is a measure of the variation of its stored energy with temperature. From thermodynamics the two important specific heats are [135]:

$$\text{Specific heat at constant volume: } c_v \equiv \left.\frac{\partial u}{\partial T}\right|_v \tag{7.19}$$

$$\text{Specific heat at constant pressure: } c_p \equiv \left.\frac{\partial h}{\partial T}\right|_p \tag{7.20}$$

Here u is the internal energy per unit mass and h is the enthalpy per unit mass. In general, u and h are functions of two variables: temperature and specific volume, and temperature and pressure, respectively. For substances which are incompressible, c_p and c_v are numerically equal. For solids, specific heat data are only weakly dependent upon temperature and even less affected by pressure.

The equivalent specific heat, $c_{p,eq}$, of multicomponent materials nearly perfectly satisfies the Kopp-Neumann rule of additivity:

$$c_{p,eq} = \sum_i c_{p,i} m_i \tag{7.21}$$

where m_i and $c_{p,i}$ are the **mass fraction** and the specific heat of the i-th component, respectively.

Density [kg m^{-3}]

Density, ρ, is defined as the mass per unit volume. As long as the systems are large enough we can assume a homogenous medium by applying statistical averages.

We can equate the equivalent density, ρ_{eq}, of multicomponent materials using:

$$\rho_{eq} = \frac{M_{tot}}{V_{tot}} = \frac{\sum \rho_i V_i}{V_{tot}} = \sum_i \rho_i v_i \tag{7.22}$$

where v_i and ρ_i are the **volume fraction** and the density of the i-th component, respectively.

7.5.2.2 Conduction

Conduction may be viewed as the transfer of energy from the more energetic to the less energetic particles of a substance due to interactions between the particles. Heat conduction takes place through different mechanisms in different media. In a gas it is through random collisions of the molecules. In a liquid it is much the same, although the molecules are more closely spaced and the molecular interactions are stronger and more frequent. Solids will have heat conduction through lattice vibrations (i.e. lattice waves or phonons). Conductors (e.g. metals) will also

have heat conduction due to the translational motion of the free electrons. Typical for heat conduction is that the heat flux is proportional to the temperature gradient.

According to *Fourier's Law*, the *conductive heat flux vector* [W m^{-2}] is proportional to the negative gradient of the temperature and the thermal conductivity of the material through which the heat is flowing:

$$q_{cond} = -\kappa \cdot \nabla T \tag{7.23}$$

The minus sign ensures that heat flows down the temperature gradient. Note that, using Cartesian coordinates, the heat flux vector can also be resolved into its components:

$$q_{cond,x} = -\kappa \frac{\partial T}{\partial x} \qquad q_{cond,y} = -\kappa \frac{\partial T}{\partial y} \qquad q_{cond,z} = -\kappa \frac{\partial T}{\partial z} \tag{7.24}$$

These are referred to as the *local heat flux* [W m^{-2}] and describe the amount of energy that flows through a particular surface per unit time per unit area. To get the power that is lost through this loss mechanism, the local heat flux will have to be multiplied by its corresponding surface. That is that surface through which the heat is flowing normal to the direction of the heat gradient.

As is explained in more detail in [134] (chapter 2.3) equations (7.13) and (7.23) lead to the general *heat diffusion equation*:

$$\frac{\partial}{\partial x}\left(\kappa \frac{\partial T}{\partial x}\right) + \frac{\partial}{\partial y}\left(\kappa \frac{\partial T}{\partial y}\right) + \frac{\partial}{\partial z}\left(\kappa \frac{\partial T}{\partial z}\right) + \dot{q}_s = \rho c_p \frac{\partial T}{\partial t} \tag{7.25}$$

For temperature T as a function of x, y, z and t. Here $\dot{q}_s$ is the *rate of internal energy conversion* ("heat generation/loss") per unit volume. $\dot{q}_s$ is positive if thermal energy is being generated in the material at the expense of some other energy form (e.g. electrical, chemical or radiation); it is negative if thermal energy is being consumed (i.e. extracted from the material). A common instance of a positive $\dot{q}_s$ is for example provided by resistive heating in an electrical conductor (i.e. Joule effect).

In most engineering problems κ can be taken as constant and (7.25) reduces to:

$$\frac{\partial^2 T}{\partial x^2} + \frac{\partial^2 T}{\partial y^2} + \frac{\partial^2 T}{\partial z^2} + \frac{\dot{q}_s}{\kappa} = \nabla^2 T + \frac{\dot{q}_s}{\kappa} = \frac{\rho c_p}{\kappa} \frac{\partial T}{\partial t} \tag{7.26}$$

Special cases of the conduction equation:

1. **Fourier equation** (no internal energy conversion)

$$\frac{\partial^2 T}{\partial x^2} + \frac{\partial^2 T}{\partial y^2} + \frac{\partial^2 T}{\partial z^2} = \nabla^2 T = \frac{\rho c_p}{\kappa} \frac{\partial T}{\partial t} \tag{7.27}$$

2. **Poisson equation** (steady state with internal energy conversion)

$$\frac{\partial^2 T}{\partial x^2} + \frac{\partial^2 T}{\partial y^2} + \frac{\partial^2 T}{\partial z^2} + \frac{\dot{q}_s}{\kappa} = \nabla^2 T + \frac{\dot{q}_s}{\kappa} = 0 \tag{7.28}$$

3. **Laplace equation** (steady state and no internal energy conversion)

$$\frac{\partial^2 T}{\partial x^2} + \frac{\partial^2 T}{\partial y^2} + \frac{\partial^2 T}{\partial z^2} = \nabla^2 T = 0 \tag{7.29}$$

7.5.2.3 Convection

Heat convection, in this particular case, takes place through the heat dissipation from a solid surface to a displacing fluid. We speak of a forced convection when the flow is caused by external means, such as a fan, pump or atmospheric winds. In contrast, free (or natural) convection is induced by density differences, which may be caused by temperature variations in the fluid. It is important to keep in mind that the fundamental energy exchange at a solid-fluid boundary is by conduction, and that this energy is then convected away by the fluid flow.

Since the space within the package of the sensor under consideration is only very small, the air inside, if present at all, will be virtually still. Therefore convection will not be further considered as a mechanism of heat loss.

7.5.2.4 Radiation

Heat transfer by radiation takes place through electromagnetic wave (i.e photon) propagation. Therefore, unlike conduction and convection, radiation does take place in absolute vacuum as well as in a medium. Just like the mechanism of infrared absorption as described in section 5.2, the mechanism of radiation is related to energy released as a result of oscillations or transitions of the many electrons that constitute matter. These oscillations are, in turn, sustained by the internal energy, and therefore the temperature of matter. Hence we associate the emission of thermal radiation with thermally excited conditions within the matter. This also makes that all matter emits radiation. In most solids and liquids, radiation emitted from interior molecules is strongly absorbed by adjoining molecules. Accordingly, radiation that is emitted from a solid or a liquid originates from molecules that are within a distance of approximately 1 μm from the exposed surface. It is for this reason that emission from a solid or a liquid into an adjoining gas or a vacuum is viewed as a surface phenomenon.

Although the directional distribution of surface emission varies according to the nature of the surface, there is a special case, called a diffuse emitter, that provides a reasonable approximation for many surfaces if viewed from within 20° from the normal line [28]. We speak of a *diffuse emitter* (i.e. *Lambertian source*) as a surface for which the radiance is independent of direction, in which case $L_{\lambda,e}(\lambda,\theta,\phi) = L_{\lambda,e}(\lambda)$.

The black body

The ideal surface in the study of radiative heat transfer (i.e. radiometry) is called the *black body*, which is defined as such a diffuse emitter with both a spectral emissivity, ε_λ, and a spatial emissivity, ε_θ of 1. The *emissivity* is the relative ability of the surface to emit energy by means of radiation and is given by a dimensionless quantity, $\varepsilon \leq 1$. The spectral emissivity refers to this ability as a function of wavelength, where the spatial emissivity is the coefficient which defines its dependence on direction. Surfaces with a spatial emissivity of 1 but a spectral emissivity $\varepsilon_\lambda < 1$, are called grey bodies.

The spectral radiance as function of wavelength, $L_{\lambda,bb}(\lambda,T)$ [W m^{-2} sr^{-1} μm^{-1}], of black body emission is well known, having first been determined by Planck. It is of the form:

$$L_{\lambda,bb}(\lambda,T) = \frac{2 \cdot 10^{-6} h c_0^2}{\lambda^5 e^{hc_0/\lambda k T_s} - 1} \tag{7.30}$$

or for grey bodies:

$$L_\lambda(\lambda,T) = \varepsilon_\lambda(\lambda) L_{\lambda,bb}(\lambda,T) \tag{7.31}$$

Where h is Planck's constant ($6.6256 \cdot 10^{-34}$ J s), k_b is Boltzmann's constant ($1.3805 \cdot 10^{-23}$ J K^{-1}) and T [K] is the absolute temperature of the black body.

As already mentioned, in the field of spectroscopy, radiation is usually referred to in units of wavenumber. Rewriting (7.30) to be used with wavenumbers is not as trivial as it might look. First we have to note that by using equation (2.1) we can write [137]:

$$L_{\bar{\nu},bb}(\bar{\nu},T)\,|\mathrm{d}\bar{\nu}| = L_{\lambda,bb}(\lambda,T)\,|\mathrm{d}\lambda| \rightarrow L_{\bar{\nu},bb}(\bar{\nu},T) = \left|\frac{\mathrm{d}\lambda}{\mathrm{d}\bar{\nu}}\right| L_{\lambda,bb}(\lambda,T) = \frac{10^4}{\bar{\nu}^2} L_{\lambda,bb}(\lambda,T) \tag{7.32}$$

With this, we can now rewrite (7.30) to the spectral radiance in units of W m^{-2} sr^{-1} (cm^{-1})$^{-1}$:

$$L_{\bar{\nu},bb}(\bar{\nu},T) = \frac{2\cdot 10^8 hc_0^2\bar{\nu}^3}{e^{100hc_0\bar{\nu}/k_bT}-1} \tag{7.33}$$

Plotting (7.30) and (7.33) for a given temperature, will show a shift in the peak. This is due to the fact that the spectral radiance is calculated per spectral unit. The position of the peak can be calculated using Wien's displacement law (usually written for units of μm), but will have to be done cautiously because of this dependence on the unit chosen [138–140]. Obviously, the total amount of energy will remain the same, since it depicts the same physical quantity. Only how this energy is divided along the spectrum depends in fact, on the dispersive element used. In [138], Heald states that diffraction gratings give experimental dispersion that approximates the linear-wavelength rule, whereas prisms approximate the frequency-squared rule.

Since this thesis reports of a spectrometer design using a dispersive element that is designed to be linear in wavelength, it seems most appropriate to use wavelength as the main unit. We will therefore describe the Wien peak as:

$$L_{peak} = \frac{b}{T} \tag{7.34}$$

where $b = 2.898\cdot 10^{-3}$ m K is Wien's constant.

We can integrate the spectral radiance with respect to the solid angle to obtain the *spectral exitance* (i.e. *spectral emissive power*) [W m^{-2} μm^{-1}]. Since the black body under consideration here is by definition a diffuse emitter, its exitance is written as [134]:

$$M_{\lambda,bb}(\lambda,T) = \pi L_{\lambda,bb}(\lambda,T) = \pi\frac{2\cdot 10^{-6}hc_0^2}{\lambda^5 e^{hc_0/\lambda kT_s}-1} \tag{7.35}$$

And its *exitance* [W m^{-2}] as:

$$\int_0^\infty M_{\lambda,bb}(\lambda,T)\mathrm{d}\lambda = \frac{2\pi^5 k_b^4}{15h^3c_0^2}T^4 = \sigma T^4 \tag{7.36}$$

This is called the fundamental *Stefan-Boltzmann law* and represents the maximum amount of power per unit area that can be radiated from any thermal source. It is always valid and, unlike the spectral radiance, is independent of the unit chosen. The Stefan-Boltzmann constant σ is independent of surface, medium and temperature and has the value $5.6697\cdot 10^{-8}$ Wm^{-2}K^{-4}.

Similarly we can define the *incidence*, $E_{\lambda,bb}(\lambda,T)$. Exitance and incidence have the same units, but have different interpretations. Exitance is the amount of power per unit area that leaves a surface (either generated by the matter or reflected from it), while incidence is the amount of power per unit area that is incident on a surface.

Radiative power transfer

Now let us assume a system with a source and a detector which are both perfectly opaque (i.e. no radiation is transmitted through the device) and diffuse. If we consider a point x located

on the source's surface with spectral emissivity $\varepsilon_{\lambda,x}$, reflectivity, $\rho_{\lambda,x}$, absorptivity $\alpha_{\lambda,x}$ and temperature T_x; And a point y located on the detector's surface with spectral emissivity $\varepsilon_{\lambda,y}$, reflectivity, $\rho_{\lambda,y}$, absorptivity $\alpha_{\lambda,y}$ and absolute temperature T_y. The spectral exitance at y, is then defined as the sum of the reflected incidence and the generated radiation:

$$M_{\lambda,y} = \rho_{\lambda,y} E_{\lambda,y} + \varepsilon_{\lambda,y} \sigma T_y^4 \tag{7.37}$$

The net inward spectral radiative heat flux at point y, $q_{rad,in,\lambda,y}$ [W m^{-2}], is then given by the difference between the incidence and the exitance at point y.

$$q_{rad,in,\lambda,y} = E_{\lambda,y} - M_{\lambda,y} = (1 - \rho_{\lambda,x}) E_{\lambda,y} - \varepsilon_{\lambda,y} \sigma T_y^4 \tag{7.38}$$

Most opaque bodies behave as ideal grey bodies, meaning that the spectral absorptivity and emissivity are equal. The spectral reflectivity is therefore given as:

$$\alpha_\lambda = \varepsilon_\lambda = 1 - \rho_\lambda \tag{7.39}$$

Thus, for ideal grey bodies like presented here, $q_{rad,in,y}$ is given by [141]:

$$q_{rad,in,\lambda,y} = \varepsilon_{\lambda,y} (E_{\lambda,y} - \sigma T_y^4) \tag{7.40}$$

7.5.3 Micro mechanics

To have some understanding on what happens mechanically, also some basic analysis has been done on this part. As time is very limited, in this thesis no full mechanical analysis has been performed whatsoever. For some parts of the design very basic analysis is done, where other parts merely the experience of the supervisors is used to asses if it is all structurally sound.

7.5.3.1 Process residual stresses

Due to details of the deposition process, residual stresses often appear in thin-films during the processing. These stresses can be characterized as either intrinsic or extrinsic, depending on the mechanism by which it develops and are either compressive or tensile. Intrinsic stresses are also known as growth stresses, as they result directly from the film nucleation process itself. Extrinsic stresses result from some externally imposed factor like a mismatch in thermal expansion coefficient [142].

Intrinsic stress

During fabrication several techniques will be used including doping, chemical vapour deposition (CVD) and sputtering. As the intrinsic stresses are induced in thin films mainly by the re-aggregation of crystalline grains of thin film materials, intrinsic stress is thought to be of minor concern for the CVD process [143]. However, both doping and sputtering can result in significant intrinsic stresses.

The biggest problem is that credible methods for quantifying the intrinsic stresses are not currently available, because the distribution of materials in thin films is not likely to be uniform across the area on which they are deposited. The use of continuum mechanics theory with average material behaviour to asses the stresses is therefore not realistic. Therefore, intrinsic stresses are usually determined by means of empirical evaluation.

Extrinsic stress: Thermal mismatch

The thermal mismatch strain, $\varepsilon_{mismatch}$, between a film and the substrate it is deposited on is found by equating [142]:

$$\varepsilon_{mismatch} = (\alpha_{T,f} - \alpha_{T,s})(T_d - T_r) \tag{7.41}$$

where $\alpha_{T,f}$ and $\alpha_{T,s}$ are the coefficients of thermal expansion of the film and substrate, respectively and T_d and T_r are the deposition and room temperatures. From equation 7.41, we see that the extra expansion or contraction of the thin film as it cools down from T_d to T_r, is directly proportional to the difference of the thermal expansion coefficients.

The resulting stress in the thin-film from this strain, $\sigma_{mismatch}$ [Pa], may than be calculated using [142]:

$$\sigma_{mismatch} = \frac{E}{1-\nu} \cdot \varepsilon_{mismatch} \tag{7.42}$$

where E [Pa] is the Young's modulus and ν is the Poisson's ratio.

7.5.3.2 Buckling

All these stresses combined, may result in the buckling of the bridge. If we assume a double clamped bridge the problem becomes exactly the same as a column with both ends fixed against rotation. In this case we can determine the critical stress, σ_{crit} [Pa], above which buckling will occur by using [144]:

$$\sigma_{crit} = \frac{P_{crit}}{A} = \frac{\pi^2 EI}{AL_{eff}^2} \tag{7.43}$$

Where P_{crit} [N] is the critical force, A is the cross-sectional area and $L_{eff} = L/2$ is the effective length.

Because we will be dealing with composite beams, before we can solve this equation, we will have to start by finding the neutral axis. This neutral axis is found from the condition that the resultant axial force acting on the cross section is zero. Therefore, for a composite beam with n layers, we can write [144]:

$$E_1 \int_1 z_1 \mathrm{d}A + E_2 \int_2 z_2 \mathrm{d}A + ... + E_n \int_n z_n \mathrm{d}A = 0 \tag{7.44}$$

where z is the distance of the normal stresses from the neutral axis. It is understood that the first integral is evaluated over the cross-sectional area of material 1, etc.

We can now use this definition of the neutral axis to find the effective moment of inertia, I_{eff} [m^4], using the parallel plate theorem [144]:

$$I_{eff,n} = I_{0,n} + A_n z_n^2 = \frac{b}{12} t_n^3 + b t_n z_n^2 \tag{7.45}$$

where b is the width of the beam and t_n the thickness of the material layer n.

Finally we can state:

$$EI = E_1 I_{eff,1} + E_2 I_{eff,2} + ... + E_n I_{eff,n} \tag{7.46}$$

7.5.3.3 Static loading of a thin, pillar supported sheet

To attain a simplified expression for the lateral deflection of a thin continuous plate over many columns, several assumptions are made:

1. The plate is subjected to a uniform load, q [Pa].
2. The column cross sections are so small that their reactions on the plate are regarded as point loads.
3. The columns are equally spaced in mutually perpendicular directions.
4. The dimensions of the plate are large as compared to the column spacing.

It is therefore considered as a uniformly loaded rectangular plate ($W \times L$) supported at the corners by columns. Clearly, the maximum deflection, δ_z [m], occurs at the center of the panel and may be calculated with [145]:

$$\delta_z = \alpha \frac{qL^4}{D} \tag{7.47}$$

where L [m] is the longest span of the pillars, α is a constant dependent on the ratio between the longest and shortest span of the pillars given by table 7.4 and D [Nm] is the mechanical rigidity defined as:

$$D = \frac{Et^3}{12(1-\nu^2)} \tag{7.48}$$

where t [m] is the sheet thickness.

L/W	α
1.0	0.00581
1.1	0.00487
1.2	0.00428
1.3	0.00387
1.4	0.00358
1.5	0.00337
2.0	0.00292
∞	0.00260

Table 7.4: Deflection constant at the center of a panel supported by rows of equidistant columns.

7.5.3.4 Shock loading

To determine the maximum shock that a double sided clamped beam can handle before stiction to the top or bottom will occur, we will first determine the maximum distributed load, q_{max} [N m^{-1}], by [144]:

$$q_{max} = \frac{384\delta_{z,max}EI}{L^4} \tag{7.49}$$

where $\delta_{z,max}$ [m], is the maximum allowable deflection, E [Pa], is the Young's modulus, I [m^4], is the second moment of area and L [m], is the length of the beam.

Using equation (7.49), we can now determine the maximum acceleration, a_{max} [m s^{-2}], allowed:

$$a_{max} = \frac{F_{max}}{m} = \frac{q_{max}L}{\rho V} = \frac{q_{max}}{\rho W t} \tag{7.50}$$

where F_max [N] is the maximum allowable force, m [kg] is the mass of the bridge, ρ [kg m^{-3}] is the density and V [m^3] the volume.

7.5.3.5 Eigen frequency

Another way of creating a deflection that will cause stiction is by exciting the device at its eigen frequency. An approximation of the first eigen frequency, ω_1 [rad], of a double sided clamped beam is given by:

$$\omega_{1,clamp} = \frac{\omega_0}{\sqrt{13}} = 22.74\sqrt{\frac{EI}{\rho AL^4}} = 22.74\sqrt{\frac{EI}{\rho WtL^4}} \tag{7.51}$$

and for a supported beam by:

$$\omega_{1,sup} = \sqrt{7.31 \cdot 10^{-3}} \cdot \omega_0 = 7.01\sqrt{\frac{EI}{\rho AL^4}} \tag{7.52}$$

7.6 Modeling

7.6.1 Thermal modeling of a pixel

Cell title(s): RESULTING SPACTRAL WINDOW PER PIXEL AS RESULT OF LVOF;
ABSORBED POWER PER PIXEL;
PIXEL CHARACTERISTICS

Sub-function(s): N/A

To be able to calculate the output voltage of a pixel, we require the temperature difference between the hot and cold junctions of the thermopile. To get to this temperature difference, this section will divide the problem in three parts and solve these individually using the theory as explained in sections 5.3 and 7.5.2.

First we will determine the amount of power absorbed by the pixel. Second, the heat loss from the absorber to its surroundings through radiation and conduction will be looked at. Third and final, we will use the information from the first two steps to determine the heat gradient across the beam with which the absorber is connected to the bulk material, which acts as the heat sink as illustrated in figure 7.13

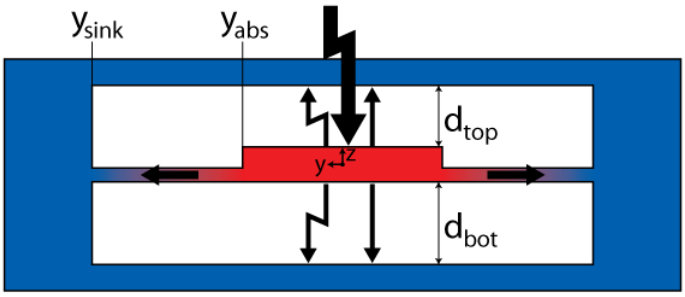

Figure 7.13: Schematic drawing of identifiable heat transfer mechanisms. The straight arrows represent the conduction paths, the lightning shaped arrows the radiation. The difference in heat is represented by the different colors, red being high, blue being low.

Step I: The absorbed power

Assuming a uniformly lit detector, we can state:

$$E_p = E_d \frac{A_p}{A_d} \tag{7.53}$$

where A_p and A_d are the areas of the pixel and detector, respectively. Substituting equations (5.13) and (7.53) in (7.40) and solve for a uniform surface we get:

$$q_{rad,in,\lambda,d} = \varepsilon_{\lambda,d} \left[\frac{A_p}{A_d} L_{\lambda,s} \mathcal{T}_\lambda A_s 2\pi(1 - \cos\theta) - \sigma T_d^4 \right] \tag{7.54}$$

where $L_{\lambda,s}$ may for example be given by equation (7.30) or (7.31), $\mathcal{T}_\lambda$ is the total spectral transmittance as a result of the gas and all the optics and T_d is the absolute temperature of the detector. The subscripts s and d indicate the source and detector, respectively. The absorbed

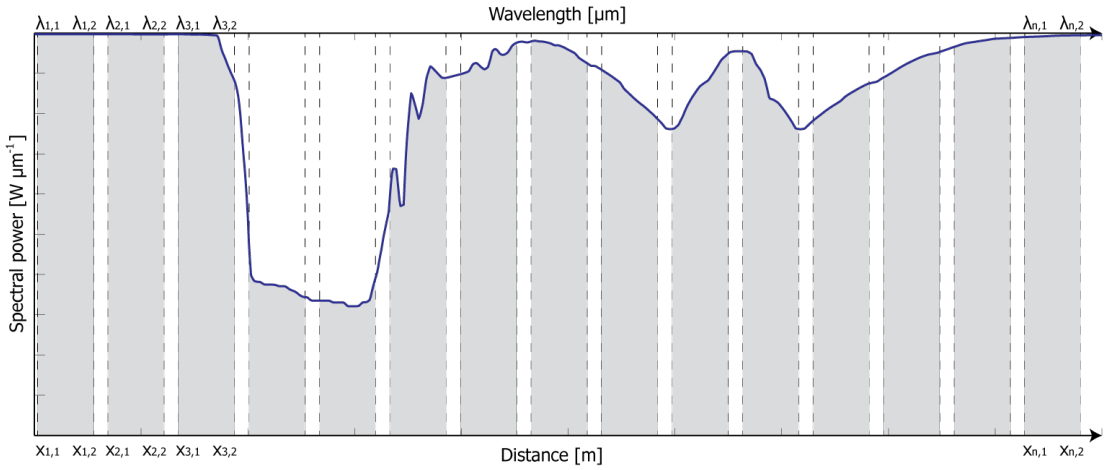

Figure 7.14: Figure to indicate how the spectral windows of the pixels are defined. The grey area is the amount of absorbed power.(Amount of pixels is not representative)

power by pixel n, $P_{abs,n}$ [W], may then be calculated by integrating over that part of the spectrum which is 'seen' by the pixel due to the linear variable optical filter.

$$P_{abs,n} = A_p \int_{\lambda_{n,1}}^{\lambda_{n,2}} \varepsilon_{\lambda,d} \left[\frac{A_p}{A_d} L_{\lambda,s} \mathcal{T}_\lambda A_s 2\pi(1 - \cos\theta) - \sigma T_d^4 \right] \mathrm{d}\lambda \tag{7.55}$$

The limits of the integral are determined by simply dividing the spectrum equally along the pixels as shown in figure 7.14. This is quite a rough approximation since it does not include the actual intensity profile of the incident light. Improvements may therefore be made on this part.

Step II: Thermal losses from the absorber to its surroundings

A closer look at the detector identifies two conduction paths from the absorber, through the surrounding gas, to the detector's enclosure as shown in figure 7.13. If we assume a steady state

condition (i.e. thermal equilibrium), the heat losses by means of the conductive fluxes can be calculated using (7.24), which in this particular case may be written as:

$$q_{cond,abs-top} = \frac{\kappa_{air}(T_{abs} - T_{amb})}{d_{top}}; \quad q_{cond,abs-bot} = \frac{\kappa_{air}(T_{abs} - T_{amb})}{d_{bot}} \tag{7.56}$$

Where d_{top} and d_{bot} are the distances from the device to the top and to the bottom respectively and T_{abs} and T_{amb} are the absorber and ambient temperatures. The minus signs are dropped because we want to know the absolute flux that is leaving through these conduction paths.

Assuming the ambient to be a perfect grey body, we can use equation (7.40) to describe the net outward radiative flux as:

$$q_{rad,abs,out} = -q_{rad,abs,in} = \varepsilon_{abs}\sigma(T_{abs}^4 - T_{amb}^4) \tag{7.57}$$

where we substituted $E_{\lambda,y}$ with σT_{amb}^4.

Since the temperature of the absorber is only moderately higher than the ambient temperature, we can state that $T_{abs} > T_{amb} > 0$ and $\frac{T_{abs}-T_{amb}}{T_{amb}} \ll 1$, Thus:

$$1 < \frac{T_{abs}}{T_{amb}} \ll 2 \rightarrow \frac{T_{abs}}{T_{amb}} \approx 1 \tag{7.58}$$

Using these simplifications (7.57) becomes:

$$\begin{aligned} q_{rad,abs,out} &= \varepsilon_{abs}\sigma(T_{abs} + T_{amb})(T_{abs}^2 + T_{amb}^2)(T_{abs} - T_{amb}) \\ &= \varepsilon_{abs}\sigma T_{amb}^3 \left(\frac{T_{abs}}{T_{amb}} + 1\right)\left(\left(\frac{T_{abs}}{T_{amb}}\right)^2 + 1\right)(T_{abs} - T_{amb}) \\ &\approx 4\varepsilon_{abs}\sigma T_{amb}^3(T_{abs} - T_{amb}) \end{aligned} \tag{7.59}$$

Because we are not interested in the temperature gradient along the surrounding gas, but merely in the total power lost, we can state:

$$\begin{aligned} P_{abs,loss} &= A_{abs}(q_{cond,abs-top} + q_{cond,abs-bot} + q_{rad,abs,out}) \\ &= A_{abs}(T_{abs} - T_{amb})\left(4\varepsilon_{abs}\sigma T_{amb}^3 + \kappa_{gas}\left(\frac{1}{d_{top}} + \frac{1}{d_{bot}}\right)\right) \end{aligned} \tag{7.60}$$

Where $A_{abs} = 2y_{abs}W$, is the absorber area.

Step III: Determination of the temperature gradient across the beams.

We can represent any conductive heat flux in two ways: By Fourier's law of heat conduction (7.23) and by its definition. The former gives us:

$$q_{abs-beam} = -\kappa_{beam}\frac{dT}{dy} \tag{7.61}$$

In which κ_{beam} is represented by:

$$\kappa_{beam} = \frac{\sum(\kappa_i \cdot t_i)}{\sum t_i} \tag{7.62}$$

With film thicknesses t_i and thermal conductances κ_i (i=1,2,3,...).

The second representation of the conductive heat flux is through its definition, which is the energy that flows through a particular surface per unit area per unit time. We know that all the

heat left in the absorber would like to conduct through the two absorber-beam surface areas, $A_{abs-beam}$ to obtain equilibrium. Therefore we can write:

$$q_{abs-beam} = \frac{P_{abs,in} - P_{abs,loss}}{2A_{abs-beam}} = \frac{P_{abs,in} - P_{abs,loss}}{2W\sum t_i} \tag{7.63}$$

Where W is the width of the beam. Using equations (7.60)-(7.63) we get:

$$\begin{aligned} \left.\frac{\mathrm{d}T(y)}{\mathrm{d}y}\right|_{y=y_{abs}} &= \frac{P_{abs,loss} - P_{abs,in}}{2W\sum(\kappa_i \cdot t_i)} \\ &= y_{abs}\left(T_{abs} - T_{amb}\right)\beta_{abs}^2 - \frac{P_{abs,in}}{2W\sum(\kappa_i \cdot t_i)} \end{aligned} \tag{7.64}$$

Where the *heat transfer coefficient*, β_{abs} [m^{-1}] is given by:

$$\beta_{abs} = \sqrt{\frac{4\varepsilon_{abs}\sigma T_{amb}^3 + \kappa_{gas}\left(\frac{1}{d_{top}} + \frac{1}{d_{bot}}\right)}{\sum(\kappa_i \cdot t_i)}} \tag{7.65}$$

Of course, also the beam will endure losses through its surroundings. We will therefore have to take the same steps as we did earlier for the absorber, with the exception that this time we are interested in the temperature gradient.

$$q_{cond,beam-top} = \frac{\kappa_{gas}(T(y) - T_{amb})}{d_{top}}; \quad q_{cond,beam-bot} = \frac{\kappa_{gas}(T(y) - T_{amb})}{d_{bot}} \tag{7.66}$$

Where d_{top} and d_{bot} are the distances from the device to the top and to the bottom respectively, T_{amb} is the ambient temperature and $T(y)$ is the temperature at point y on the beam.

The net outward radiative flux from the beam is again calculated by:

$$q_{rad,beam,out} = \varepsilon_{beam}\sigma(T(y)^4 - T_{amb}^4) \approx 4\varepsilon\sigma T_{amb}^3(T(y) - T_{amb}) \tag{7.67}$$

By applying the poisson equation (7.28), we get:

$$\frac{d^2[T(y) - T_{amb}]}{dy^2} + \frac{\dot{q}_s}{\kappa_{beam}} = 0 \tag{7.68}$$

Where $\dot{q}_s$ is the rate of internal energy conversion ("heat generation/loss") per unit volume. Because we will be using thermopiles, we may neglect any Joule heating of the beams. The rate of internal energy conversion is therefore simply given by:

$$\begin{aligned} \dot{q}_s &= -\frac{P_{cond,beam-top} + P_{cond,beam-bot} + P_{rad,beam,out}}{V} \\ &= -\frac{A_{beam}\left(4\varepsilon_{beam}\sigma T_{amb}^3(T(y) - T_{amb}) + \frac{\kappa_{gas}(T(y)-T_{amb})}{d_{top}} + \frac{\kappa_{gas}(T(y)-T_{amb})}{d_{bot}}\right)}{A_{beam}\sum t_i} \\ &= -\frac{(T(y) - T_{amb})\left(4\varepsilon_{beam}\sigma T_{amb}^3 + \kappa_{gas}\left(\frac{1}{d_{top}} + \frac{1}{d_{bot}}\right)\right)}{\sum t_i} \end{aligned} \tag{7.69}$$

Substituting (7.62) and (7.69) into (7.68), the second-order differential equation becomes:

$$\frac{d^2\left(T(y) - T_{amb}\right)}{dy^2} - \frac{\left(4\varepsilon_{beam}\sigma T_{amb}^3 + \kappa_{gas}\left(\frac{1}{d_{top}} + \frac{1}{d_{bot}}\right)\right)}{\sum(\kappa_i \cdot t_i)}\left(T(y) - T_{amb}\right) = 0 \tag{7.70}$$

Again assuming

$$\beta_{beam} = \sqrt{\frac{4\varepsilon_{beam}\sigma T_{amb}^3 + \kappa_{gas}\left(\frac{1}{d_{top}} + \frac{1}{d_{bot}}\right)}{\sum(\kappa_i \cdot t_i)}} \tag{7.71}$$

(7.70) becomes:

$$\frac{d^2\left(T(y) - T_{amb}\right)}{dy^2} - \beta_{beam}^2\left(T(y) - T_{amb}\right) = 0 \tag{7.72}$$

Whose general solution can be written as:

$$T(y) - T_{amb} = Ae^{-\beta_{beam}y} + Be^{+\beta_{beam}y} \tag{7.73}$$

To solve the second-order differential equation we will have to introduce some boundary conditions. We will start by assuming that the temperature distribution is uniform and that we have two points along the beam that are at a fixed temperature.

1. Heat sink boundary condition:
$$T(y_{sink}) = T_{amb} \tag{7.74}$$
2. Heat source boundary condition:
$$T(y_{abs}) = T_{abs} \tag{7.75}$$

Applying (7.74) and (7.75) to the general solution (7.73), we get:

$$Ae^{-\beta_{beam}y_{sink}} + Be^{+\beta_{beam}y_{sink}} = 0 \rightarrow A = -Be^{2\beta_{beam}y_{sink}} \tag{7.76}$$

And:

$$\begin{aligned} Ae^{-\beta_{beam}y_{abs}} + Be^{+\beta_{beam}y_{abs}} &= T_{abs} - T_{amb} \\ &\rightarrow B\left[e^{\beta_{beam}y_{abs}} - e^{\beta_{beam}(2y_{sink} - y_{abs})}\right] = T_{abs} - T_{amb} \end{aligned} \tag{7.77}$$

From which we derive A and B as:

$$A = -\frac{\left(T_{abs} - T_{amb}\right)e^{2\beta_{beam}y_{sink}}}{e^{\beta_{beam}y_{sink}}\left[e^{-\beta_{beam}(y_{sink} - y_{abs})} - e^{\beta_{beam}(y_{sink} - y_{abs})}\right]} \tag{7.78}$$

$$B = \frac{T_{abs} - T_{amb}}{e^{\beta_{beam}y_{sink}}\left[e^{-\beta_{beam}(y_{sink} - y_{abs})} - e^{\beta_{beam}(y_{sink} - y_{abs})}\right]} \tag{7.79}$$

Substituting A and B back again into (7.73) we get the particular solution of the second-order differential equation:

$$\begin{aligned} T(y) - T_{amb} &= \frac{\left(T_{abs} - T_{amb}\right)e^{\beta_{beam}y}}{e^{\beta_{beam}y_{sink}}\left[e^{-\beta_{beam}(y_{sink} - y_{abs})} - e^{\beta_{beam}(y_{sink} - y_{abs})}\right]} \\ &\quad - \frac{\left(T_{abs} - T_{amb}\right)e^{2\beta_{beam}y_{sink}}e^{-\beta_{beam}y}}{e^{\beta_{beam}y_{sink}}\left[e^{-\beta_{beam}(y_{sink} - y_{abs})} - e^{\beta_{beam}(y_{sink} - y_{abs})}\right]} \\ &= \left(T_{abs} - T_{amb}\right)\frac{e^{\beta_{beam}y_{sink}}\left[e^{-\beta_{beam}(y_{sink} - y)} - e^{\beta_{beam}(y_{sink} - y)}\right]}{e^{\beta_{beam}y_{sink}}\left[e^{-\beta_{beam}(y_{sink} - y_{abs})} - e^{\beta_{beam}(y_{sink} - y_{abs})}\right]} \\ &= \left(T_{abs} - T_{amb}\right)\frac{\sinh\left[-\beta_{beam}(y_{sink} - y)\right]}{\sinh\left[-\beta_{beam}(y_{sink} - y_{abs})\right]} \\ &= \left(T_{abs} - T_{amb}\right)\frac{\sinh\left[\beta_{beam}(y_{sink} - y)\right]}{\sinh\left[\beta_{beam}(y_{sink} - y_{abs})\right]} \end{aligned} \tag{7.80}$$

Consequently, the temperature distribution along the beam is given by:

$$T(y) = (T_{abs} - T_{amb}) \frac{\sinh\left[\beta_{beam}(y_{sink} - y)\right]}{\sinh\left[\beta_{beam}(y_{sink} - y_{abs})\right]} + T_{amb} \tag{7.81}$$

The derivative at point y_{abs} of which is given by:

$$\begin{aligned} \left.\frac{dT(y)}{dy}\right|_{y=y_{abs}} &= (T_{abs} - T_{amb}) \left.\frac{d\left\{\frac{\sinh[\beta_{beam}(y_{sink}-y)]}{\sinh[\beta_{beam}(y_{sink}-y_{abs})]} + T_{amb}\right\}}{dy}\right|_{y=y_{abs}} \\ &= (T_{abs} - T_{amb}) \frac{-\beta_{beam}\cosh\left[\beta_{beam}(y_{sink} - y_{abs})\right]}{\sinh\left[\beta_{beam}(y_{sink} - y_{abs})\right]} \\ &= -(T_{abs} - T_{amb})\,\beta_{beam}\coth\left[\beta_{beam}(y_{sink} - y_{abs})\right] \end{aligned} \tag{7.82}$$

Using equations (7.64) and (7.82) we can now state:

$$y_{abs}\,(T_{abs} - T_{amb})\,\beta_{abs}^2 - \frac{P_{abs,in}}{2W\sum(\kappa_i \cdot t_i)} = -(T_{abs} - T_{amb})\,\beta_{beam}\coth\left[\beta_{beam}(y_{sink} - y_{abs})\right] \tag{7.83}$$

Thus:

$$\begin{aligned} \Delta T = T_{abs} - T_{amb} &= \frac{P_{abs,in}}{\mathcal{G}} \\ &= \frac{P_{abs,in}}{2W\sum(\kappa_i \cdot t_i)\,(y_{abs}\beta_{abs}^2 + \beta_{beam}\coth\left[\beta_{beam}(y_{sink} - y_{abs})\right])} \end{aligned} \tag{7.84}$$

We can also use this to determine the thermal time constant, τ:

$$\tau = \frac{\mathcal{C}}{\mathcal{G}} = \frac{V\rho_{eq}c_{p,eq}}{2W\sum(\kappa_i \cdot t_i)\,(y_{abs}\beta_{abs}^2 + \beta_{beam}\coth\left[\beta_{beam}(y_{sink} - y_{abs})\right])} \tag{7.85}$$

where ρ_{eq} and $c_{p,eq}$ are the equivalent density and specific heat, respectively.

7.6.2 Modeling the thermopile

Cell title(s): PIXEL OUTPUT CALCULATION + VISUALIZATION;
Sub-function(s): N/A

Now we have the temperature difference between the hot and cold junctions of the thermopile we can easily calculate the output voltage, V_{tp} [V], according to:

$$V_{tp} = |\alpha_1 - \alpha_2| N \Delta T \tag{7.86}$$

where α_n is the Seebeck coefficient of material n.

This does not conclude the model of the thermopile however. One very important figure still to be calculated is the amount of noise introduced by the detector. The most prominent source of noise is the Johnson noise, v_n [V/$\sqrt{\text{Hz}}$], (i.e. Thermal noise or Nyquist noise) and is given by:

$$v_n^2 = 4k_b T R_{TP} \tag{7.87}$$

Where R_{TP} [Ω], is the resistance of the complete thermopile, which depends on the number N and the length L of the thermopile wires. Each thermocouple consists of a strip of N and

P-doped polySi connected by a short metal interconnect wire. The total thermopile resistance can be written as:

$$R_{TP} = N\frac{L}{W}(R_{\square,N} + R_{\square,P}) + 4NR_{contact} \tag{7.88}$$

Where $R_{contact}$ is the contact resistance between the polySi and the metal interconnect and $R_{\square,N}$ and $R_{\square,P}$ are the sheet resistance of the N and P-type polySi, respectively. Often the contact resistance is neglected.

7.7 Detailed design

As also becomes apparent from equation (7.84), one can imagine that a lower thermal conductivity of the beams will lead to an increased difference in temperature between the hot and cold junction of the thermopile. This could easily be reached by for example reducing the beam widths. However, except for the required mechanical rigidity, the beams are also the base layer (i.e. membrane) on which the thermopiles are located. Therefore a reduction in beam width, would reduce the amount of thermocouples in the thermopile and thus reduce the output. Also, the maximum beam width is dictated by the maximum pixel width, which in turn is dependent on the required spectral resolution.

One could also make the beams thinner or longer, but this will reduce the stiffness of the detector. We would not like the detector to stick to the top or bottom because of a small shock induced by handling during the process or measurements.

Unfortunately, many requirements, including the required spectral resolution, are not known. Therefore there has been chosen to create several designs. Together these designs should give good insight in the accuracy of the model and should be able to give us practical information on which paths to pursue further.

To be able to have some outline within which the design should fit, several parameters were defined at the beginning of the project, as indicated in figure 7.15(a). The length (along x-axis) of the detector array, for example, is set to 10 mm with a distance between pixels of 10 μm. This fits on a 15x15 mm chip and leaves some space to allow for the mounting of the LVOF chip on top of the detector. Also, the length of the absorber (along the y-axis) was set to the minimum width (along y-axis) of the LVOF, which was considered to be 3 mm. Furthermore the minimum thermocouple track width and track-to-track distance are set to 2 μm due to the accuracy limitations of the process.

This section will go into detail on the final designs and show all the simulation results as calculated by the MATLAB^{TM} model and Essential Macleod program. The former is mainly used to determine the length and width of the pixels, such that a good trade-off is found between spectral resolution, the responsivity, bandwidth and the footprint. Next to that it is used to determine the required thickness for certain layers to be structurally sound. The Essential Macleod program is used to determine the layer thicknesses of the infrared absorber layers to maximize absorption in the 3-5μm range.

Figure 7.15(b) gives a schematic side view of the final design. One can clearly identify the infrared absorber and the beams which connect the absorber to the bulk. The temperature gradient across the beams make them the perfect location for the thermopiles. Note also the vacuum encapsulation including the thin coating which covers the complete inside of the device.

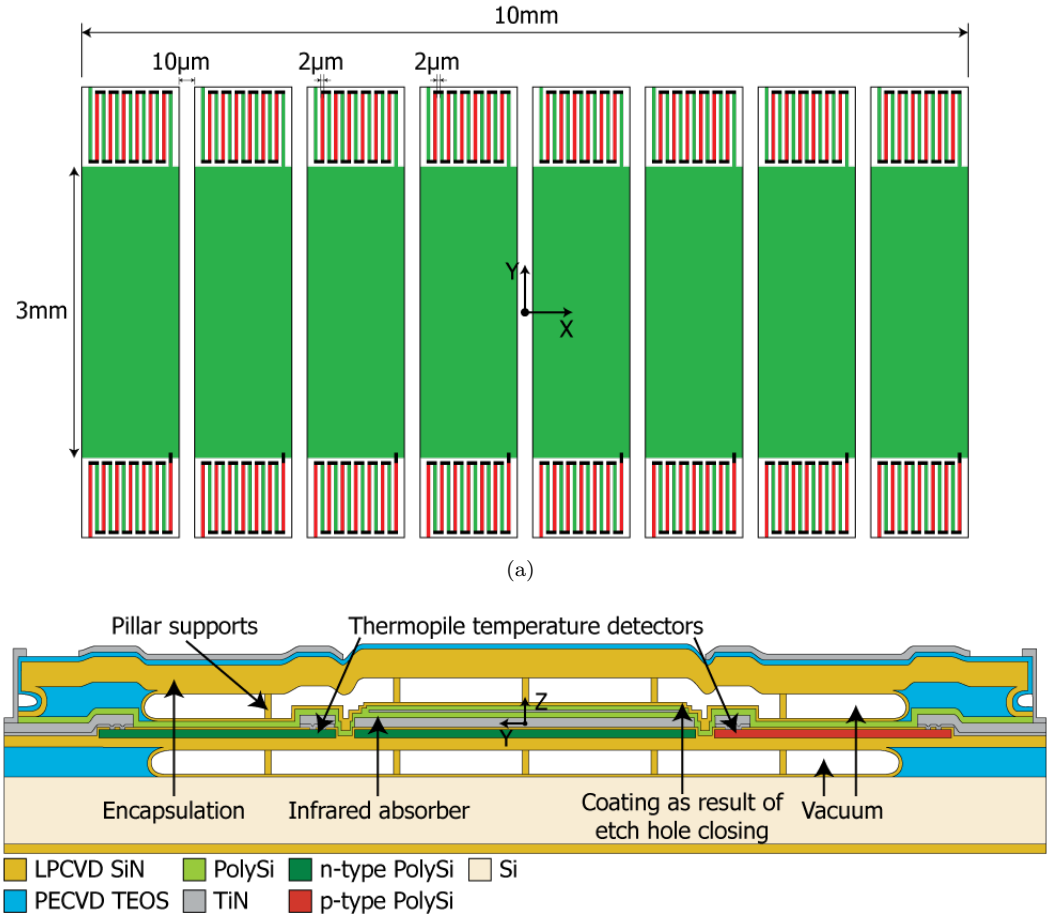

Figure 7.15: Schematic overview of the final design of the infrared detector, with a) Top view and b) Cross sectional view. Note: Drawing is not to scale.

7.7.1 Optical Design

As said, the width of the pixels determines the spectral resolution of the spectrometer, as shown in figure 7.16(a). Because the length of the absorber is fixed to 3 mm, the width is also the only parameter left which influences the amount of absorbed infrared light and thus ultimately the resolution with which the gas can be measured, shown in figures 5.10 and 7.16(b). The width should therefore be as small as possible, whilst being big enough to absorb enough light such that a reasonable resolution is achieved.

To be able to have several validation points, three designs were made using absorber widths of 100, 150 and 200 μm. These are expected to be in the right order of magnitude to which a more conclusive design could be made in subsequent research.

As described in section 7.4, we will have two different fabrication processes. One with vacuum encapsulation and one without. Therefore also two different absorbers have been designed, such

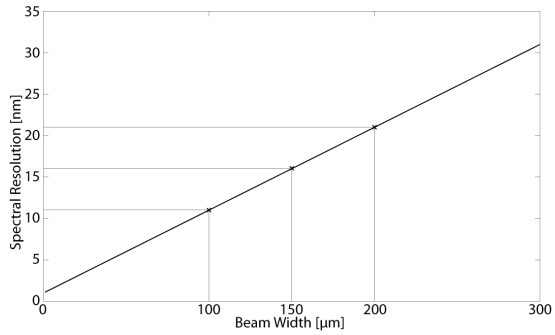

(a)

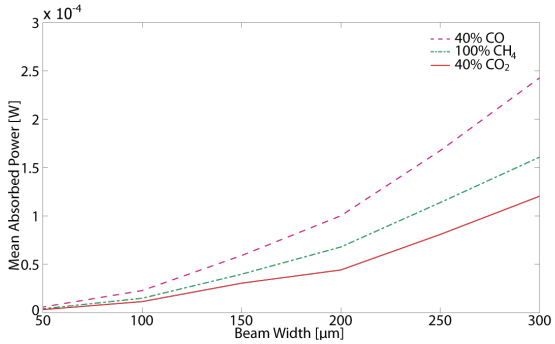

(b)

Figure 7.16: Dependencies on beam width for a) Spectral resolution and b) Mean absorbed power for maximum gas concentrations.

that absorption is maximized for either process. We have also seen in section 7.4, that we will use a thin-film absorber to collect the infrared radiation incident on the detector.

The optics have been designed using the commercially available Essential Macleod thin-film modeling software. The material data used can be found in appendix A. The center wavelength, λ_0, is always chosen to be 4 μm.

7.7.1.1 Thin-Film IR absorber: Low Temperature process

Let us divide the stack into its three sections: the bottom (i.e. back) reflector, the resonance layer and the top reflector.

The only purpose of the bottom reflector is to either absorb or reflect all the incident radiation. It is therefore obvious to use a material with a high refractive index. Unlike the reflectors designed earlier for the LVOF's, this time the reflector may actually absorb the radiation as well. Therefore the extinction coefficient is not important. By again looking at the available materials given in table 6.2, we can identify aluminium as the best candidate. The layer should only be thick enough to have no transmission. This would allow for a thickness of only 50 nm. However, aluminium layers of 675 nm are considered standard in IC processing. Since the total stack thickness in the low temperature process has no real maximum, there has been chosen to use this standard thickness.

The resonance layer should be a dielectric with a thickness as calculated by equation (7.7). Pretty much any dielectric material will suffice as long as it is process compatible. PolySi for example is not allowed to be deposited after aluminium. Because good results had been obtained with SiN as dielectric layer, this was the safest option.

The top reflector is more difficult. As discussed in section 7.5.1, it should not reflect any incident light, but it should contain the light in the dielectric layer to allow for the resonance to happen. Using the Essential Macleod software, it was found that a combination of TiN for the internal reflection and PECVD SiN as a top anti-reflection coating gave the best performance.

After optimization, the final design is given by the layers shown in table 7.5 and the absorption plot shown in figure 7.17.

Layer#	**Material**	**Optical thickness (FWOT)**	**Physical thickness [nm]**
Medium	Air		
1	PECVD SiN	0.218	425
2	TiN	0.024	16
3	PECVD SiN	0.311	606
4	Al	1.03	675
Substrate	Si		

Table 7.5: Mid infrared thin-film absorber design for the low temperature process.

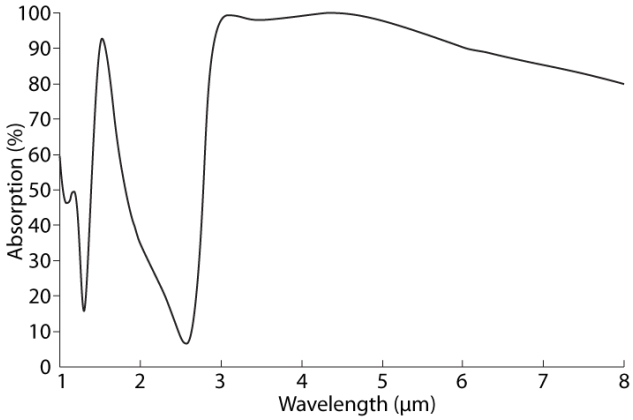

Figure 7.17: Absorption plot for the infrared absorber in the low temperature process.

The substrate material in this simulation is arbitrary and does not influence the performance, because the back reflector satisfies the requirement to have a transmittance of 0.

7.7.1.2 Thin-Film IR absorber: High Temperature process

Although the function of the layers remains the same between the low and high temperature processes, the difference in process does have a big influence on the final design of the absorber

stack. First of all we cannot use aluminium for the back reflector, simply because its melting temperature is too low for the high temperature process. Therefore this process will be using the next best candidate: titanium nitride (TiN). Titanium (Ti) is also possible, but has two major downsides. First of all, it is not resistant to vaporized Hydrofluoric (HF) acid, the etchant we would like to use. Second, it may oxidise, which, although only a surface phenomenon, might change the optical characteristics slightly and induce extra stresses.

The resonance chamber could simply be made of SiN again, but this would create a stack too thick for the encapsulation process. Therefore polySi has been chosen. Because of its high refractive index, the physical thickness can become much thinner.

To determine the top layer of the absorber for the high temperature process, we have to take the encapsulation into account. The influence of the encapsulation on the optical performance cannot be neglected and is therefore taken as part of the simulation. The exact layer thickness of the cap itself does not really influence the optical performance. However, its mechanical properties will determine the final thickness of the air gap which does influence the performance. Therefore a close relation exists between the mechanical properties of the encapsulation and the optical performance of the complete device. The calculation of the required cap thickness will be discussed in the next section and is considered given at this point.

Optimization with the Essential Macleod software resulted in the layers shown in table 7.6 and the absorption plot shown in figure 7.18.

Layer#	**Material**	**Optical thickness (FWOT)**	**Physical thickness [nm]**
Medium	Air		
1	SiO_2	0.234	675
2	LPCVD SiN	1.721	3200
3	Air	0.481	1925
4	LPCVD SiN	0.376	700
5	polySi	0.2356	240
6	TiN	0.037	25
7	polySi	0.285	290
8	TiN	0.221	150
Substrate	Si		

Table 7.6: Mid infrared thin-film absorber design for the high temperature process.

The top layer is the anti-reflection coating, followed by the encapsulation layer and the air gap (vacuum) between the encapsulation and the device. Layer 4 represents the layer of dense LPCVD SiN which acts as a sealer to reduce any out-gassing to a minimum (see also figure 7.15). The same layer will make sure that the sacrificial etch holes are plugged. The thickness of this layer is therefore dictated by the size of these holes.

Layer 5-8 make up the true absorber, similar to the one designed for the low temperature process. The reduced thickness of the resonance layer (layer 7) is apparent. Theoretically, even better optical performance can be achieved by using PECVD SiN or LPCVD SiN for layer 5, but this will create problems during the process. PECVD SiN will crack under the thermal stresses of the rest of the process. LPCVD SiN is deposited using dichlorosilane (SiCl2H2) as the source gas. The reaction produces hydrochloric acid (HCl), which will etch the titanium nitride (TiN)

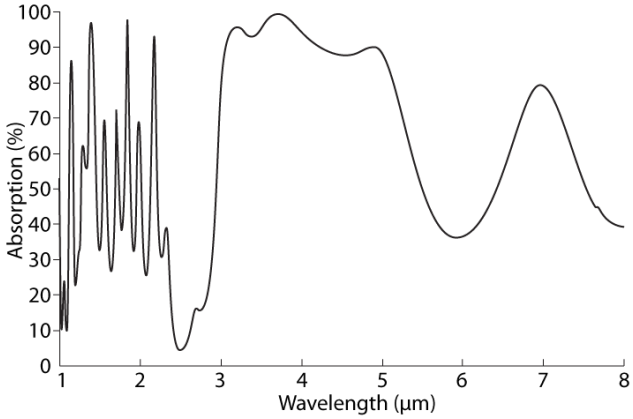

Figure 7.18: Absorption plot for the infrared absorber in the high temperature process.

layer. The latter could be prevented by depositing a 100 nm layer of SiO^2 on top of the TiN before deposition of the LPCVD SiN. However, the little bit of extra performance is considered not to outweigh the downside of more and thicker layers.

That the absorption is actually happening in the absorber and not in the encapsulation is shown in figure 7.19. The sensitivity of the absorptance to layer thickness variation is shown in figure 7.20 for the most critical layers.

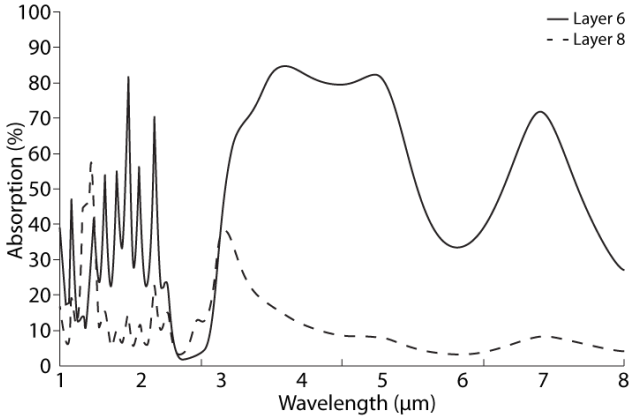

Figure 7.19: Absorption plot for the infrared absorber in the high temperature process.

7.7.2 Vacuum packaging

In section 7.4, we made a trade-off, which resulted in the use of a thin-film encapsulation to create the vacuum package. Obviously, the encapsulation should be stiff enough to make sure it does not sag to the point where it is in contact with the absorber. This is partly met by supporting the encapsulation with pillars. If we would have pillars in our pixel, we would loose absorbing area both due to the footprint of the pillar itself, but maybe also due to shadowing.

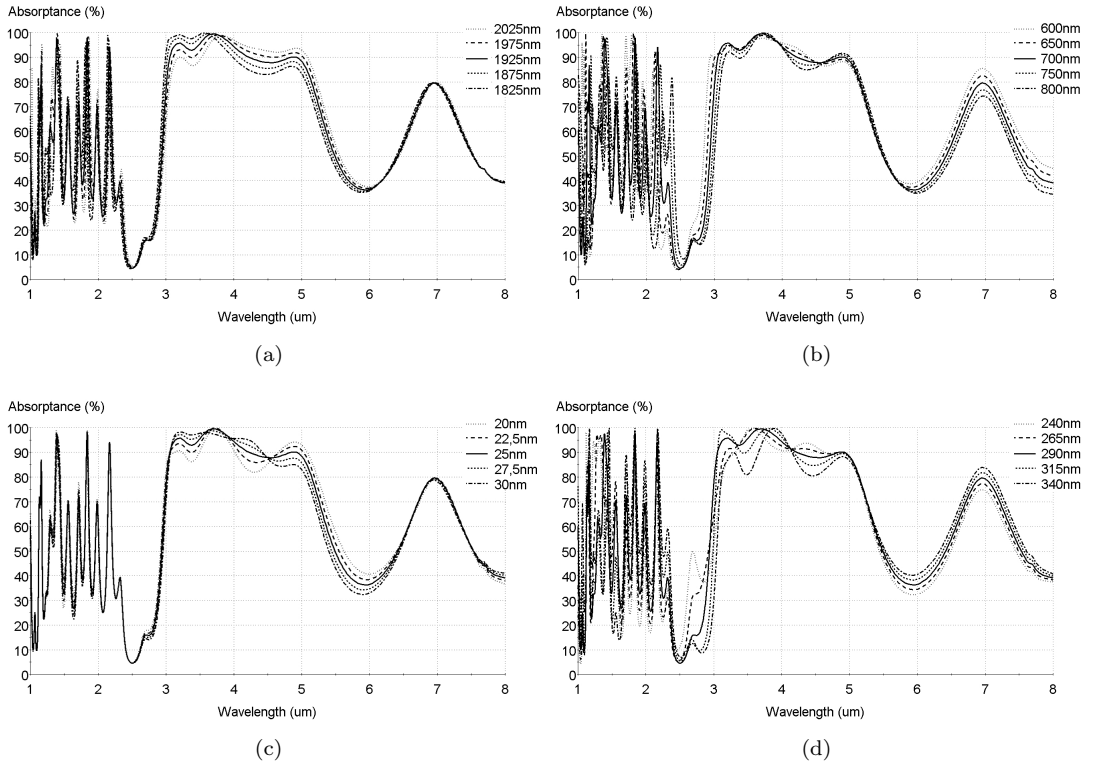

Figure 7.20: Sensitivity of the absorptance of the absorber to variations in layer thickness of a) Layer 3, b) Layer 4, c) Layer 6 and d) Layer 7.

We therefore chose to position the pillars between the pixels only, as shown in figure 7.21(a). This will therefore dictate the x-axis pillar pitch.

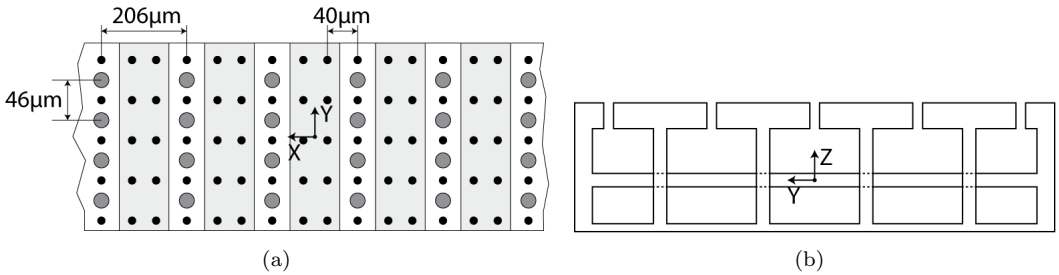

Figure 7.21: Schematic views of the detector with a) Top view. The light grey areas are the pixels, the darker grey dots the pillars which support the encapsulation and the black dots are the holes through which the sacrificial etching will be done. b) Side view. Etch holes are left open for clarification.

As said in the previous section, the mechanical properties of the cap are closely related to the optical performance of the device. The cap thickness and its material properties will result

in a certain amount of deflection under the static load resulting from the pressure difference. This deflection should be such that the air gap, t_{air}, is in close proximity of the value which we determined in the previous section to give us optimum optical performance.

Obviously, the final air gap is not only a property of the deflection, but also to the size of the air gap if no load is applied. This gap is determined by the thickness of the sacrificial material (PECVD TEOS), t_{sacr}, the amount of cap material removed during etching, t_{etched}, and the size of the sacrificial etch holes. The latter might seem odd, but the gap is reduced significantly when the holes are closed. Up to the point where the holes are completely closed, LPCVD SiN will be deposited uniformly across the inside of the device. Therefore, the gap is reduced by two times (top of absorber and bottom of the cap) the radius of the etch holes, r_{hole}. See also figure 7.15. The maximum deflection may therefore be given by:

$$\delta_z = t_{sacr} + t_{etched} - 2r_{hole} - t_{air} \tag{7.89}$$

The required thickness of the encapsulation may be calculated by rewriting equation (7.47). As said, the x-axis pillar pitch, L, is given by the pitch of the pixels and the y-axis pillar pitch, W, by the pitch of the etch holes. The static load, q, is defined by the pressure difference between the outside world and the vacuum inside. We can therefore list the following properties:

- $L = 206 \cdot 10^{-6}$ m
- $\alpha(L/W \gg 2) = 0.00260$
- $q = 1 \cdot 10^{5}$ Pa
- $\nu = 0.33$
- $E = 235 \cdot 10^{9}$ Pa
- $t_{sacr} = 4 \cdot 10^{-6}$ m
- $r_{hole} = 0.7 \cdot 10^{-6}$ m
- $t_{air} = 1.925 \cdot 10^{-6}$ m
- $t_{etched} = 157 \cdot 10^{-9}$ m

We can therefore write:

$$\delta_z = 4 \cdot 10^{-6} + 157 \cdot 10^{-9} - 1.4 \cdot 10^{-6} - 1.925 \cdot 10^{-6} = 832 \cdot 10^{-9}\text{m} \tag{7.90a}$$

$$t_{cap} = \sqrt[3]{0.00260 \frac{12 \times 1 \cdot 10^{5}(1 - 0.33^2)(206 \cdot 10^{-6})^4}{235 \cdot 10^{9} \times 832 \cdot 10^{-9}}} = 2.95 \cdot 10^{-6}\text{m} \tag{7.90b}$$

As said before, the sacrificial etching removes quite a significant amount of SiN from the cap. On the other hand, the closing of the etch holes will deposit quite some material as well, both on the bottom and top of the cap. Together, this means that the initial amount of LPCVD SiN to be deposited should be 2.95+0.16-2x0.7 = 1.71 μm. Because we can only deposit 1.5 μm at a time, we can get the last 0.21 μm by continuing to deposit after the sacrificial etch holes are closed. So we will deposit 1.5 μm of LPCVD SiN, do the sacrificial etching, close the holes with 0.7 μm and continue for another 0.21 μm to get the required thickness.

7.7.3 Thermal Design

7.7.3.1 Thermal conductivity

Although it is difficult to get to one optimized design, as said in the introduction of this section, one important aspect that always holds, regardless of the requirements, is to make sure no one layer in the beam dominates the thermal conductivity. Both the thickness and material of the membrane and the thermocouples are considered given by earlier conducted research [42, 131]. The thicknesses of the other layers are dictated solely by the optical design. In tables 7.7-7.10, one can find the stacks of the resulting beams and absorbers after the both the high and low temperature processes. Although both thermocouple poles will be on the same layer, they are mentioned separately to indicate their different thermal conductivity.

Layer #	**Application**	**Material**	**Thickness [nm]**	**Thermal Conductivity κ [W m^{-1} K^{-1}]**
9	Passivation	LPCVD SiN	700	1.55
8	Anti-reflection	Undoped PolySi	240	13.8
7	Front Reflector	TiN	25	19.2
6	Resonance	LPCVD SiN	606	3.2
5	Back Reflector	TiN	150	19.2
4	Passivation	LPCVD SiN	100	1.55
3	Thermocouple (-)	LPCVD n-type PolySi	300	29
2	Membrane	LPCVD SiN	700	1.55
1	Passivation	LPCVD SiN	700	1.55

Table 7.7: Final layers of the absorber after the high temperature process.

Layer #	**Application**	**Material**	**Thickness [nm]**	**Thermal Conductivity κ [W m^{-1} K^{-1}]**
6	Passivation	LPCVD SiN	700	1.55
5	Anti-reflection	Undoped PolySi	240	13.8
4	Passivation	LPCVD SiN	100	1.55
3	Thermocouple (+)	LPCVD p-type PolySi	300	34
3	Thermocouple (-)	LPCVD n-type PolySi	300	29
2	Membrane	LPCVD SiN	700	1.55
1	Passivation	LPCVD SiN	700	1.55

Table 7.8: Final layers of the beams after the low temperature process.

Therefore the only design parameters are the length and the width of the beams. As said in the previous section, we have three different absorber widths: 100, 150 and 200 μm. These determine the maximum width of the beams. Figures 7.22(a) and 7.23(a) show the thermal conductances of the different layers of the beam as a function of the beam width. This assumes

Layer #	Application	Material	Thickness [nm]	Thermal Conductivity κ [W m^{-1} K^{-1}]
7	Anti-reflection	PECVD SiN	425	3.2
6	Front Reflector	TiN	16	19.2
5	Resonance	PECVD SiN	606	3.2
4	Back Reflector	Al	675	19.2
3	Passivation	LPCVD SiN	100	1.55
2	Thermocouple (-)	LPCVD n-type PolySi	300	29
1	Membrane	LPCVD SiN	700	1.55

Table 7.9: Final layers of the absorber after the low temperature process.

Layer #	Application	Material	Thickness [nm]	Thermal Conductivity κ [W m^{-1} K^{-1}]
4	Anti-reflection	PECVD SiN	425	3.2
3	Passivation	LPCVD SiN	100	1.55
2	Thermocouple (+)	LPCVD p-type PolySi	300	34
2	Thermocouple (-)	LPCVD n-type PolySi	300	29
1	Membrane	LPCVD SiN	700	1.55

Table 7.10: Final layers of the beams after the high temperature process.

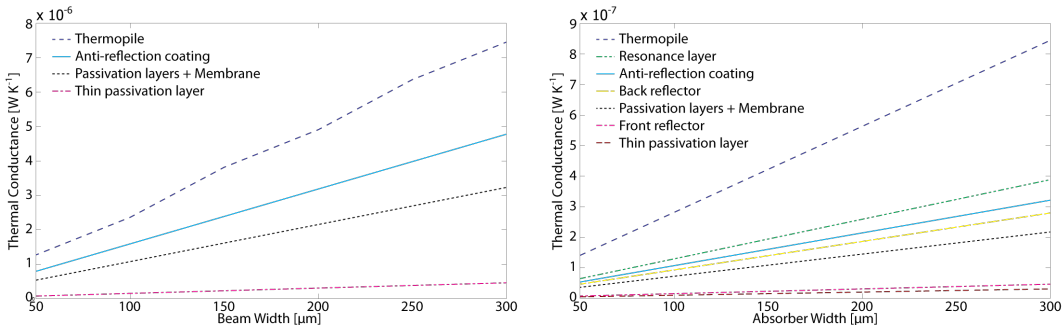

(a) (b)

Figure 7.22: Thermal conductances for the different layers of a) the beam and b) the absorber of the high temperature process, as function of their width.

we would fill the membrane to its maximum capacity, with minimum sized thermocouple tracks. It clearly shows that the thermal conductance of the thermopile is the largest as expected, but in the same order of magnitude. The thermal conductance of the anti-reflection coating is also quite significant. Although this layer is not required for the beam itself, it saves a mask step in

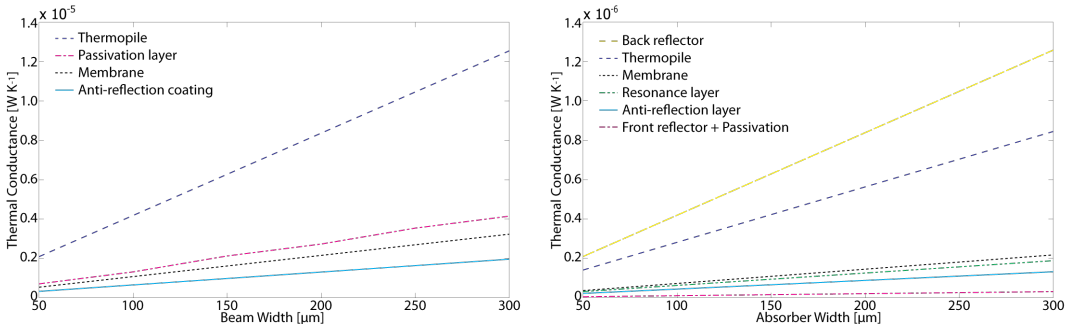

(a) (b)

Figure 7.23: Thermal conductances for the different layers of a) the beam and b) the absorber of the low temperature process, as function of their width.

the process to leave the layer.

Similarly, figures 7.22(b) and 7.23(b) show the thermal conductances for the layers of the absorber. For the high temperature process, the thermopile layer is again the most dominant. The low temperature process shows the back reflector as the most dominant. This makes complete sense since this layer is very thick. The order of magnitude lower values compared to the layers of the beam are assigned to the much larger length of the absorber. Although it might seem a problem, it is assumed that the absorber will be lit uniformly and will therefore heat uniformly. A reasonably good thermal conductance will only enhance this uniformity.

The exact figures are of course very dependent on the material properties. These may differ per process and are not yet known for our process at this stage. Because of this, the same order of magnitude is currently considered good enough. Further research may optimize this design.

As with some of the layer thicknesses, at the beginning of the project the beam length was also considered given by earlier conducted research [42] and was set to 250μm. However, later review showed that for this particular design, the optimum beam length is more in the order of 600-750 μm, as shown in figure 7.24. Unfortunately this knowledge came too late to change the design.

7.7.3.2 Response time

The response time is considered not to be very important, because the gas composition will most likely not change that fast. Still it is a good habit to check the performance of the design in this respect. The thermal time constant, τ [s], is calculated using:

$$\tau = \frac{\mathcal{C}}{\mathcal{G}} = \frac{V\rho_{eq}c_{p,eq}}{2W\sum\kappa_i t_i\left(y_{abs}\beta_{abs}^2 + \beta_{beam}\coth\left[\beta_{beam}(y_{sink}-y_{abs})\right]\right)} \tag{7.85}$$

To calculate the equivalent density, ρ_{eq} and equivalent specific heat, $c_{p,eq}$, we will use the layer dimensions as we have determined up to this point. Let us summarize these dimensions for a 200μm wide pixel of the high temperature process in table 7.11 and the thermal properties of the used materials in table 7.12. When we do this for all three pixel widths we can see that there is hardly any influence of the pixel width on the thermal time constant due to the similar increase in both conductance and heat capacity. The result is a thermal time constant of 0.32 for the

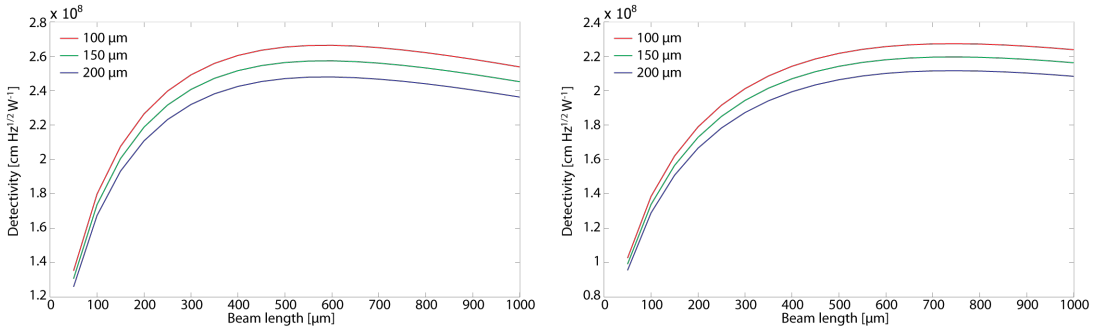

(a) (b)

Figure 7.24: Detectivity versus beam length for several beam widths. a) Low temperature b) high temperature design.

pixels in the high temperature and 0.28 for the low temperature process, making it fast enough for a 1 Hz measurement system, which seems to be sufficient.

Application	**Material**	**Dim X [μm]**	**Dim Y [μm]**	**Dim Z [nm]**	**Volume [m^3]**	**Mass [kg]**
Passivation	LPCVD SiN	196	3506	700	4.81E-13	1.49E-9
Anti-Reflection	LPCVD PolySi	196	3506	240	1.65E-13	3.84E-10
Reflector	TiN	196	3090	25	1.51E-14	8.18E-11
Reson. Cavity	LPCVD PolySi	196	3090	290	1.76E-13	4.09E-10
Reflector	TiN	196	3090	150	9.08E-14	4.91E-10
Passivation	LPCVD SiN	196	3506	100	6.87E-14	2.13E-10
Thermocouple	Doped LPCVD PolySi	196	3090	300	1.82E-13	4.23E-10
Thermocouple	Doped LPCVD PolySi	108	208	300	6.74E-15	1.57E-11
Thermocouple	Doped LPCVD PolySi	108	208	300	6.74E-15	1.57E-11
Membrane	LPCVD SiN	196	3506	700	4.81E-13	1.49E-9
Passivation	LPCVD SiN	196	3506	700	4.81E-13	1.49E-9
Total					2.15E-12	6.51E-9

Table 7.11: Final layer dimensions for a single 200μm pixel of the high temperature process.

7.7.3.3 Pixel crosstalk

One of the reasons to operate the device in a vacuum environment, is to eliminate pixel crosstalk. For this thesis, it is assumed that the pressure will be low enough to make any crosstalk negligible. A more detailed analysis has been performed by Wu [131].

Material	Volume %	Mass %	**Density** ρ_0 **[kg m^{-3}]**	**Specific heat** $c_{p,0}$ **[J kg^{-1}K^{-1}]**
LPCVD SiN	70.20	72.03	3100	700
LPCVD doped PolySi	9.06	6.99	2329	753
LPCVD PolySi	15.81	12.19	2329	753
TiN	4.92	8.80	5400	37
Equivalent			3021.39	651.84

Table 7.12: Thermal properties of a 200μm pixel of the high temperature process.

7.7.4 Mechanical Design

In this section we will discuss the basic mechanical analysis of the detector. The structural integrity of the encapsulation has already been discussed in section 7.7.2. Unlike the encapsulation, the detector will not be subjected to a static load. Therefore we will only look at its behavior under a shock load and vibrations.

Shock load

The shock load is calculated assuming a double sided clamped beam, which may have a maximum deflection of 2.4μm. For the high temperature design we therefore have:

$$I = \frac{W \times t^3}{12} = \frac{200 \cdot 10^{-6} \times (3.11 \cdot 10^{-6})^3}{12} = 4.99 \cdot 10^{-22} \text{ [m}^4\text{]} \tag{7.91a}$$

$$q_{max} = \frac{384 \times 2.40 \cdot 10^{-6} \times 3.00 \cdot 10^{9} \times 4.99 \cdot 10^{-22}}{(3.50 \cdot 10^{-3})^4} = 9.20 \cdot 10^{-6} \text{ [N/m]} \tag{7.49}$$

$$a_{max} = \frac{9.20 \cdot 10^{-6} \times 3.50 \cdot 10^{-3}}{5.22 \cdot 10^{-9}} = 6.17 \text{ [m s}^{-2}\text{]} \tag{7.50}$$

And for the low temperature design:

$$I = \frac{W \times t^3}{12} = \frac{200 \cdot 10^{-6} \times (3.42 \cdot 10^{-6})^3}{12} = 6.68 \cdot 10^{-22} \text{ [m}^4\text{]} \tag{7.92a}$$

$$q_{max} = \frac{384 \times 2.40 \cdot 10^{-6} \times 3.00 \cdot 10^{9} \times 6.68 \cdot 10^{-22}}{(3.50 \cdot 10^{-3})^4} = 12.3 \cdot 10^{-6} \text{ [N/m]} \tag{7.49}$$

$$a_{max} = \frac{12.3 \cdot 10^{-6} \times 3.50 \cdot 10^{-3}}{5.75 \cdot 10^{-9}} = 7.49 \text{ [m s}^{-2}\text{]} \tag{7.50}$$

Eigen frequency

Assuming again a double sided clamped beam, the eigen frequency for the high temperature process detector is calculated by:

$$\omega = 22.74\sqrt{\frac{3.00 \cdot 10^{9} \times 4.99 \cdot 10^{-22}}{3001.4 \times 46 \cdot 10^{-6} \times 3.11 \cdot 10^{-6} \times (3.5 \cdot 10^{-3})^4}} = 1860 \text{ [rad s}^{-1}\text{]} = 296 \text{ [Hz]} \tag{7.51}$$

and for the low temperature process detector by:

$$\omega = 22.74\sqrt{\frac{3.00 \cdot 10^{9} \times 4.99 \cdot 10^{-22}}{2476.0 \times 46 \cdot 10^{-6} \times 3.42 \cdot 10^{-6} \times (3.5 \cdot 10^{-3})^4}} = 1772 \text{ [rad s}^{-1}\text{]} = 282 \text{ [Hz]} \tag{7.51}$$

7.7.5 Simulated Performance

All the designs have been simulated and their performance characteristics displayed in tables 7.13 and 7.14. The values are in the same order as those found in literature and may therefore be considered as reasonable approximations. Further model validation will of course be discussed in the experimental results section (9.1).

Although the responsivity is not particularly high, it obviously is still useful to have bigger pixels since they will absorb more power as shown earlier in figure 7.16(b) and therefore will have higher output voltages. Of course the big pixels will be at the cost of a relatively slow response, but this is not considered to be of big concern in this particular application. Moreover, as also already shown earlier (figure 7.16(a)), bigger pixels will also worsen the spectral resolution. Therefore it is thought at this moment that one of these detector setups presented in these tables will be best for this application.

7.8 Fabrication

Fabrication is done at the Delft Institute of Microsystems and Nanoelectronics (DIMES). A simplified and highly schematic illustration of the process is shown in figure 7.25.

As said in previous sections, the process is divided into two parts: A non-CMOS compatible high temperature part and a CMOS compatible low temperature part. The main difference is that the high temperature process continues after step 6 as shown in figure 7.25, whereas the low temperature process will only be sacrificially etched after step 6.

The material used in the metallization step is dependent on which of the two processes is being conducted. For the low temperature process we can use Aluminium (Al), whereas the high temperature process will use Titanium Nitride (TiN). We have to go for a different material, because Al has a melting point of 660°C, while the LPCVD Silicon Nitride (SiN) is deposited at 850°C.

To reduce any chance on stiction, the sacrificial etching is performed using vaporized HydroFluoric (HF) acid. The sacrificial material is chosen to be TEOS SiO_2. This was thought to result in an etch selectivity of about 1000:1 to the SiN. Only later this selectivity proved much lower. Exact etch rates can be found in chapter 9 and appendix A. The vapour HF setup is shown in figure 7.26.

A detailed flowchart of the fabrication process can be found in appendix B

Parameter	**Design 1a**	**Design 2a**	**Design 3a**
Pixel width [μm]	100	150	200
Pixel length [μm]	3500	3500	3500
Absorber length [μm]	3090	3090	3090
No. of Thermocouple pairs	15	21	26
Thermal Conductance[W K^{-1}]	$3.91{\cdot}10^{-5}$	$5.87{\cdot}10^{-5}$	$7.82{\cdot}10^{-5}$
Thermal Capacitance [J K^{-1}]	$9.09{\cdot}10^{-7}$	$1.36{\cdot}10^{-6}$	$1.81{\cdot}10^{-6}$
Thermal Time constant [ms]	23	23	23
Sensitivity [μVK^{-1}]	290	290	290
DC Responsivity [V/W]	111	104	96
Detectivity [cm Hz$^{1/2}$ W^{-1}]	$1.56{\cdot}10^{8}$	$1.50{\cdot}10^{8}$	$1.45{\cdot}10^{8}$
Operating pressure [mTorr]	200	200	200
Material	p-n PolySi	p-n PolySi	p-n PolySi
CMOS compatible	no	no	no
Impedance @ T=298K [kΩ]	95	133	165
Absorber type	Thin-Film	Thin-Film	Thin-Film
Mean absorption [%]	94	94	94
Detection band [μm]	3-5	3-5	3-5
Releasing process	Surface MM	Surface MM	Surface MM

Table 7.13: Simulated key parameters of the designed thermopile detectors for the high temperature process.

Parameter	**Design 1b**	**Design 2b**	**Design 3b**
Pixel width [μm]	100	150	200
Pixel length [μm]	3500	3500	3500
Absorber length [μm]	3090	3090	3090
No. of Thermocouple pairs	15	21	26
Thermal Conductance [W K^{-1}]	$2.66{\cdot}10^{-5}$	$3.99{\cdot}10^{-5}$	$5.32{\cdot}10^{-5}$
Thermal Capacitance [J K^{-1}]	$1.40{\cdot}10^{-6}$	$2.10{\cdot}10^{-6}$	$2.79{\cdot}10^{-6}$
Thermal Time constant [ms]	53	53	53
Sensitivity [μVK^{-1}]	290	290	290
DC Responsivity [V/W]	163	153	142
Detectivity [cm Hz$^{1/2}$ W^{-1}]	$2.29{\cdot}10^{8}$	$2.21{\cdot}10^{8}$	$2.13{\cdot}10^{8}$
Operating pressure [mTorr]	200	200	200
Material	p-n PolySi	p-n PolySi	p-n PolySi
CMOS compatible	yes	yes	yes
Impedance @ T=298K [kΩ]	95	133	165
Absorber type	Thin-Film	Thin-Film	Thin-Film
Mean absorption [%]	98	98	98
Detection band [μm]	3-5	3-5	3-5
Releasing process	Surface MM	Surface MM	Surface MM

Table 7.14: Simulated key parameters of the designed thermopile detectors for the low temperature process.

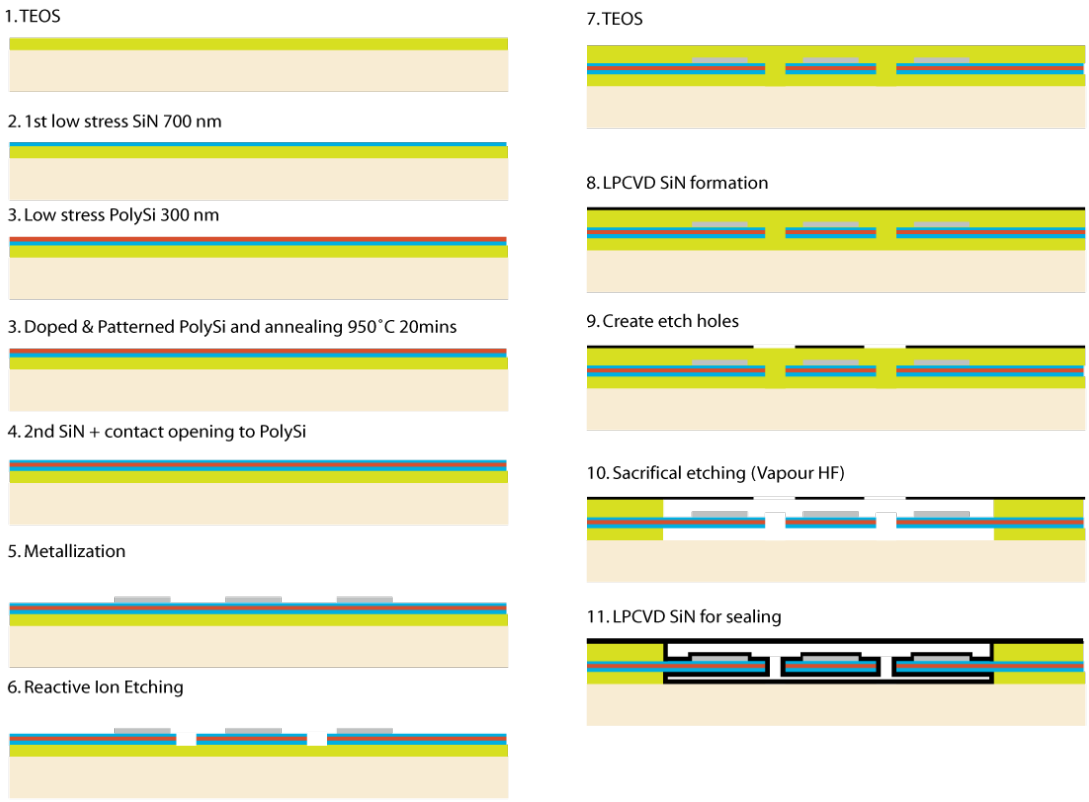

Figure 7.25: Schematic illustration of the EI1704 process

Figure 7.26: Photo's of the vapour HF setup. Left: Complete setup; Top Right: Setup during preparation; Bottom Right: Setup during etching.

Chapter 8

System integration

8.1 Integration with the LVOF

To be able to integrate the Linear Variable Opitical Filter with the detector chip, one could either try to deposit the LVOF directly on top of the encapsulation. However, because we chose to fabricate detectors both with and without encapsulation, we fabricated the LVOF on a separate die. This may then be bonded on top of the detector chip with adhesive wafer bonding as shown in figure . The argument of low transmittance through the thick slab of silicon, used earlier, becomes invalid if the LVOF is deposited on top, because the low transmittance is only due to reflection and not absorption.

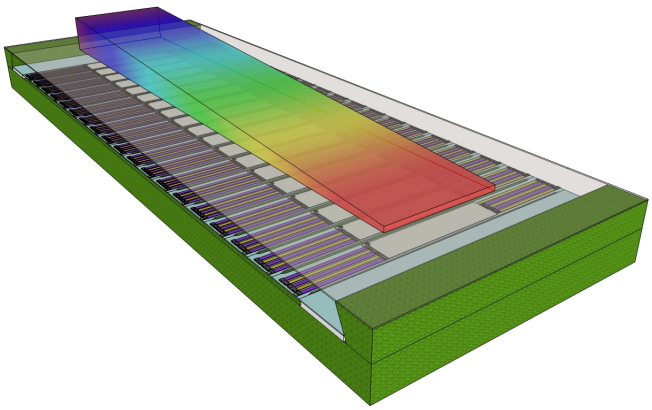

Figure 8.1: Impression of the integration of the LVOF on top of the detector array. (not to scale)

Similar chips could be created with the pass-band filters which can for example be mounted on the source or on top of the LVOF. An even better solution might be the deposition of the filters on the bottom side of the LVOF chip. Although this side will have a recession etched into it, this is still possible, because there is no need for any lithographic steps. However, one should take into account that the surface of the recession might be quite rough due to the etching.

8.2 Read-out circuitry

A simple read-out circuit is designed to allow for the measurements and characterization of the detector. Figure 8.2 shows the circuit for a single pixel. Because of the many pixels, a double stage multiplexing system is used. The first stage uses 6 3-bit multiplexers and the second stage another 2. To be able to fit in the vacuum chamber the circuit had to be divided over two separate circuit boards. The complete circuit including the board designs can be found in appendix C.

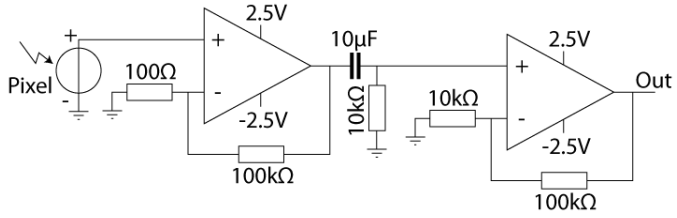

Figure 8.2: Schematic of the read-out of a single pixel.

Chapter 9

Results and Evaluation

This chapter will discuss the different measurements that have been conducted, including the setups used. Some measurements are conducted on the wafer. For these measurements every die on the wafer will be identified according to their number shown in figure 9.1. Any wafer number will correspond to those shown in the detailed process flowchart in appendix B. Unfortunately the fabrication process has been delayed more than 2 months and is still not finished at the moment of writing. For the biggest part this is due to inoperable machines like the Novellus (PECVD) and stepper machine. Therefore not as many results can be presented as was hoped for.

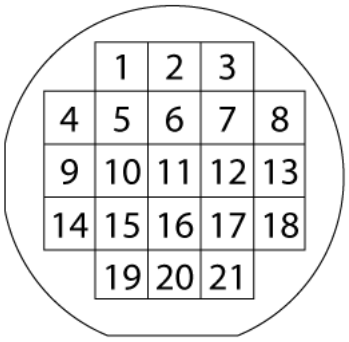

Figure 9.1: Identification numbers of the dies while on the wafer

9.1 Model validation

Because of all the delays, no detector has been fully fabricated. It was therefore impossible to validate the design, and therefore the model, with these detectors. However, earlier conducted research by Wu [131] did produce detectors which are similar enough to be able to have their performance simulated. The detector part of the model is therefore validated using these detectors as shown in table 9.1. Further research will have to validate the rest of the model.

Although the values do not match exactly, the model is still considered a valid tool for first approximation during the design of a detector. The fact that it is underestimating the perfor-

Parameter	Measured Value	Simulated Value
Element dimension [μm^2]	650x36	650x36
Pitch [μm]	46	46
Number of Thermocouples	5	5
Sensitive area [μm^2]	282x36	282x36
Thermopile resistance [kΩ]	31	28
Operating in air		
Responsivity [V/W]	21	16.6
Specific detectivity D* [cm $Hz^{1/2}$ W^{-1}]	$9.346 \cdot 10^6$	$7.74 \cdot 10^6$
Time constant [ms]	0.537	0.488
Operating in vacuum (1 mbar)		
Responsivity [V/W]	294.7	147.3
Specific detectivity D* [cm $Hz^{1/2}$ W^{-1}]	$131 \cdot 10^6$	$69.5 \cdot 10^6$
Time constant [ms]	4.85	4.3

Table 9.1: Comparison between measured and simulated values.

mance of the detector will in the end only result in better system performance than expected. Further refinement of the assumptions made, may result in even better approximations. These include for example the emissivity factors of both the beam and absorber, which are currently set to 0.29 and 1 respectively.

9.2 Fabrication Results

To have more design input for future research, a lot of effort has been put into trying to characterize the fabrication process as much as possible. It was found that many problems may be encountered during the process. Those that were encountered will be presented here, including theories on the cause and suggested solutions.

9.2.1 Sacrificial etching

The etch rate of the sacrificial TEOS SiO_2 is of course of great importance. Therefore several tests have been performed to characterize this etch rate, the conclusions of which are reported in table 9.2. Wafers with several different layers have been used, though all had a sacrificial layer of 4μm thick TEOS SiO_2. On top of this sacrificial layer there was at least an LPCVD SiN layer of several hundred nanometers thick which was acting as the membrane that we wanted to release. After sacrificial etching the dies were successfully cleaned using a vacuum hotplate at 250°C and minimum pressure (about 1mbar) for 1 hour to sublimate all the residues.

Several interesting things were found about the uniformity of the etching. We saw, for

Wafer number	**Anneal Temp. [°C]**	**Etch Temp. [°C]**	**HF Conc. [%]**	**Distance to sample [cm]**	**Etch time [min]**	**Under etch [μm]**	**Etch rate [nm min^{-1}]**
T	950	wet	73	-	14.17	37.5	2647
T	850	30	40	2.5	12	18	1500
T	850	30	40	2.5	35	47	1350
10	950	30	40	2.5	22	9	409
10	950	29	40	2.5	30	12.2	405
10	950	27	40	2.5	15	9.6	640
10	950	27	40	2.5	50	22	440
10	950	27	40	2.5	75	29	387
10	950	25	40	2.5	15	9	600
10	950	42	73	1.9	20	18	900
10	950	42	73	1.9	38	30	789
10	950	42	73	1.9	45	>30	
10	950	42	73	1.9	50	$\gg$30	
10	950	38	73	1.9	20	19	955
10	950	35	73	1.9	13.5	24	1778
10	950	30	73	1.9	13.5	30	2222
10	950	30	73	1.9	15	35	2333

Table 9.2: Average etch rates of different types of SiO_2 (TEOS) in both vapour and liquid HF. 0.5L was used for 40% vapour HF and 0.2L for 73% vapour HF. T = Test wafer.

example, that for higher temperatures, the etch front was showing more and more interference fringes as can be seen clearly in figure 9.2. This is thought to indicate that the etch front is faster at the top than the bottom due to a temperature gradient, resulting in a non-vertical slope. It would therefore be required to have more over etch at higher temperatures to account for this non-uniformity.

At one point also the lateral uniformity degraded significantly as shown in figure 9.3. However, no clear indication of process dependency was found. It might have just been dirt preventing the etchant to enter the etch holes.

One of the wafers (#10) had Carbon Nano Tubes (CNT's) deposited on top of the membrane. This process did not include a protection layer for the Ti/TiN interconnect layer. Because the Ti is only 40 nm thick, it is etched away quite fast. How fast is very much depending on the HF concentration and temperature. Once the Ti is gone, the TiN is free floating and will therefore break up in many pieces as shown in figure 9.4.

Increasing both the HF concentration and the temperature significantly improved the metal condition, but did still not prevent cracking. Because of stress concentration, the most severe cracks originate from sharp corners as shown in figure 9.5, resulting in detached interconnect lines from the bond pad.

9.2.2 Buckling or stiction

After sacrificial etching we noticed that many, if not all, released devices were in contact with the substrate as shown in figure 9.6. Because the etching is performed using vapour in stead of

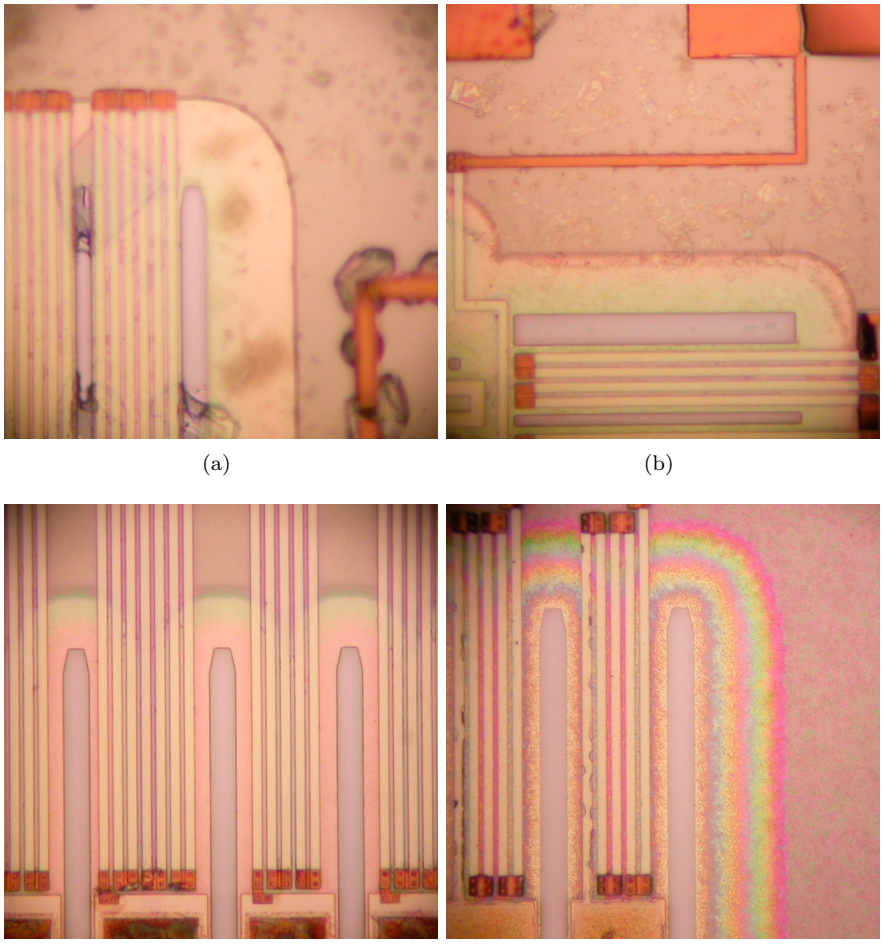

(a) (b)

(c) (d)

Figure 9.2: Vertical etch uniformity for 73% vapour HF at a) 30°C, b) 35°C, c) 38°C and d) 42°C.

a liquid, stiction (i.e. substrate contact due to capillary forces of fluids) was not considered the most prominent suspect. Another option would be that residual stresses of the process causes the beam to buckle down. To verify this, a mathematical analysis is performed using a slightly simplified structure as shown in figure 9.7. Using equations (7.43) to (7.46) we can write:

$$\int_1 z_1 \mathrm{d}A = z_1 A_1 = (h_1 - 50 \cdot 10^{-9}) 3 \cdot 10^{-3} \times 100 \cdot 10^{-9} \tag{9.1a}$$

$$\int_2 z_2 \mathrm{d}A = z_2 A_2 = (h_1 - 100 \cdot 10^{-9} - 150 \cdot 10^{-9}) 3 \cdot 10^{-3} \times 300 \cdot 10^{-9} \tag{9.1b}$$

$$\int_3 z_3 \mathrm{d}A = z_3 A_3 = -(1.1 \cdot 10^{-6} - h_1 - 350 \cdot 10^{-9}) 3 \cdot 10^{-3} \times 700 \cdot 10^{-9} \tag{9.1c}$$

Which results in:

$$h_1 = \frac{0.1 \cdot 10^{-17} E_1 + 1.5 \cdot 10^{-17} E_2 + 10.5 \cdot 10^{-17} E_3}{2 \cdot 10^{-11} E_1 + 6 \cdot 10^{-11} E_2 + 14 \cdot 10^{-11} E_3} = 587 \cdot 10^{-9} \text{ [m]} \tag{9.2}$$

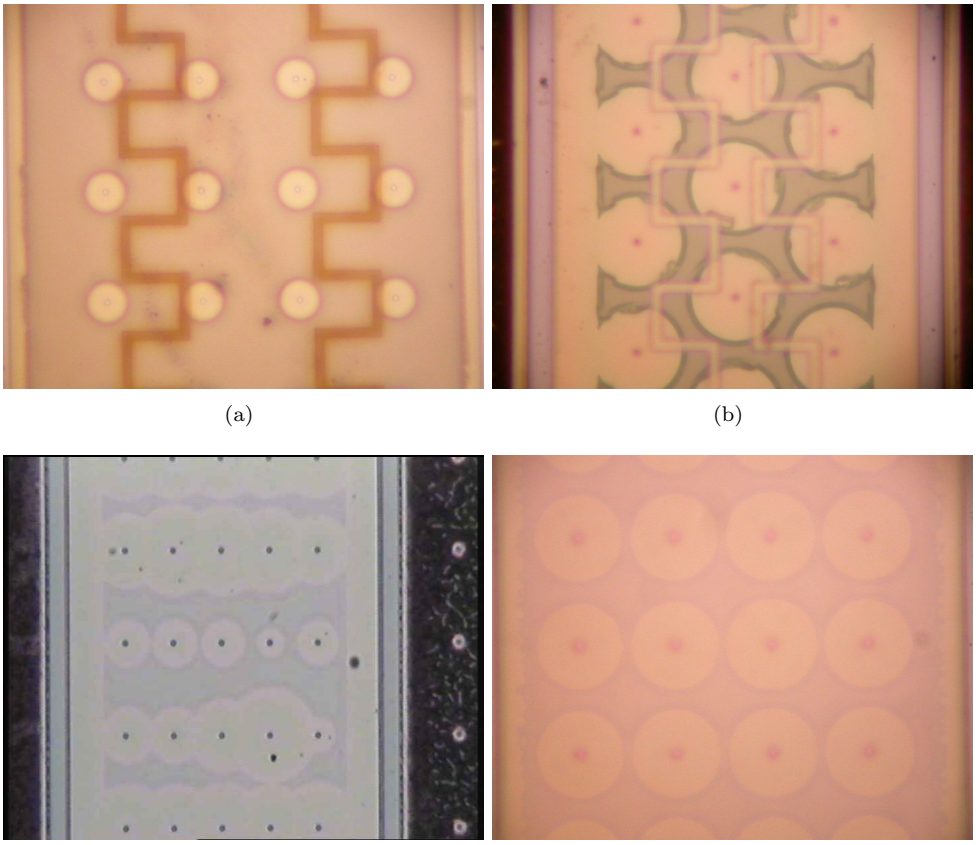

(a) (b)

(c) (d)

Figure 9.3: Lateral etch uniformity for a) 40% vapour HF at 25°C, b) 40% at 30°C, c) 73% at 38°C and 73% at 42°C.

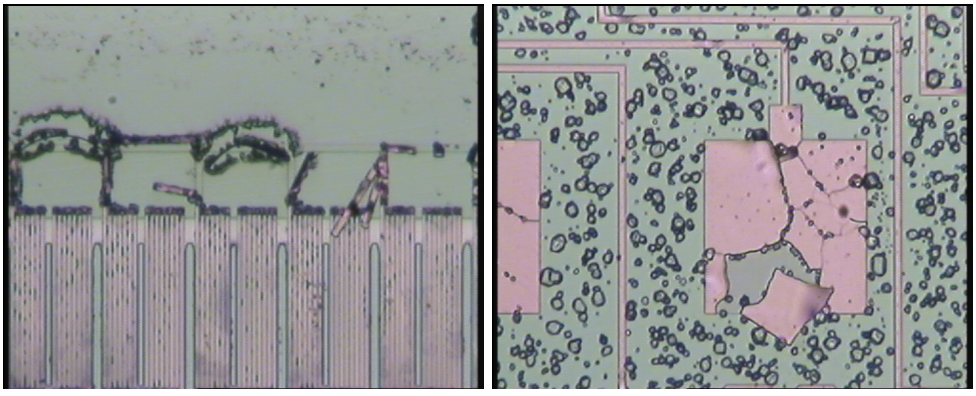

(a) (b)

Figure 9.4: Broken interconnect lines (a) and bond pad (b) after sacrificial etching with 40% vapour HF (there seems to be no significant dependence on time and temperature).

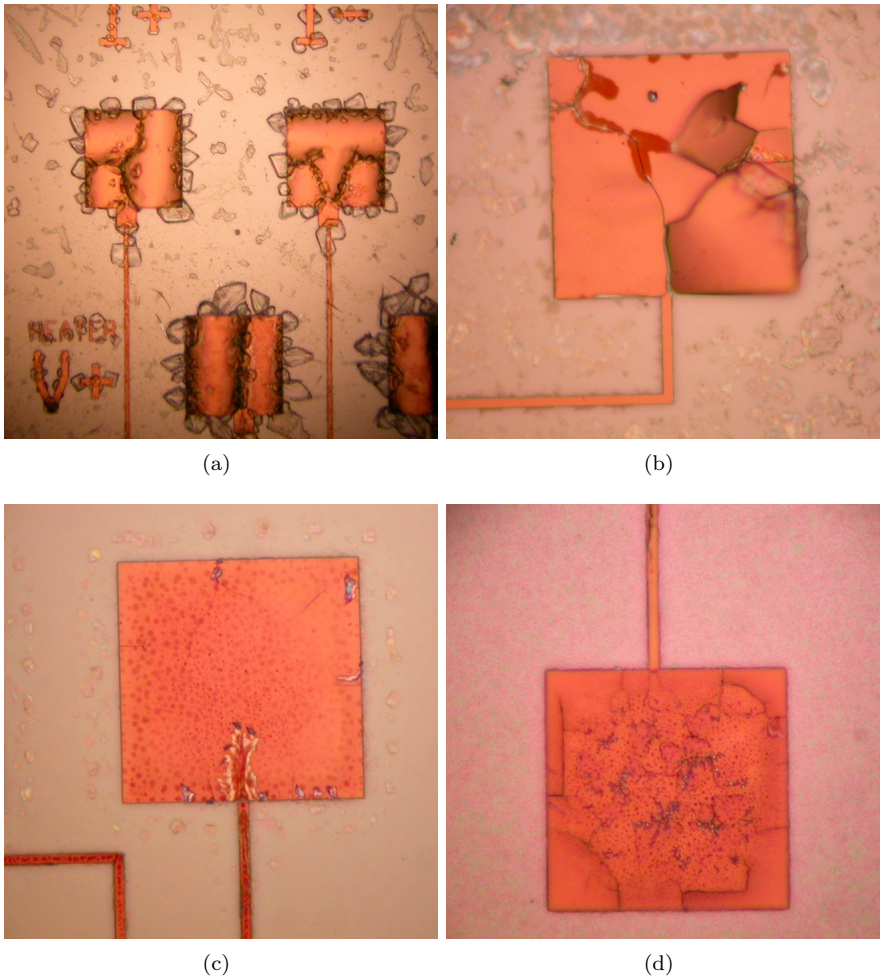

(a) (b)

(c) (d)

Figure 9.5: Ti/TiN after etching with 73% vapour HF at a) 30°C, b) 35°C, c) 38°C and d) 42°C.

where $E_1 = E_3 = 235$ GPa and $E_2 = 140$ GPa.

We can now define:

$$I_{eff,1} = \frac{b}{12}t_1^3 + bt_1z_1^2 = 5.79 \cdot 10^{-24} \text{ [m}^4\text{]} \tag{9.3a}$$

$$I_{eff,2} = \frac{b}{12}t_2^3 + bt_2z_2^2 = 7.27 \cdot 10^{-24} \text{ [m}^4\text{]} \tag{9.3b}$$

$$I_{eff,3} = \frac{b}{12}t_3^3 + bt_3z_3^2 = 9.43 \cdot 10^{-24} \text{ [m}^4\text{]} \tag{9.3c}$$

$$EI = E_1I_{eff,1} + E_2I_{eff,2} + E_3I_{eff,3} = 4.59 \cdot 10^{-12} \text{ [Nm}^2\text{]} \tag{9.3d}$$

Resulting in a critical stress for the 3500μm long and 200μm wide bridge of:

$$\sigma_{crit} = \frac{P_{crit}}{A} = \frac{\pi^2 EI}{AL_{eff}^2} = 6.73 \cdot 10^4 \text{ [Pa]} \tag{9.4}$$

And for a 500μm long and 200μm wide bridge of:

$$\sigma_{crit} = \frac{P_{crit}}{A} = \frac{\pi^2 EI}{AL_{eff}^2} = 3.30 \cdot 10^6 \text{ [Pa]} \tag{9.5}$$

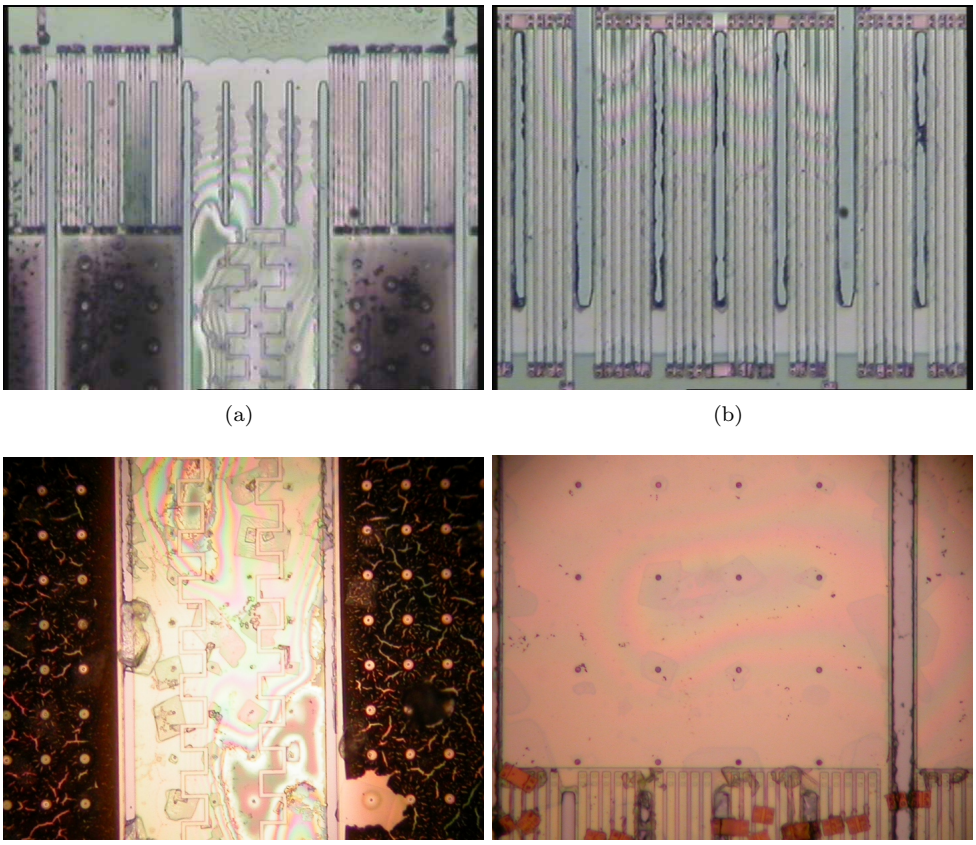

(a) (b)

(c) (d)

Figure 9.6: Rainbow patterns indicating contact between the membrane and the substrate. a) and b) were both etched with 40% vapour HF at 30°C and c) and d) with 73% at 30°C.

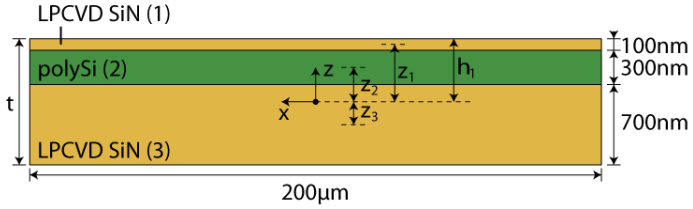

Figure 9.7: Cross-section of a simplified bridge structure for buckling calculation.

Because SiN will have a tensile residual stress, the buckling would only occur if the polySi layer has a compressive stress which is high enough to overcome both this tensile stress and

the critical stress required to buckle. Although this might seem possible for the long beam, it definitely seems unlikely for the short one.

Further reasoning gave us the idea that the temperature of the wafer may still be low enough for water to condensate on the devices, resulting in stiction anyhow, even though we are using vapour etching. Increasing the temperature to 35°C or above seemed to remove the stiction effect, supporting our theory. However, of course the higher temperature will come at the cost of a lower etch rate.

9.2.3 Etching of SiN

To still have the required 30μm of under etch, the etch time had to be increased significantly up to the point where the bridges broke because the SiN membrane was etch away completely as shown in figure 9.8. This lead us to investigate the etch rate of SiN for different etch conditions. These results are presented in table 9.3.

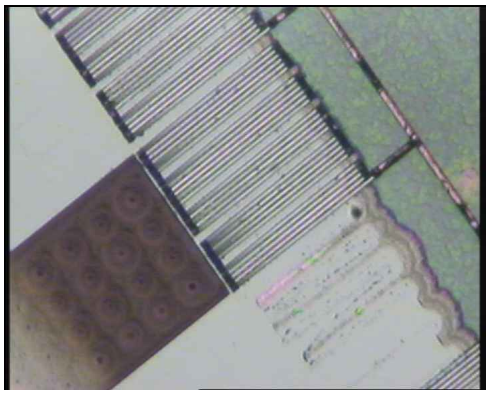

Figure 9.8: No LPCVD SiN membrane left after 45 min of etching in 73% vapour HF at 42°C. The black part is the Carbon Nanotube absorber, being completely detached from the polysilicon thermopile.

Deposition Technique	**Etch Temp. [°C]**	**HF Conc. [%]**	**Distance to sample [cm]**	**Etch time [s]**	**Etch depth [nm]**	**Etch rate [nm min^{-1}]**
LPCVD	30	40	2.5	2100	49	1.4
LPCVD	42	73	1.9	150	26	10.4
LPCVD	42	73	1.9	300	60	12
LPCVD	35	73	1.9	180	28	9.3
LPCVD	wet	73	1.9	150	9	3.6
PECVD	42	73	1.9	5	54	648
PECVD	42	73	1.9	10	76	456
PECVD	35	73	1.9	10	98	588
PECVD	wet	73	1.9	10	97	582

Table 9.3: Etch rates of different types of SiN in both vapour and wet HF.

If we compare tables 9.2 and 9.3, we identify the selectivity of PECVD TEOS SiO_2 annealed at 950°C to LPCVD SiN to be only about 75:1 for etching at 42°C with 73% vapour HF. This

means that when we would like to have an under etch of 30μm, we would remove 500 nm of SiN. Wafer #10 only had a 700 nm thick membrane with a 100 nm thick protection layer and the etchant can attack from both sides, the SiN will thus be gone completely, supporting our earlier findings. Lowering the temperature to 35°C would increase the selectivity to about 200:1.

Even worse is the selectivity of this TEOS to PECVD SiN, which for 73% vapour HF at 35°C is just about 3:1. It will therefore be impossible to do the sacrificial etching of the low temperature wafers by means of vapour HF!

40% vapour HF will do a little better with about 300:1. Wet etching in 73% HF will have the best selectivity of about 700:1. However, as discussed earlier, the 40% vapour HF will show significantly more damage to the Ti and wet etching will result in a complex process to prevent stiction.

9.2.4 Cracking & blistering

During deposition of the encapsulation layers, cracks and blisters started to appear, as shown in figure 9.9. After inspection this is thought to be caused by the TiN bottom reflector. During the LPCVD step at 850°C the stresses in the TiN will be released, causing the failures. Measurements have been conducted on the stresses in the TiN layers using a Tencor Flexus thin-film stress analyser and are presented in table 9.4.

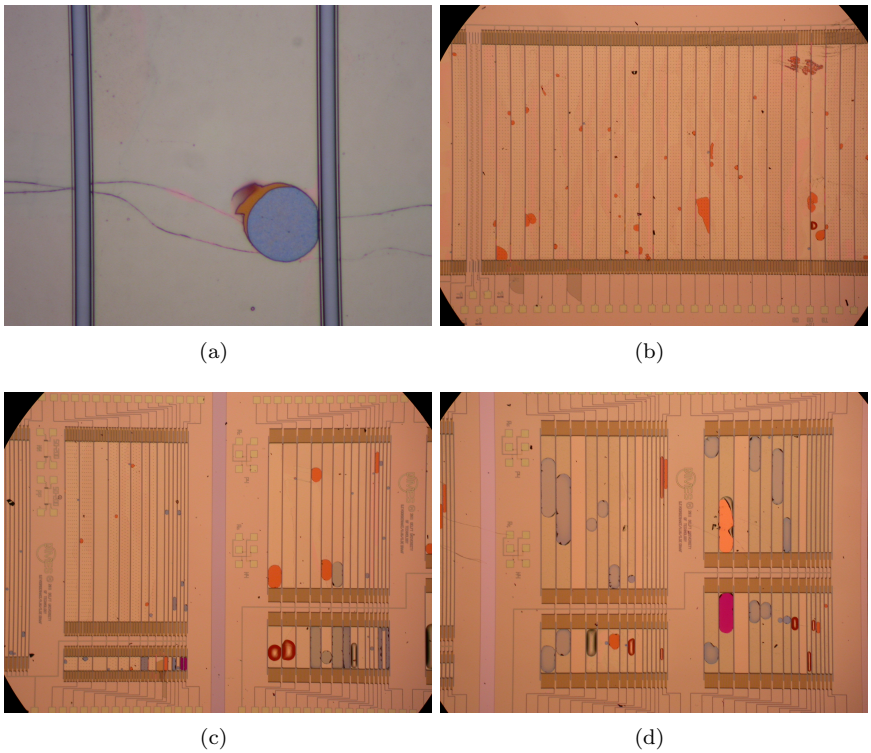

(a) (b)

(c) (d)

Figure 9.9: Cracked and blistered absorbers after 2μm of LPCVD TEOS deposition.

It is also possible to use a low-stress recipe as reported by Creemer [146]. A test has been

Material	Thickness [nm]	Stress [MPa]	Type
TiN	134	1592	Tensile
TiN	25	170	Tensile

Table 9.4: Measured resulting stresses after processing.

performed on this recipe (also 150 nm) by annealing it at 850°C. By looking at Scanning Electron Microscope (SEM) images, as shown in figure 9.10, no real difference in the grain size or structure can be found between the samples before and after annealing. It is therefore proposed to use this recipe instead of the standard one when TiN is used in thick layers.

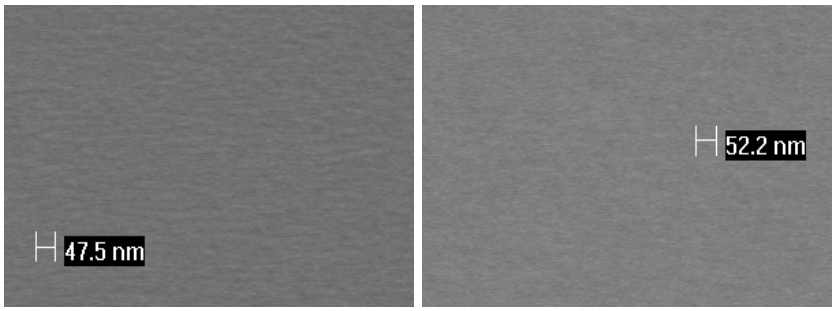

(a) (b)

Figure 9.10: SEM images of low stress Titanium Nitride grain size a) before annealing and b) after annealing.

9.3 Contact resistance

The contact resistance between the PolySi and the metal (Ti/TiN or Al dependent on the process) was measured before sacrificial etching using a four point measurement structure as shown in figure 9.11. The instrument used is an HP 4145B Semiconductor Parameter Analyzer which is setup as shown in table 9.5. The measured voltage is calculated as V4-V1. The results are shown in figure 9.12. From these results we can conclude that the contact resistance of n-type polySi to the Ti/TiN metal is averaged around 28 Ω, whereas the p-type polySi will have an average of about 42 Ω. It can also be seen that the centre die (#11) has the smallest spread from wafer to wafer.

9.4 Sheet resistance

The sheet resistances of the n-type and p-type PolySi are measured using a four point measurement structure as shown in figure 9.13 and an HP 4145B Semiconductor Parameter Analyzer which is setup as shown in table 9.6, where the measured voltage is calculated as V4-V2. The results are shown in figure 9.14. From these results we can conclude that the sheet resistance

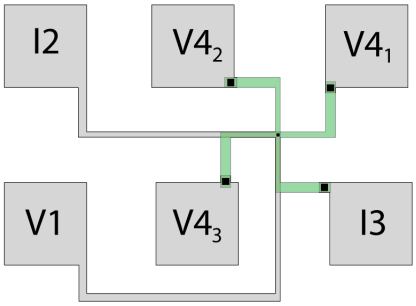

Figure 9.11: Illustration of the device created to measure the contact resistance between the PolySi and metal

(a)

	Name		Source	
Chan	**V**	**I**	**Mode**	**Fntn**
SMU1	V1	I1	I	Const
SMU2	V2	I2	COM	Const
SMU3	V3	I3	I	Var1
SMU4	V4	I4	I	Const

(b)

	Var1
Name	I3
Sweep mode	Linear
Start	-1.000mA
Stop	1.000mA
Step	100.0μA
No. Of Step	21
Compliance	10.000 V

Table 9.5: HP 4145B Channel Definition and Source Set up for the contact resistance measurement

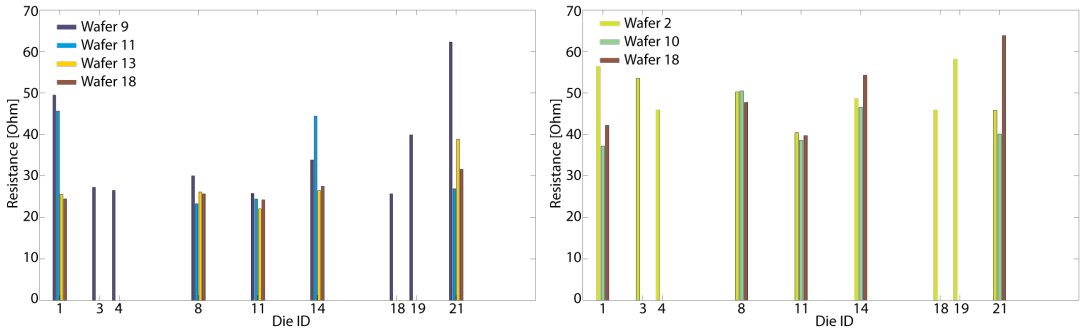

(a) (b)

Figure 9.12: Results of the contact resistance measurements for a) N-type and b) P-type polySi

of n-type polySi is averaged around 56 Ω/□, whereas the p-type polySi will have an average of about 115 Ω/□.

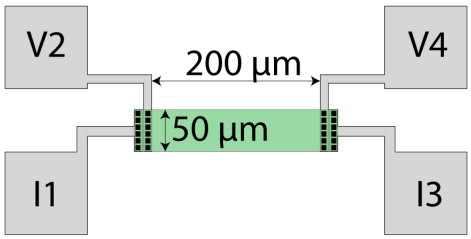

Figure 9.13: Illustration of the device created to measure the sheet resistance of the n-type and p-type PolySi

(a)

	Name		Source	
Chan	**V**	**I**	**Mode**	**Fntn**
SMU1	V1	I1	COM	Const
SMU2	V2	I2	I	Const
SMU3	V3	I3	I	Var1
SMU4	V4	I4	I	Const

(b)

	Var1
Name	I3
Sweep mode	Linear
Start	-1.000mA
Stop	1.000mA
Step	100.0μA
No. Of Step	21
Compliance	10.000 V

Table 9.6: HP 4145B Channel Definition and Source Set up for the sheet resistance measurement

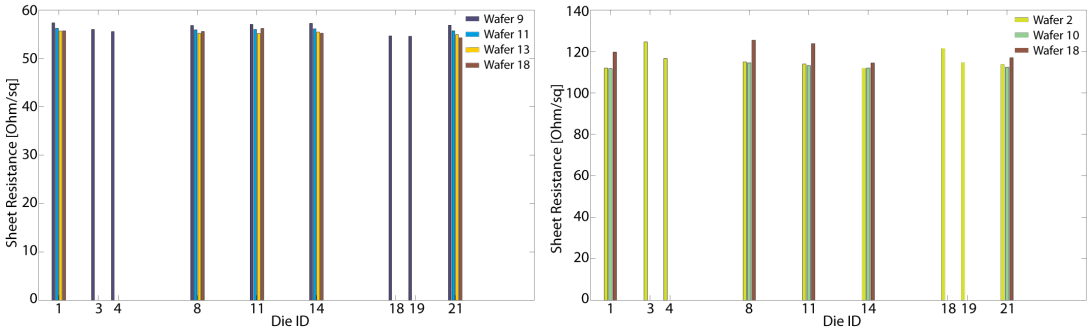

(a) (b)

Figure 9.14: Results of the sheet resistance measurements for a) N-type and b) P-type polySi

9.5 Device measurements

9.5.1 LVOF

Several of the fabricated LVOF's have been characterized using a Nicolet 5700 FTIR spectrometer and a 250μm pinhole to reduce the spot size. The LVOF's are 10mm long and have a triangular shape as was shown earlier in figure 6.20. Therefore it was only required to measure to the

midpoint of the LVOF. The results are shown in figure 9.15. The LVOF's were translated by means of an M4 screw, which was turned a half turn for every measurement resulting in a step of 0.35 mm.

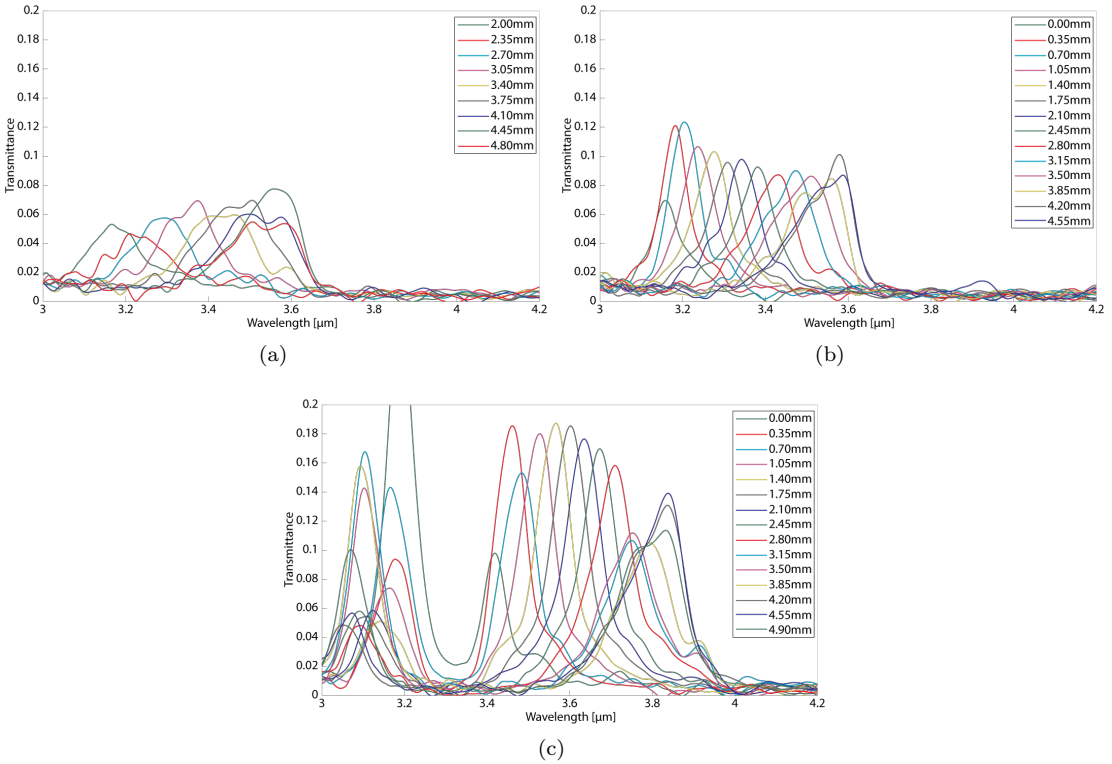

Figure 9.15: Three LVOF transmittance plots with taper angles of about a) 4.4 mdeg b) 2.9 mdeg c) 2.9 mdeg. The data is smoothed using Matlab to clear-up the image.

Although the results clearly show the workings of the LVOF, the throughput is not as good as was expected from the simulations. It is yet unclear why. Surface roughness of the oxide layers is always of big concern, but this roughness should affect all wavelengths and the data shows that transmittance in some part of the spectrum is very close to 1.

It is clear that the pinhole does affect the measurement. By using a 250μm pinhole, there was still enough light incident on the LVOF to have a measurable signal, although somewhat noisy. A larger pinhole would only broaden and lower the peaks, a smaller one would not transmit enough power for this setup to get a measurable signal. Moreover, the 250μm is close to the pixel size of the designed detector. It should therefore give us a fair indication on what kind of optical signal to expect.

The cause of the peaks on the left side of figure 9.15(c) is yet a bit unclear, but could be due to higher order diffraction by the pinhole.

9.6 Results summary

Although the fabrication was successful for the bigger part, during etching quite a few problems occurred. We saw cracking of the metal layers, stiction of the pixels and very low etch selectivity between the sacrificial material and the membrane.

The metal cracking is probably solved by using low-stress TiN and by protecting the Ti interconnects. The stiction problem was solved by using etch temperatures higher than 35°C. However, this significantly reduces both the etch rate and selectivity as shown in table 9.7. Although vapour HF etching at 35°C might give just enough selectivity, it will definitely remove a significant amount of SiN, influencing the performance. If we just look at selectivity, wet etching would be preferred. However, wet etching will require a more elaborate process like freeze drying to prevent stiction.

Material	**Etch rate in 73% vapour HF @ 42°C**	**Etch rate in 73% vapour HF @ 35°C**	**Etch rate in 40% vapour HF @ 30°C**	**Etch rate in 73% HF (wet)**
TEOS SiO_2	900 nm/min	1778 nm/min	409 nm/min	2647 nm/min
LPCVD SiN	12nm/min	9.3 nm/min	1.4nm/min	3.6 nm/min
Selectivity	75	191	292	735

Table 9.7: Summary of the etch selectivity of TEOS to LPCVD SiN for different etchants.

To have best of both worlds, it is also possible to partly etch the sample using a wet etch, put it on a hot plate to evaporate all the liquid and use vapour etching to remove the last part of the sacrificial layer.

Other measurements performed showed the contact and sheet resistances, which are summarized in table 9.8.

Contact resistance n-polySi - Ti/TiN	28 Ω
Contact resistance p-polySi - Ti/TiN	42 Ω
Sheet resistance n-polySi	56 Ω/□
Sheet resistance p-polySi	115 Ω/□

Table 9.8: Summary of the etch selectivity of TEOS to LPCVD SiN for different etchants.

Chapter 10

Conclusions and Outlook

The goal of this thesis was the design and development of an infrared absorption multi-gas micro-spectrometer for the measurement of the concentrations of Carbon Monooxide (CO), Carbon Dioxide (CO_2) and Hydro Carbons (C_xH_{2x+2}) in a composite gas. This includes mathematical modeling, design and fabrication.

The final goal is to create a gas composition sensor which should become part of a system which will allow for the introduction of new gases, like hydrogen and bio-gas. These new gases will be introduced for further sustainability of the gas network.

This thesis is the first step to such a system from a measurement science point of view. The model and demonstrator developed for this thesis were meant to be used to answer several research questions, which should act as a ground work on which further research can be based.

What is the range of concentrations of the different components in the gas?

This question was not answered by physical research, as this is currently being done by KEMA. It was therefore only limited to a small literature study. However, as the research by KEMA is still in progress, the results, as presented in section 3.2, may be subject to change. Anyone further researching on the topic of this thesis is therefore advised to continue to ask for updated results.

What are the limitations, restrictions and tolerances in the production process?

The fabrication process was probably the most difficult to grasp, because of the many aspects involved. Obviously the fabrication process is very much dependent on the availability of both men and machine. Unfortunately I have to conclude that this availability has been a lot less than I would have initially guessed (and many people with me). Even with quite a big amount of extra time planned for fabrication, we were not able to fully fabricate a single device.

Besides the planning, process technology also requires a lot of experience in what can and cannot/will not be done within the facilities available. This thesis has shown many of the materials which suited the requirements, including their properties, which for the bigger part have been measured by myself. It has also been shown which materials are and are not compatible to be used in the same process. This incompatibility can be the result of physical properties, but also process properties or machine contamination. This results for example in the advice to use low-stress Titanium Nitride.

Finally it has been shown that the sacrificial etching step is the most critical step and that many problems may occur if not planned carefully. Any design flaws or fabrication errors will only

come to light at this point. On top of that the etching itself also requires thorough understanding of all materials used. It was found that PECVD SiN is not suitable as structural material if TEOS SiO_2 and HF are used as sacrificial material and etchant, respectively. Also it was found that vapour HF etching does not necessarily mean that stiction cannot occur.

What is the required spectral resolution, detectivity and sensitivity for proper concentration resolvability?

By using the system model, it has been shown that spectral resolution, detectivity and sensitivity is only a very small part of the list of requirements for proper concentration resolvability. Also very important are for example the length of the optical path and the read-out algorithm. Therefore no definite answer can be given to this question. However, the detectors designed seem all to be able to detect the gas concentrations to a fair amount of accuracy as presented in section5.5 . Further testing of these structures in several setups should still confirm this simulation. At least it has been made clear what all the dependencies are.

Is there any system that could theoretically satisfy these requirements?

Yes. As was said in the answer of the previous question, the model predicted that the detectors designed should be able to detect the gas concentrations accurately enough.

How much do all unknown parameters (e.g. material properties, production tolerances, etc.) influence the performance of the micro-spectrometer?

Throughout this thesis several simulations have been performed to get some insight into the sensitivity of a part to change in for example layer thickness. One example of this is the infrared absorber design. It has been shown that production tolerances are within the boundaries required for these devices.

Is the model developed accurate enough to predict system performance?

The only model validation performed was on the detector part. Although not 100% accurate, it does give good insight in what can be expected. Further refinement of some of the assumptions made, may result in even better approximations. Other parts of the model will have to be validated in subsequent research. It is expected that the largest error will be located in the part calculating the optical throughput of the system. This has not been the focus of this thesis and has therefore been implemented as a rough approximation.

By setting up the model in a very modular way, it becomes not only insightful, but also easy to adapt to any requirement.

Outlook

As this thesis was intended to be the ground work for many subsequent researches, it is almost impossible to write a complete outlook including all the possible future work. I will therefore highlight a view which seem important to me.

Further validate and fine tune the model

Micro-spectrometry is most definitely not restricted to gas composition sensing. It is expected that many more applications will benefit from such a device. However, all these applications

have different requirements. A properly set up model should be able to be a good design tool in any of these applications. It is therefore proposed that the model presented in this thesis should be further validated to identify any weaknesses. This knowledge can subsequently be used to adapt the model to the requirements stated for the particular application.

Complete a full gas measurement setup

Obviously it will be required to basically continue with the research performed in this thesis and get to a complete setup as a proof of concept. This research would be especially important to physically determine the best setup. As shown, the ability of the setup to measure the gas composition is dependent on many parameters which cannot be treated independently. A full scale setup is the only way to accurately determine the required parameters.

Optimized/Alternative detector designs

The detector design is thought to be a good first design, but can definitely be optimized further. The length of the beam supporting the thermopile was for example found to be somewhat short. Other things which may be further optimized are the amount of thermocouples in the thermopile and membrane thickness.

Although in this thesis there has been chosen to use a thermopile detector array which is contained in a vacuum by a thin-film encapsulation, this is not necessarily the setup with the best output. Other options may be very competitive, including bolometers and wafer bonding. More research into these topics may result in a more definite answer to which detector will give the best output.

Other very interesting topics to research are alternative absorber designs. These include Carbon Nanotubes, meta materials or a combination thereof. Definitely the spectral selectivity of the meta materials in combination with the high absorption of the CNT's seems the way forward, since it would exclude the need for a dispersive element.

Bibliography

[1] E. Jurdík, J. Turkstra, R. Otjes, T. Groot, and F. Bakker, "Sensors for new gases," report, Nederlandse Gasunie, 29 november 2004.

[2] EEP, "Europe's energy portal." `http://www.energy.eu/#depletion`, Lasted checked: september 2010.

[3] T. Klein, "Friese boer levert groen gas," *Reformatorisch Dagblad*, vol. 2 feb 2011, 2011.

[4] CBS, "Stroomdiagram energie voor nederland, 2009." `http://www.compendiumvoordeleefomgeving.nl/indicatoren/nl0201-Stroomdiagram-energie-voor-Nederland.html?i=6-40`, Lasted checked: September 2010.

[5] IEA, "Key world energy statistics 2010," tech. rep., 2010.

[6] M. aan de Brugh, "Importgas bedreigt nederlandse kwaliteit," *NRC*, vol. february, 3rd, p. 15, 2011.

[7] M. aan de Brugh, "Nieuw gas vergt dure aanpassing," *NRC*, vol. february, 3rd, p. 1, 2011.

[8] E. S. Barr, "Historical survey of the early development of the infrared spectral region," *American Journal of Physics*, vol. 28, no. 1, pp. 42–54, 1960.

[9] Caltech IPAC, "Discovery of infrared." `http://coolcosmos.ipac.caltech.edu/cosmic_classroom/ir_tutorial/discovery.html`, Lasted checked: May 2011.

[10] Wikipedia, "Joseph von Fraunhofer." `http://en.wikipedia.org/wiki/Joseph_von_Fraunhofer`, Lasted checked: March 2011.

[11] J. F. Mulligan, "Who were Fabry and Pérot?," *American Journal of Physics*, vol. 66, no. 9, pp. 797–802, 1998.

[12] Wikipedia, "W. W. Coblentz." `http://en.wikipedia.org/wiki/W._W._Coblentz`, Lasted checked: March 2011.

[13] R. C. Jaeger, *Introduction to Microelectronic fabrication*, vol. 5 of *Modular series on solid state devices*. Upper saddle River: Prentice Hall, 2nd ed., 2002.

[14] J. A. Kaplan, "45 years later, does moore's law still hold true?," *FoxNews.com*, vol. January 04, 2011.

[15] M. Strojnik and G. Paez, "Radiometry," in *Handbook of Optical engineering* (D. Malacara and B. J. Thompson, eds.), New York: Marcel Dekker, Inc., 2001.

[16] P. Schley, M. Jaeschke, and K. Altfeld, "New technologies for gas quality determination," in *22nd World Gas Conference*, (Tokyo), pp. 1–12, International Gas Union, 2003.

[17] GasUnie, "Summary: expected range of composition of future gases," 2010.

[18] G. de Graaf, *Mid-Infrared microspectrometer systems.* PhD thesis, Delft University of Technology, 2008.

[19] J. Spannhake, O. Schulz, A. Helwig, G. Miiller, and T. Doll, "Design, development and operational concept of an advanced mems ir source for miniaturized gas sensor systems," in *IEEE Sensors, 2005*, (Irvine, CA, USA), pp. 762–765, IEEE, 2005.

[20] M. Weber, P. Lerch, and P. Renaud, "Improved design for fast modulating IR sources," *Journal of Micromechanics and Microengineering*, vol. 7, no. 3, p. 210, 1997.

[21] D. A. Neamen, *Semiconductor Physics and Devices: Basic Principles.* New York: McGraw-Hill Higher Education, 3rd ed., 2003.

[22] A. Godard, "Infrared (2-12 μm) solid-state laser sources: a review," *Comptes Rendus Physique*, vol. 8, no. 10, pp. 1100–1128, 2007.

[23] A. Kosterev, G. Wysocki, Y. Bakhirkin, S. So, R. Lewicki, M. Fraser, F. Tittel, and R. F. Curl, "Application of quantum cascade lasers to trace gas analysis," *Applied Physics B: Lasers and Optics*, vol. 90, no. 2, pp. 165–176, 2008.

[24] C. Sirtori and J. Nagle, "Quantum cascade lasers: the quantum technology for semiconductor lasers in the mid-far-infrared," *Comptes Rendus Physique*, vol. 4, no. 6, pp. 639–648, 2003.

[25] K. L. Vodopyanov, "Mid-infrared optical parametric generator with extra-wide (3-19 μm) tunability: applications for spectroscopy of two-dimensional electrons in quantum wells," *J. Opt. Soc. Am. B*, vol. 16, no. 9, pp. 1579–1586, 1999.

[26] F. Rouessac and A. Rouessac, *Chemical Analysis: Modern Instrumentation Methods and Techniques.* Chichester: John Wiley & Sons Ltd., 2nd ed., 2007.

[27] W. Wolfe, "Spectrometers," in *Handbook of Optical engineering* (D. Malacara and B. J. Thompson, eds.), New York: Marcel Dekker, Inc., 2001.

[28] E. L. Dereniak and G. D. Boreman, *Infrared detectors and systems.* Pure and applied optics, Wiley & Sons, Inc., 1996.

[29] L. L. Gordley, B. T. Marshall, and D. Allen Chu, "Linepak: Algorithms for modeling spectral transmittance and radiance," *Journal of Quantitative Spectroscopy and Radiative Transfer*, vol. 52, no. 5, pp. 563–580, 1994.

[30] J. Fang, W. Liu, T. Zhang, and W. Feng, "Line-by-line trace gas absorption model and its application for ndir gas detection technology," vol. 6723, pp. 67232S–5, SPIE, 2007.

[31] L. S. Rothman *et al.*, "The hitran 2008 molecular spectroscopic database," *Journal of Quantitative Spectroscopy and Radiative Transfer*, vol. 110, no. 9-10, pp. 533–572, 2009.

[32] Spectral Calc, "Calculation of molecular spectra with the Spectral Calculator," 2011.

[33] E. E. Whiting, "An empirical approximation to the voigt profile," *Journal of Quantitative Spectroscopy and Radiative Transfer*, vol. 8, no. 6, pp. 1379–1384, 1968.

[34] D. Killinger and D. Plutov, *Hitran-PC 4.0: User Manual*. Ontar Corporation, 2009.

[35] C. Zender, "Radiative transfer in the earth system," 2010.

[36] NIST, "Nist chemistry webbook." `http://webbook.nist.gov/chemistry/`, 2011.

[37] J. White, "Long optical paths of large aperture," *Journal of the Optical Society of America*, vol. 32, pp. 285–288, 1942.

[38] D. R. Herriott and H. J. Schulte, "Folded optical delay lines," *Appl. Opt.*, vol. 4, no. 8, pp. 883–889, 1965.

[39] Thermo Scientific, "60*i*," 2011.

[40] MKS, "MultiGas^{TM} 2030," 2011.

[41] MKS, "Process Sense^{TM} ," 2011.

[42] S. H. Kong, *Infrared Micro-Spectrometer Based on a multi-slit grating*. PhD thesis, Delft University of Technology, 2002.

[43] S. Grabarnik, *Optical microspectrometer using imaging diffraction gratings*. PhD thesis, Delft University of Technology, 2009.

[44] Technikon Forschungs- und Planungsgesellschaft mbH, "MEMFIS Project." `http://www.memfis-project.eu`.

[45] M. Kraft, A. Kenda, T. Sandner, and H. Schenk, "MEMS-based compact FT-spectrometers - a platform for spectroscopic mid-infrared sensors," in *Sensors, 2008 IEEE*, pp. 130–133, 2008.

[46] A. Kenda, C. Drabe, H. Schenk, A. Frank, M. Lenzhofer, and W. Scherf, "Application of a micromachined translatory actuator to an optical FTIR spectrometer," in *MEMS, MOEMS, and Micromachining II* (H. Urey and A. El-Fatatry, eds.), vol. 6186, (Strasbourg, France), pp. 618609–11, SPIE, 2006.

[47] T. Sandner, C. Drabe, H. Schenk, A. Kenda, and W. Scherf, "Translatory MEMS actuators for optical path length modulation in miniaturized Fourier-transform infrared spectrometers," *Journal of Micro/Nanolithography, MEMS and MOEMS*, vol. 7, no. 2, pp. 021006–12, 2008.

[48] J. A. McKay, "Single and tandem fabry-perot etalons as solar background filters for lidar," *Appl. Opt.*, vol. 38, no. 27, pp. 5851–5858, 1999.

[49] G. A. Gary, K. S. Balasubramaniam, and M. Sigwarth, "Multiple etalon systems for the advanced technology solar telescope," vol. 4853, (Waikoloa, HI, USA), pp. 252–272, SPIE, 2003.

[50] N. Neumann, M. Ebermann, S. Kurth, and K. Hiller, "Tunable infrared detector with integrated micromachined fabry-perot filter," *Journal of Micro/Nanolithography, MEMS and MOEMS*, vol. 7, no. 2, pp. 021004–9, 2008.

[51] A. Emadi, H. Wu, S. Grabarnik, G. de Graaf, K. Hedsten, P. Enoksson, J. H. Correia, and R. F. Wolffenbuttel, "Fabrication and characterization of IC-compatible Linear Variable Optical Filters with application in a micro-spectrometer," *Sensors and Actuators A: Physical*, vol. 162, no. 2, pp. 400–405, 2010.

[52] Elster-Instromet, "Gas-Lab Q1 EN03," 2010.

[53] J. Kastner, "Online gas quality measurement technique based on optical and thermal gas properties," in *Natural gas quality, Energy measurement and Interchangeability*, (Chicago), Elster-Instromet, 2005.

[54] F. López, J. de Frutos, A. M. González, and A. Navarro, "Integrated optical filters for infrared electrooptical gas sensors," *Sensors and Actuators B: Chemical*, vol. 6, no. 1-3, pp. 170–175, 1992.

[55] F. López and J. de Frutos, "Multispectral interference filters and their application to the design of compact non-dispersive infrared gas analysers for pollution control," *Sensors and Actuators A: Physical*, vol. 37-38, pp. 502–506, 1993.

[56] J. de Frutos, J. M. Rodríguez, F. López, A. J. de Castro, J. Meléndez, and J. Meneses, "Electrooptical infrared compact gas sensor," *Sensors and Actuators B: Chemical*, vol. 19, no. 1-3, pp. 682–686, 1994.

[57] J. Meléndez, A. J. De Castro, F. López, and J. Meneses, "Spectrally selective gas cell for electrooptical infrared compact multigas sensor," *Sensors and Actuators A: Physical*, vol. 47, no. 1-3, pp. 417–421, 1995.

[58] Q.-l. Tan, W.-d. Zhang, C.-y. Xue, J.-j. Xiong, Y.-c. Ma, and F. Wen, "Design of mini-multi-gas monitoring system based on IR absorption," *Optics & Laser Technology*, vol. 40, no. 5, pp. 703–710, 2008.

[59] R. Rubio, J. Santander, J. Fonollosa, L. Fonseca, I. Gràcia, C. Cané, M. Moreno, and S. Marco, "Exploration of the metrological performance of a gas detector based on an array of unspecific infrared filters," *Sensors and Actuators B: Chemical*, vol. 116, no. 1-2, pp. 183–191, 2006.

[60] R. Rubio, J. Santander, L. Fonseca, N. Sabaté, I. Gràcia, C. Cané, S. Udina, and S. Marco, "Non-selective NDIR array for gas detection," *Sensors and Actuators B: Chemical*, vol. 127, no. 1, pp. 69–73, 2007.

[61] L. Fonseca, R. Rubio, J. Santander, C. Calaza, N. Sabaté, P. Ivanov, E. Figueras, I. Gràcia, C. Cané, S. Udina, M. Moreno, and S. Marco, "Qualitative and quantitative substance discrimination using a CMOS compatible non-specific NDIR microarray," *Sensors and Actuators B: Chemical*, vol. 141, no. 2, pp. 396–403, 2009.

[62] E. Kälvesten, T. Corman, M. Huiku, K. Weckström, P. Meriläinen, and G. Stemme, "A silicon IR-source and CO_2-chamber for CO_2 measurements," in *IEEE 11th International Workshop on Micro Electro Mechanical Systems*, (Heidelberg, Germany), 1998.

[63] J. Kwon, G. Ahn, G. Kim, J. C. Kim, and H. Kim, "A study on NDIR-based CO_2 sensor to apply remote air quality monitoring system," in *ICCAS-SICE, 2009*, pp. 1683–1687, 2009.

[64] ICx^{TM}Photonics, "SensorChip^{TM}CO_2 Sensor." `http://photonics.icxt.com/index.php?page=sensorchip`.

[65] G. Lammel, S. Schweizer, S. Schiesser, and P. Renaud, "Tunable optical filter of porous silicon as key component for a MEMS spectrometer," *Microelectromechanical Systems, Journal of*, vol. 11, no. 6, pp. 815–828, 2002.

[66] Wilksir, "InfraSpec VFA-IR Spectrometer," 2011.

[67] F. G. Nogueira, D. Felps, and R. Gutierrez-Osuna, "Development of an infrared absorption spectroscope based on linear variable filters," *Sensors Journal, IEEE*, vol. 7, no. 8, pp. 1183–1190, 2007.

[68] B. R. Wiesent, D. G. Dorigo, and A. W. Koch, "Limits of ir-spectrometers based on linear variable filters and detector arrays," in *Instrumentation, Metrology, and Standards for Nanomanufacturing IV* (M. T. Postek, ed.), vol. 7767, (San Diego, California, USA), pp. 77670L–6, SPIE, 2010.

[69] H. Hara, N. Kishi, and H. Iwaoka, "Silicon bolometer and micro variable infrared filter for CO_2 measurement," in *Optical MEMS, 2000 IEEE/LEOS International Conference on*, pp. 139–140, 2000.

[70] E. Hecht, *Optics*. Addison Wesley, 4th ed., 2002.

[71] C. Palmer, *Diffraction Grating Handbook*. Newport Corporation, 6th ed., 2005.

[72] K. Chaganti, I. Salakhutdinov, I. Avrutsky, and G. W. Auner, "A simple miniature optical spectrometer with a planar waveguide grating coupler in combination with a plano-convex lens," *Opt. Express*, vol. 14, no. 9, pp. 4064–4072, 2006.

[73] I. Avrutsky, K. Chaganti, I. Salakhutdinov, and G. Auner, "Concept of a miniature optical spectrometer using integrated optical and micro-optical components," *Appl. Opt.*, vol. 45, no. 30, pp. 7811–7817, 2006.

[74] S. Ura, F. Okayama, K. Shiroshita, K. Nishio, T. Sasaki, H. Nishihara, T. Yotsuya, M. Okano, and K. Satoh, "Planar reflection grating lens for compact spectroscopic imaging system," *Appl. Opt.*, vol. 42, no. 2, pp. 175–180, 2003.

[75] S. Grabarnik, R. Wolffenbuttel, A. Emadi, M. Loktev, E. Sokolova, and G. Vdovin, "Planar double-grating microspectrometer," *Opt. Express*, vol. 15, no. 6, pp. 3581–3588, 2007.

[76] S. Grabarnik, A. Emadi, H. Wu, G. De Graaf, G. Vdovin, and R. F. Wolffenbuttel, "Ic-compatible microspectrometer using a planar imaging diffraction grating," in *Micro-Optics 2008* (H. Thienpont, P. Van Daele, J. Mohr, and M. R. Taghizadeh, eds.), vol. 6992, (Strasbourg, France), pp. 699215–10, SPIE, 2008.

[77] S. Grabarnik, A. Emadi, H. Wu, G. de Graaf, and R. F. Wolffenbuttel, "High-resolution microspectrometer with an aberration-correcting planar grating," *Appl. Opt.*, vol. 47, no. 34, pp. 6442–6447, 2008.

[78] M. Tormen, R. Lockhart, P. Niedermann, T. Overstoltz, A. Hoogerwerf, J.-M. Mayor, J. Pierer, C. Bosshard, R. Ischer, G. Voirin, and R. P. Stanley, "MEMS tunable grating micro-spectrometer," in *International Conference on Space Optics*, (Toulouse, France), 2008.

[79] M. M. Chitteboyina and D. P. Butler, "Tunable infrared microspectrometer based on bragg grating," *Quantum Electronics, IEEE Journal of*, vol. 44, no. 2, pp. 182–184, 2008.

[80] Tydex. `http://www.tydexoptics.com`, Lasted checked: July 2011.

[81] P. R. Norton, "Infrared detectors in the next millennium," in *SPIE*, vol. 3698 of *Proceedings of SPIE - The International Society for Optical Engineering*, (Bellingham, WA, USA), pp. 652–665, Society of Photo-Optical Instrumentation Engineers, 1999.

[82] P. G. Datskos and N. V. Lavrik, "Uncooled infrared mems detectors," *Smart Sensors and MEMS*, vol. 181, pp. 381–419, 2004.

[83] A. Rogalski, "Infrared detectors: status and trends," *Progress in Quantum Electronics*, vol. 27, no. 2-3, pp. 59–210, 2003.

[84] S. Haywood, K. Lai, and M. Missous, "QWIP detectors for the MWIR," in *Mid-infrared Semiconductor Optoelectronics* (A. Krier, ed.), Optical Sciences, London: Springer, 1st ed., 2006.

[85] J. Caniou, *Passive infrared detection: Theory and Application*. Dordrecht: Kluwer Academic Publishers, 1999.

[86] F. Träger, *Handbook of Lasers and Optics*. New York: Springer Science+Business Media, 2007.

[87] D. L. Smith and C. Mailhiot, "Proposal for strained type ii superlattice infrared detectors," *Journal of Applied Physics*, vol. 62, no. 6, pp. 2545–2548, 1987.

[88] B. F. Levine, K. K. Choi, C. G. Bethea, J. Walker, and R. J. Malik, "New 10 μm infrared detector using intersubband absorption in resonant tunneling GaAlAs superlattices," *Applied Physics Letters*, vol. 50, no. 16, pp. 1092–1094, 1987.

[89] S. Maimon and G. W. Wicks, "nbn detector, an infrared detector with reduced dark current and higher operating temperature," *Applied Physics Letters*, vol. 89, no. 15, pp. 151109–3, 2006.

[90] D. Z. Y. Ting, S. V. Bandara, J. Mumolo, S. A. Keo, J. Nguyen, H. C. Liu, C. Y. Song, Y.-C. Chang, S. B. Rafol, C. J. Hill, S. D. Gunapala, A. Soibel, J. K. Liu, and E. Blazejewski, "Dots, QWISPs, and BIRDs," *Infrared Physics & Technology*, vol. 52, no. 6, pp. 294–298, 2009.

[91] S.-H. Lin, Y.-H. Wang, C.-W. Chang, J.-H. Lu, C. C. Chen, and C.-H. Kuan, "Development of superlattice infrared photodetectors," in *Cutting Edge Nanotechnology* (D. Vasileska, ed.), InTech, 2010.

[92] H. C. Liu, "Quantum well infrared photodetector physics," in *Intersubband Transitions in Quantum Wells: Physics and Device Applications I* (H. C. Liu and F. Capasso, eds.), vol. 62 of *Semiconductors and Semimetals*, San Diego: Academic Press, 2000.

[93] A. Rogalski, "Quantum well photoconductors in infrared detector technology," *Journal of Applied Physics*, vol. 93, no. 8, pp. 4355–4391, 2003.

[94] M. Helm, "The basic physics of intersubband transitions," in *Intersubband Transitions in Quantum Wells: Physics and Device Applications I* (H. C. Liu and F. Capasso, eds.), vol. 62 of *Semiconductors and Semimetals*, San Diego: Academic Press, 2000.

[95] Y.-C. Chang and R. B. James, "Saturation of intersubband transitions in p-type semiconductor quantum wells," *Physical Review B*, vol. 39, no. 17, p. 12672, 1989.

[96] B. F. Levine, S. D. Gunapala, J. M. Kuo, S. S. Pei, and S. Hui, "Normal incidence hole intersubband absorption long wavelength GaAs/$Al_xGa_{1-x}As$ quantum well infrared photodetectors," *Applied Physics Letters*, vol. 59, no. 15, pp. 1864–1866, 1991.

[97] J. Katz, Y. Zhang, and W. I. Wang, "Normal incidence infra-red absorption from intersubband transitions in p-type GaInAs/AlInAs quantum wells," *Electronics Letters*, vol. 28, no. 10, pp. 932–934, 1992.

[98] C.-L. Yang, D.-S. Pan, and R. Somoano, "Advantages of an indirect semiconductor quantum well system for infrared detection," *Journal of Applied Physics*, vol. 65, no. 8, pp. 3253–3258, 1989.

[99] E. R. Brown and S. J. Eglash, "Calculation of the intersubband absorption strength in ellipsoidal-valley quantum wells," *Physical Review B*, vol. 41, no. 11, p. 7559, 1990.

[100] W. Xu, Y. Fu, and M. Willander, "Oscillator strength and absorption coefficient and their optimization for quantum wells to detect normally incident radiation," *Physical Review B*, vol. 48, no. 15, p. 11477, 1993.

[101] W. Xu, Y. Fu, M. Willander, and S. C. Shen, "Theory of normal-incidence absorption for the intersubband transition in n-type indirect-gap semiconductor quantum wells," *Physical Review B*, vol. 49, no. 19, p. 13760, 1994.

[102] R. Q. Yang, J. M. Xu, and M. Sweeny, "Selection rules of intersubband transitions in conduction-band quantum wells," *Physical Review B*, vol. 50, no. 11, p. 7474, 1994.

[103] B. Sherliker and et al., "Room temperature operation of AlGaN/GaN quantum well infrared photodetectors at a 3-4 μm wavelength range," *Semiconductor Science and Technology*, vol. 22, no. 11, p. 1240, 2007.

[104] A. D. Stiff-Roberts and et al., "Room-temperature, mid-infrared photodetection in colloidal quantum dot/conjugated polymer hybrid nanocomposites: a new approach to quantum dot infrared photodetectors," *Journal of Physics D: Applied Physics*, vol. 42, no. 23, p. 234004, 2009.

[105] A. Rogalski, "Insight on quantum dot infrared photodetectors," *Journal of Physics: Conference Series*, vol. 146, no. 1, p. 012030, 2009.

[106] H. Lim, S. Tsao, W. Zhang, and M. Razeghi, "High-performance InAs quantum-dot infrared photodetectors grown on InP substrate operating at room temperature," *Applied Physics Letters*, vol. 90, no. 13, pp. 131112–3, 2007.

[107] J. Phillips, "Evaluation of the fundamental properties of quantum dot infrared detectors," *Journal of Applied Physics*, vol. 91, no. 7, pp. 4590–4594, 2002.

[108] C. Calaza, N. Viarani, G. Pedretti, M. Gottardi, A. Simoni, V. Zanini, and M. Zen, "An uncooled infrared focal plane array for low-cost applications fabricated with standard CMOS technology," *Sensors and Actuators A: Physical*, vol. 132, no. 1, pp. 129–138, 2006.

[109] X. Dehui and et al., "Design, fabrication and characterization of a front-etched micromachined thermopile for IR detection," *Journal of Micromechanics and Microengineering*, vol. 20, no. 11, p. 115004, 2010.

[110] A. Emadi, H. Wu, S. Grabarnik, G. De Graaf, and R. F. Wolffenbuttel, "Infrared thermopile detector array for the integrated microspectrometer," in *Sensors, 2007 IEEE*, pp. 435–438, 2007.

[111] Y. Li, H. Zhou, T. Li, Y. Wang, Y. Liu, and Y. Wang, "CMOS-compatible 8x2 thermopile array," *Sensors and Actuators A: Physical*, vol. 161, no. 1-2, pp. 120–126, 2010.

[112] A. Roncaglia, F. Mancarella, and G. C. Cardinali, "CMOS-compatible fabrication of thermopiles with high sensitivity in the 3-5 μm atmospheric window," *Sensors and Actuators B: Chemical*, vol. 125, no. 1, pp. 214–223, 2007.

[113] M. Ahn, Y.-H. Han, and S. Moon, "A novel infrared absorbing structure for uncooled infrared detector," *Current Applied Physics*, vol. 7, no. 6, pp. 617–621, 2007.

[114] C. Chen, X. Yi, X. Zhao, and B. Xiong, "Characterizations of VO_2-based uncooled microbolometer linear array," *Sensors and Actuators A: Physical*, vol. 90, no. 3, pp. 212–214, 2001.

[115] H. Jerominek, M. Renaud, N. R. Swart, F. Picard, T. D. Pope, M. Levesque, M. Lehoux, G. Bilodeau, M. Pelletier, D. Audet, and P. Lambert, "Micromachined VO_2-based uncooled IR bolometric detector arrays with integrated CMOS readout electronics," in *Micromachined Devices and Components II* (K. H. Chau and R. M. Roop, eds.), vol. 2882, (Austin, TX, USA), pp. 111–121, SPIE, 1996.

[116] A. Jahanzeb, C. M. Travers, Z. Celik-Butler, D. P. Butler, and S. G. Tan, "A semiconductor ybacuo microbolometer for room temperature ir imaging," *Electron Devices, IEEE Transactions on*, vol. 44, no. 10, pp. 1795–1801, 1997.

[117] M. F. Almasri, Z. Celik-Butler, D. P. Butler, A. Yaradanakul, and A. Yildiz, "Semiconducting ybacuo microbolometers for uncooled broadband ir sensing," in *Infrared Technology and Applications XXVII* (B. F. Andresen, G. F. Fulop, and M. Strojnik, eds.), vol. 4369, (Orlando, FL, USA), pp. 264–273, SPIE, 2001.

[118] H. Wada, T. Sone, H. Hata, Y. Nakaki, O. Kaneda, Y. Ohta, M. Ueno, and M. Kimata, "Ybacuo uncooled microbolometer irfpa," in *Infrared Technology and Applications XXVII* (B. F. Andresen, G. F. Fulop, and M. Strojnik, eds.), vol. 4369, (Orlando, FL, USA), pp. 297–304, SPIE, 2001.

[119] S. Eminoglu, M. Y. Tanrikulu, and T. Akin, "A low-cost 128 x 128 uncooled infrared detector array in CMOS process," *Microelectromechanical Systems, Journal of*, vol. 17, no. 1, pp. 20–30, 2008.

[120] M. Kimata, M. Ueno, M. Takeda, and T. Seto, "Soi diode uncooled infrared focal plane arrays," in *Quantum Sensing and Nanophotonic Devices III* (M. Razeghi and G. J. Brown, eds.), vol. 6127, (San Jose, CA, USA), pp. 61270X–11, SPIE, 2006.

[121] P. Neuzil, L. Yong, F. Han-Hua, and Z. Wenjiang, "Micromachined bolometer with single-crystal silicon diode as temperature sensor," *Electron Device Letters, IEEE*, vol. 26, no. 5, pp. 320–322, 2005.

[122] D. L. Polla, C.-p. Ye, and T. Tamagawa, "Surface-micromachined PbTiO3 pyroelectric detectors," *Applied Physics Letters*, vol. 59, no. 27, pp. 3539–3541, 1991.

[123] Y. Tang and H. Luo, "High-performance pyroelectric single crystals for uncooled infrared detection applications," *Infrared Physics & Technology*, vol. 52, no. 5, pp. 180–182, 2009.

[124] B. Willing, M. Kohli, P. Muralt, N. Setter, and O. Oehler, "Gas spectrometry based on pyroelectric thin-film arrays integrated on silicon," *Sensors and Actuators A: Physical*, vol. 66, no. 1-3, pp. 109–113, 1998.

[125] B. Jiao, C. Li, D. Chen, T. Ye, S. Shi, Y. Ou, L. Dong, Q. Zhang, Z. Guo, F. Dong, and Z. Miao, "A novel opto-mechanical uncooled infrared detector," *Infrared Physics & Technology*, vol. 51, no. 1, pp. 66–72, 2007.

[126] F. Dong, Q. Zhang, D. Chen, Z. Miao, Z. Xiong, Z. Guo, C. Li, B. Jiao, and X. Wu, "Uncooled infrared imaging device based on optimized optomechanical micro-cantilever array," *Ultramicroscopy*, vol. 108, no. 6, pp. 579–588, 2008.

[127] X. Dehui, J. Errong, X. Bin, and W. Yuelin, "Wafer-level vacuum packaging of micromachined thermoelectric ir sensors," *Advanced Packaging, IEEE Transactions on*, vol. 33, no. 4, pp. 904–911, 2010.

[128] E. Masayoshi, "Wafer level packaging of mems," *Journal of Micromechanics and Microengineering*, vol. 18, no. 7, p. 073001, 2008.

[129] F. Santagata, *Mechanical robustness and hermeticity monitoring for MEMS thin-film encapsulation*. PhD thesis, TU Delft, 2011.

[130] S. Eminoglu, D. S. Tezcan, M. Y. Tanrikulu, and T. Akin, "Low-cost uncooled infrared detectors in CMOS process," *Sensors and Actuators A: Physical*, vol. 109, no. 1-2, pp. 102–113, 2003.

[131] H. Wu, *MEMS-based linear thermopile detector arrays for IR microspectrometers*. PhD thesis, Technical University Delft, 2011.

[132] K. C. Liddiard, "Application of interferometric enhancement to self-absorbing thin film thermal IR detectors," *Infrared Physics*, vol. 34, no. 4, pp. 379–387, 1993.

[133] Thin Film Center, "Essential Macleod 8.14.159(ie) software." `http://www.thinfilmcenter.com/`.

[134] F. Incropera and D. DeWitt, *Introduction to Heat Transfer*. John Wiley & Sons, Inc., 3rd ed., 1996.

[135] D. R. Pitts and L. Sissom, *Theory and problems of Heat Transfer*. Schaums Outline Series, McGraw-Hill Book Company, 1977.

[136] J. A. Potkay, G. R. Lambertus, R. D. Sacks, and K. D. Wise, "A low-power pressure- and temperature-programmable micro gas chromatography column," *Microelectromechanical Systems, Journal of*, vol. 16, no. 5, pp. 1071–1079, 2007.

[137] Spectral Calc, "Calculation of blackbody radiance V2," 2011.

[138] M. A. Heald, "Where is the "wien peak"?," *American Journal of Physics*, vol. 71, no. 12, pp. 1322–1323, 2003.

[139] J. M. Overduin, "Eyesight and the solar wien peak," *American Journal of Physics*, vol. 71, no. 3, pp. 216–219, 2003.

[140] M. Eppley and A. R. Karoli, "Use of wave number in radiation formulas," *J. Opt. Soc. Am.*, vol. 43, no. 11, pp. 957–959, 1953.

[141] COMSOL, "Theory of heat transfer," in *COMSOL Multiphysics: Heat Transfer Module*, 3.5a ed., 2008.

[142] T. M. Adams and A. Layton, Richard, *Introductory MEMS: Fabrication and applications*. Springer, 2010.

[143] T. Hsu, *MEMS and Microsystems: Design, Manufacture, and Nanoscale engineering*. New Jersey: John Wiley & Sons, Inc., 2nd ed., 2008.

[144] J. Gere and S. Timoshenko, *Mechanics of Materials*. Cheltenham: Stanley Thornes Ltd, 4th ed., 1999.

[145] S. Timoshenko and S. Woinowsky-Krieger, "Bending of plates supported by rows of equidistant columns (flat slabs)," in *Theory of plates and shells*, McGraw-Hill, 2nd ed., 1959.

[146] J. F. Creemer, D. Briand, H. W. Zandbergen, W. van der Vlist, C. R. de Boer, N. F. de Rooij, and P. M. Sarro, "Microhotplates with tin heaters," *Sensors and Actuators A: Physical*, vol. 148, no. 2, pp. 416–421, 2008.

[147] MEMSnet, "Memsnet." `http://www.memsnet.org/`, Lasted checked: july 2011.

[148] G. Harris, *Properties of Silicon Carbide*. Institution of Engineering and Technology, 1995.

[149] RefractiveIndex.info, "Refractive Index database." `http://www.refractiveindex.info`, Lasted checked: July 2011.

[150] D. D. L. Wijngaards, *Lateral on-chip integrated Peltier elements*. Phd. thesis, Technical University of Delft, 2003.

[151] K. R. Williams, K. Gupta, and M. Wasilik, "Etch rates for micromachining processing-part ii," *Microelectromechanical Systems, Journal of*, vol. 12, no. 6, pp. 761–778, 2003.

[152] The Engineering Toolbox, "The Engineering Toolbox." `http://www.engineeringtoolbox.com`, Lasted checked: July 2011.

[153] A. Witvrouw, B. D. Bois, P. D. Moor, A. Verbist, C. A. V. Hoof, H. Bender, and C. Baert, *Comparison between wet HF etching and vapor HF etching for sacrificial oxide removal*, vol. 4174. SPIE, 2000.

Appendices

Appendix A

Material Properties

NOTE: Material properties are very much dependent on the conditions they were deposited at. Therefore, actual values may differ significantly from those found in literature as presented in this appendix. (* Self measured value).

Material	**Young's Modulus [GPa]**	**Poisson's Ratio**	**Density [kg m^{-3}]**	**Thermal Exp. Coeff. [$\cdot 10^{-6}$ K^{-1}]**	**Reference**
SiO_2 (TEOS)	46-68		2200	1.83	[18, 147]
SiN (PECVD)	134-142		3100	1.80	[18]
SiN (LPCVD)	230-265	0.22-0.27	2400	2.2-3.34	[18, 147]
SiC	400-450	0.183-0.192	3200		[147, 148]
PolySi	140-171		2328		[18]
Mo, bulk	343		10300		[147]
Ti, bulk	115		4510	8.5	[147]
TiN, film	380-450	0.25	5430	9.35	[147]
Al, bulk	70		2700	23.1	[147]

Table A.1: Mechanical properties of materials

Material	**Refractive Index**	**Extinction Coefficient**	**Reference**
SiO_2 (TEOS)	1.39	0	[133]
SiN (PECVD)	2.05	$8{\cdot}10^{-5}$	[133]
SiN (LPCVD)	2.15*	0*	
SiC	2.56		[149]
PolySi	3.93	0	[149]
Mo	2.32	22.98	[149]
Ti	4.66	7.27	[133]
TiN	5.9*	10.97*	
Al	6.1	30.4	[133]

Table A.2: Optical properties of materials at a wavelength of 4μm.

Material	**Thermal conductivity [W m^{-1} K^{-1}]**	**Specific heat [J kg^{-1} K^{-1}]**	**Reference**
SiO_2 (TEOS)	1.38	745	[18]
SiN (PECVD)	3.2	700	[18]
SiN (LPCVD)	15.88	691	[147]
SiC	3.6	711	[148]
PolySi	30-35		[18]
PolySi N ($7.5{\cdot}10^{15}$ cm^{-2})	29	753	[18]
PolySi P ($5{\cdot}10^{15}$ cm^{-2})	34	753	[18]
Mo, bulk	138	233.7	[147]
Ti, bulk	21.9	522.5	[147]
TiN	19.2		[]
Al, bulk	237	898.7	[147]

Table A.3: Thermal properties of materials

Material	**Sheet Resistance [$\Omega/\square$]**	**Seebeck Coefficient [μV K^{-1}]**	**Reference**
PolySi N ($7.5{\cdot}10^{15}$ cm^{-2})	56*	-129	[150]
PolySi P ($5{\cdot}10^{15}$ cm^{-2})	115*	174	[150]
Al		-1.7	[18]

Table A.4: Electrical properties of materials

Material	**Process Temp. [°C]**	**Melting Temp. [°C]**	**Etch rate in Vapour HF [nm min^{-1}]**	**Reference**
SiO_2 (TEOS)	650-750		See section 9.2.1*	[13]
SiN (PECVD)	350		See section 9.2.3*	[]
SiN (LPCVD)	850		See section 9.2.3*	[]
SiC				[]
PolySi	580		0	[151]
Mo		2620		[152]
Ti	350	1670	R	[151, 152]
TiN	350	2930	$0.06{\cdot}10^{-3}$	[153]
Al	350	660	$0.19{\cdot}10^{-3}$	[152, 153]

Table A.5: Properties which influence the process. Etch rate notations: R=Visibly roughened or attacked.

Appendix B

Process Flowchart

This chapter is removed. Please contact G. de Graaf (ger.degraaf@tudelft.nl) if one would like to obtain this chapter.

Appendix C

Read-Out circuit

This chapter is removed. Please contact G. de Graaf (ger.degraaf@tudelft.nl) if one would like to obtain this chapter.